

Evaluation of Metal Building System Seismic Response Modification Coefficients

Project report written by:
NBM Technologies, Inc.

Cristopher D. Moen
Shahab Torabian
Benjamin W. Schafer

For:
Metal Building Manufacturers Association

April 2019

Table of Contents

Executive Summary	4
1. Introduction	
2. Seismic Evaluation of Metal Buildings with High Fidelity Simulation	8
2.1. Seismic design practice explored with high fidelity simulation	8
2.2. Probabilistic seismic analysis	8
2.3. Cyclic simulation to collapse of metal buildings	8
2.4. A seismic evaluation methodology for metal buildings	9
3. Metal Building Seismic Design Studies	11
3.1. Strategy for metal building seismic archetype selection	11
3.2. Seismic design practice for metal buildings	11
3.3 Influence of the seismic response modification factor R on metal building design	12
3.4 Influence of geographical location on metal building design	14
4. Metal Building Seismic Archetype Selection and Design	20
4.1. Archetype building dimensions and details	20
4.2. Archetype building design assumptions	21
4.3. Archetype building seismic parameters (R, Cd, o)	22
4.4. Archetype building performance evaluation strategy	23
5. High Fidelity Metal Building Modeling Protocol	24
5.1. The motivation for high fidelity simulation	24
5.2. Programming, platform, and choice of finite element software	24
5.3. Main frame modeling	24
5.4. Modeling of purlins, girts, and eave struts	26
5.5. Rod brace and flange brace modeling	27
5.6. Roof and wall sheeting modeling	27
5.7. Steel material modeling	27
5.8. Hard wall modeling	28
5.9 Roof mass modeling	31
5.10. Mezzanine modeling	31
5.11. Primary frame baseplate modeling	32
5.12. Modeling protocol summary	35
6. Validation of the High Fidelity Metal Building Frame Modeling Protocol	36
6.1. High fidelity simulation of selected UCSD cyclic lateral-torsional buckling tests	36

6.2. High fidelity simulation of selected UCSD shake table tests	41
6.3. High fidelity simulation accuracy: maximum drift as a function of earthquake Intensity	52
7. Observing and modeling metal building seismic limit states	54
7.1. Metal building seismic limit states captured by the high fidelity modeling protocol	54
7.2. Metal building seismic limit states excluded in the high fidelity modeling protocol	54
7.3. Plastic strain demands from high fidelity seismic simulation	55
7.4. A drift-based fracture limit for defining metal building system collapse	58
8. A Computationally Efficient Nonlinear Metal Building Seismic Time History Modeling Protocol	60
8.1. Using high fidelity simulation to inform computational efficient seismic modeling	60
8.2. Nonlinear SDOF metal building response to seismic ground motions	60
8.3. Metal building SDOF seismic simulation parameter: stiffness, K_t	61
8.4. Metal building SDOF seismic simulation parameter: period, T	63
8.5. Metal building SDOF seismic simulation parameter: mass, m	63
8.6. Metal building SDOF seismic simulation parameter: equivalent initial stiffness, keq	64
8.7. Metal building SDOF seismic simulation parameter: damping ratio, ξ	65
8.8. Validation of metal building nonlinear SDOF seismic modeling protocol	65
8.9. Employing high fidelity and nonlinear dynamic SDOF metal building models in archetype seismic studies	67
9. Probabilistic Seismic Evaluation of UCSD Metal Building Shake Table Specimens	68
9.1. Using FEMA P695 to conduct seismic hazard characterization of metal buildings	68
9.2. Nonlinear static pushover analysis to calculate UCSD shake table Specimen B1 and B2 system overstrength	70
9.3. Incremental dynamic analysis analysis and fragility curves for UCSD shake table Specimen B1 and B2	71
9.4. Building system collapse definition and fragility curves for UCSD shake table Specimen B1 and B2	73
9.5. Calculation of collapse margin ratio (ACMR) for UCSD shake table specimens B1 and B2	74
9.6. Seismic evaluation summary for UCSD metal building shake table specimens B1 and B2	75
10. Probabilistic Seismic Evaluation of Selected Metal Building Archetypes	76
10.1. Defining the performance group of metal building index archetypes	76
10.2. Calculation of performance group natural periods with high fidelity modal analysis	77
10.3. Nonlinear static pushover analysis to calculate performance group system overstrength	78

10.4. Quasi-static high fidelity cyclic archetype simulation and SDOF spring model calibration	81
10.5. Incremental dynamic analysis analysis and fragility curves for metal building index archetypes	84
10.6. Seismic evaluation summary for archetype performance groups	89
11. Conclusions and Possible Next Steps	91
Acknowledgments	92
References	93

Executive Summary

A seismic evaluation was conducted of common metal building configurations within the probabilistic framework defined in FEMA P695 “Quantification of Building Seismic Performance Parameters” with the goal of evaluating the applicability of current seismic design procedures in the ASCE 7-10 “Minimum Design Loads for Buildings and Other Structures”. The evaluation began with the definition of a performance group of index archetypes which was guided by industry steering group-led design studies that explored the influence of seismic load combinations and geographical location on the primary frame design. It was observed that taller, shorter span buildings in the western U.S. were most sensitive to seismic demands. This led to the definition of a performance group covering a range of natural periods and seismic weights designed to ASCE Seismic Category D and with the seismic response modification factor of $R=3.5$.

The seismic parameters calculated for the performance group, designed by industry with ASCE Equivalent Lateral Force procedures, were the system overstrength, ductility, and probability of system collapse when exposed to the Maximum Considered Earthquake (MCE) which has a 2% probability of exceedance in 50 years. The system overstrength and ductility for each index archetype were calculated with simulated experiments using thin shell high fidelity simulation, where all metal building components were modeled including the built-up primary frames, the girts and purlins, the exterior metal facade and screw down roof, the rod bracing, and the primary frame flange braces that are important for controlling lateral-torsional buckling. The high fidelity simulation protocol was extensively validated with research between 2006 and 2013 that included monotonic and cyclic primary frame subassembly tests and shake table tests at the University of California, San Diego.

The simulated pushover experiments revealed significant system overstrength in the index archetypes and a post-peak ductile response that was sensitive to the controlling limit state. When primary frame lateral-torsional buckling was controlled by the intermediate flange braces, post-peak deformation was available out to large drifts. Panel zone buckling at the knee of the column/rafter resulted in steady post-peak strength degradation. The heavy wall buildings had a higher pushover strength than the light wall buildings because the seismic design load combinations were more influential on the heavy wall primary frame design.

The same high fidelity models were used to characterize the quasi-static cyclic response for each index archetype using an accepted American Institute for Steel Construction (AISC) industry loading protocol. The cyclic response, including strength and stiffness degradation from local and global buckling and column-rafter knee panel zone tension field yielding, was fit to a nonlinear Single-Degree-of Freedom (SDOF) material model used for incremental dynamic analysis (IDA). The IDA performances from 44 far-field ground motions required by FEMA P695 led to a cumulative distribution function of spectral intensity of the far-field record set which could be used to calculate the median collapse probability for each index archetype.

Uncontrolled collapse was never observed for these light buildings in the simulations or the shake table experiments, however fracture was, in the knee-rafter panel zone from shear buckling and in the rafter taper joints after lateral-torsional buckling. Both drift and fracture studies were conducted to settle on a drift-based collapse limit of 4.5% for the performance group.

The collapse margin ratio, defined as the spectral acceleration at median collapse probability to the spectral acceleration from the Maximum Considered Earthquake (MCE) was on average across the metal building performance group higher than the acceptable collapse margin ratio corresponding to a 10% collapse probability, with no outliers greater than 20%. This confirms the viability of the existing ASCE 7 equivalent lateral force seismic design procedures for metal buildings in the performance group considered.

With the seismic evaluation process now established and validated, the metal building industry can now investigate other performance groups with potentially large commercial impact - for example, heavier roof buildings that are outside the limits of current ASCE 7 procedures. A modular metal building seismic performance group also becomes available for study with the verified high fidelity modeling protocol used to perform simulated pushover experiments and to quantify cyclic performance.

1. Introduction

The metal building industry is motivated to advance their seismic design approaches because they see it as an opportunity to leverage benefits of 3D system performance, beyond their typical 2D planar frame analyses. This report summarizes a recently completed multi-year study that unearths and highlights these benefits.

It is helpful to first review the existing Metal Building Manufacturers Association (MBMA) seismic research investigations that serve as the foundation for the seismic studies summarized herein. The funded research on seismic response by MBMA started in 2004 at University of California - San Diego (UCSD) with main frame quasi-static cyclic tests (Hong and Uang 2006). The frames behaved elastically up to drifts of 2.5%, and then experienced lateral-torsional buckling which resulted in significant cyclic strength degradation. The flange brace details in this study were considered 'soft', with long slotted holes at the end bolts.

The results from the Hong and Uang (2006) study, especially the observation that there was a rapid drop in lateral stiffness from main frame global lateral-torsional buckling, led to the proposal of a drift limit seismic design approach for metal buildings (Hong and Uang 2007). The premise of this approach was to avoid the lateral stiffness drop by imposing a drift limit in the elastic response range of the main frame, defining required system overstrength by dividing the elastic seismic demand by $R=3.5$ (taken from AISC ordinary moment frame seismic design), and capping drift capacity to that of the weakest main frame component.

The applicability of the UCSD drift limit criteria was evaluated with outdoor unidirectional shake table tests of metal building segments (two primary frames connected with girts, purlins, and panels) at UCSD. The test matrix covered standard, heavy wall, and a mezzanine configurations that had been explored in UCSD analytical studies (Smith 2013). The buildings were exposed to several seismic ground motion records, focusing on the Imperial Valley record at varying scaled magnitudes. Lateral-torsional buckling of the main frames was a key contributor to strength and stiffness degradation in the shake table tests, with fracture developing in the main frame inner flange (flange not connected to purlins) where the web taper pinches. The fracture developed at high seismic demands up to IV300, i.e., the Imperial Valley ground motion record scaled to 300%. Total system collapse was never observed in the tests and the primary frames accommodated up to 4% drift with some fracture observed. For example, rafter-column knee panel zone buckling and fracture developed in the hard wall building with a mezzanine at this drift magnitude. The empirical natural period prediction equations in ASCE 7-10 (ASCE 2010) were confirmed to underpredict the actual natural period of the metal building frames and new equations were proposed and validated (Smith 2013).

Uncertainty around this drift limit approach and confusion about the seismic response modification factor, R , led MBMA to more cyclic testing at UCSD. Quasi-static cyclic frame subassembly tests that exercised typical column-knee-rafter configurations documented low cycle fatigue response (Smith et al. 2013). The tests were designed to include typical main frame bracing conditions - purlins on the outer flange and discrete brace points on the inner flanges where the brace forces were measured throughout the tests. Failure modes included lateral-torsional buckling between flange brace points and flange local buckling at tapered locations and it was confirmed that the main frame tapered members could undergo several LTB cycles without fracture. The test results were compared to predictions from AISC Design Guide 25 - Frame Design using Web-Tapered Members (Kaelher et al. 2011), confirming that LTB capacity of the main frames could be determined if the calculation of the critical elastic buckling moment considers the bracing conditions.

All of this UCSD experimental data was well documented through significant MBMA investment with the idea that it would support a future high fidelity system simulation research phase. This simulation phase was completed over the past three years (2015-2018) by NBM Technologies, Inc. (NBM) within the relatively new FEMA P695 framework (ATC 2009) that defines a collapse margin ratio as a metric of seismic performance. A detailed description of the simulation studies follows that are used to perform seismic performance characterization of standard and hard wall metal building archetypes.

2. Seismic Evaluation of Metal Buildings with High Fidelity Simulation

2.1. Seismic design practice explored with high fidelity simulation

A primary goal of this study is to document how metal buildings designed with current seismic design practice perform in actual earthquakes. For lower magnitude earthquakes, what is the elastic drift response? For higher magnitude earthquakes, how do the design assumptions (e.g., the choice of R , the seismic response modification coefficient) affect the probability of structural collapse? These questions have historically been challenging to answer without instrumenting buildings and waiting for earthquakes to happen. Advances in high performance computing and probabilistic seismic analysis make these answers as accessible as they have ever been.

2.2. Probabilistic seismic analysis

The probabilistic seismic analysis framework in FEMA P695 (ATC 2009) is followed in this study to quantify the Adjusted Collapse Margin Ratio (ACMR) for a performance group of metal building index archetypes, where the ACMR is the ratio of the seismic demands that will result in a building collapse under at least 50% of the standard earthquake records to the seismic demands associated with the Maximum Considered Earthquake (MCE) amplified by the Spectrum Shape Factor, SSF , to account for the reduced acceleration demands relative to uniform hazard spectra when considering actual MCE-level ground motion spectra (ATC 2009, Appendix B).

Using 44 earthquake records with different frequency contents, performing nonlinear response analyses, considering uncertainties (e.g. quality of modeling, test data limitations, collapse criteria, records, and design) enables a probabilistic approach seismic evaluation of the metal buildings that not only carefully includes characteristics of the demands but also the system building response.

2.3. Cyclic simulation to collapse of metal buildings

The seismic demands used to calculate the ACMR are obtained through simulation, and these simulations require building models with the capability to yield, buckle, fracture, and redistribute forces, all sources of cyclic strength and stiffness degradation that eventually lead to building collapse. Typical 2D frame models cannot directly simulate this cyclic degradation in metal buildings because the tapered primary frames are locally slender with varying cross-sections

(web and flange dimensions change along the frame) and discrete brace points at connected secondary purlin and girts that result in a complicated 3D system response.

The approach taken in this work is to use high fidelity shell finite element models, where every frame, girt, purlin, and brace is modeled including cyclic plasticity models and geometric nonlinearity. The advantage of this approach is that 3D system load paths like those in an actual metal building are considered, and primary frame buckling deformation including the complex stress states from moment, shear, and axial forces that develop in an earthquake can be evaluated. The UCSD shake table tests (Smith 2013) are used to validate the high fidelity simulation protocol.

The disadvantage of high fidelity simulation within a probabilistic seismic framework is that it requires significant computational resources, with each earthquake simulation taking potentially days to months of CPU runtime. Considering multiple ground motions at multiple amplitudes and a suite of archetypes leads to an overwhelming simulation cost. With these costs in mind, a compromise is made in this study where high fidelity quasi-static pushover and cyclic models inform computationally efficient Single Degree of Freedom (SDOF) dynamic mass-spring models. Each metal building archetype considered in this study has a surrogate SDOF model with a nonlinear hysteretic spring that approximates the cyclic response observed in the high fidelity simulations and shake table tests including strength and stiffness degradation from main frame cross-sectional, global buckling deformation and yielding, and global instabilities like P- Δ effects. The high fidelity - surrogate compromise approximates the nonlinear dynamic response while dramatically accelerating the speed with which seismic evaluation of archetype metal buildings can be completed using the FEMA P695 guidelines.

2.4. A seismic evaluation methodology for metal buildings

To summarize, the seismic evaluation methodology employed herein evaluates current metal building seismic design practice with the probabilistic collapse margin criteria recommended by FEMA P695 through the following steps: (1) design a performance group of metal building index archetype buildings; (2) construct 3D high fidelity shell finite element models of each archetype; (3) perform modal (vibration) analysis on each archetype high fidelity model to obtain the fundamental period of vibration; (4) perform pushover (nonlinear static) analysis on each archetype high fidelity model to define system overstrength and period-based ductility; (5) conduct cyclic (nonlinear static) analyses on each archetype high fidelity model to define the hysteretic response including strength and stiffness degradation that develops from primary frame local and lateral-torsional buckling; (6) construct a Single Degree of Freedom (SDOF) model that fits the hysteretic response of the high fidelity model; (7) perform incremental dynamic analysis (IDA) with the nonlinear SDOF model across a suite of earthquake ground motions (typically 44 earthquakes); (8) construct a collapse cumulative distribution function (e.g., fragility curve) for each archetype building using a drift-based collapse criterion; (8) calculate the adjusted collapse margin ratios for each building type; (9) determine acceptable collapse margin

ratios considering all uncertainties; and (10) evaluate the adjusted collapse margin ratios versus acceptable collapse margin ratios defined by FEMA P695.

The reward for running through these steps is clarity and insight about metal building seismic design including correlations between performance and metal building height, span to height, roof weight, and wall weight and seismic performance. This performance clarity can lead to better performing metal buildings, design efficiencies, and competitive advantages for the industry. The study kicks off the seismic evaluation in the next chapter with metal building design studies that will inform archetype selection.

3. Metal Building Seismic Design Studies

3.1. Strategy for metal building seismic archetype selection

Archetype selection for probabilistic performance evaluation frameworks like FEMA P695 requires some thought. The archetypes should be representative of common building types, they should consider lower and upper performance bounds typically tied to building dimensions, mass and natural frequencies, and they should be simple enough so that they can be studied and understood with simulation.

This multi-year metal building seismic characterization effort relied heavily on contributions from the MBMA steering group for the archetype selection and design and contributions from MBMA members who designed and detailed the archetype metal buildings. The procedures they followed are described in the following section, and these design activities provided insight into the influence of the seismic response modification factor, R , on metal building primary frame design.

3.2. Seismic design practice for metal buildings

Seismic design of metal buildings typically follows an equivalent lateral force approach. The building lowest mode period in the short direction, i.e., the strong direction of the primary frames, is approximated with equations provided in ASCE 7 (ASCE 2010). The natural period defines the amount of dynamic amplification that the building is susceptible to according to established response spectra. The maximum spectral acceleration for the system is obtained from the response spectrum, and then divided by the seismic response modification factor (R) that accounts for nonlinearity in the load-deformation response. Typically, R is assumed as 3.5 consistent with ordinary steel moment frames (AISC 2010). The moment envelope developing from the seismic base shear is constructed with load combinations including wind, snow, and live load, and the primary frame flanges, web, and taper are defined and optimized based on this envelope.

Metal building design starts with an approximate moment distribution that is assumed independent of primary frame and rafter dimensions and with a constant frame flexural stiffness. For example, the bending moment distribution shown in Figure 1a is determined using the spaghetti frame model in Figure 1b where columns and rafters have the same section properties. The initial design to preliminarily size the members is shown in Figure 1c.

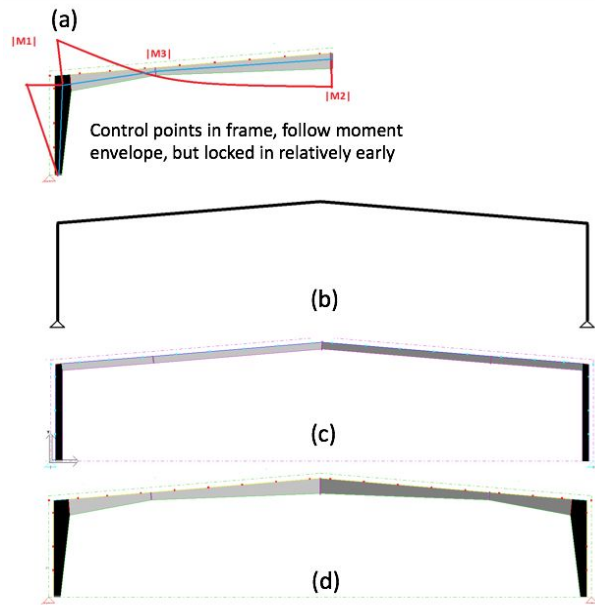


Figure 1. Metal building seismic design typically follows these steps: (a) define control points in basic moment envelope; (b) perform initial analysis using spaghetti frame; (c) perform initial design and iteration; (d) final design

The final primary frame design is obtained with automated software tools that iterate and analyze each building frame including tapered members and constant depth members with non-uniform cross-sections for the columns and rafters. Frame capacity follows the envelope of the moment demands considering all design load combinations. The frame is then checked for other limit states including shear, combined axial force and bending moment, torsion, and web crippling. The size of the frame members, the number of lateral supports, width and length of plates in the built-up frames, and all other cost-related factors are also considered and optimized in the software.

3.3. Influence of the seismic response modification factor R on metal building design

A primary factor controlling the seismic demand is the selection of the seismic response modification factor, R . It is sometimes presumed that reducing R improves the seismic performance of the building. This may not be the case however for metal building primary frame configurations with long spans because the design envelopes used to size the frames are more sensitive to gravity loads and less sensitive to lateral demands.

For example, Figure 2 shows the design moment envelope of an 80 ft clear span and 20 ft tall (at the knee) metal building. The building is initially designed for seismic demands corresponding to $R=3.5$, as shown by green positive and blue negative moment envelopes in Figure 2. When the frame is redesigned with $R=1.0$, only the red regions along the frame are governed by seismic demand. The frame design is mostly controlled by non-seismic gravity load combinations.

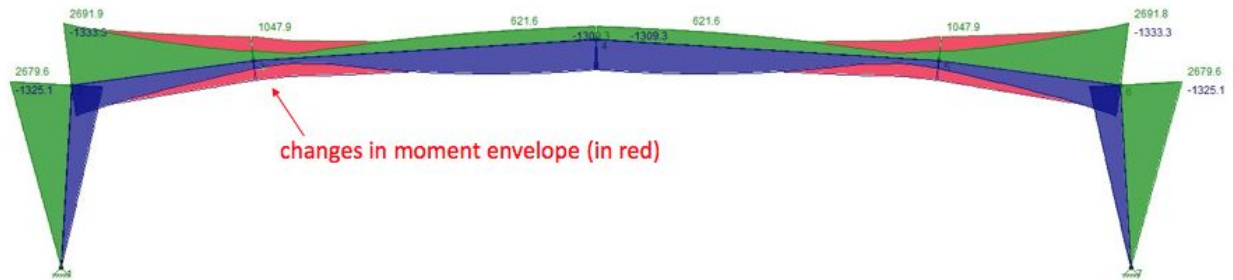


Figure 2. Flexural design envelope for a metal building frame with 80 ft clear span and 20 ft height with the seismic load calculated with $R=3.5$ shown as green (positive) and blue (negative) moment and with $R=1.0$ as the difference in red

Another metal building with a shorter span of 50 ft and a 50 ft height has the demand moment envelopes in Figure 3. Changing the seismic response modification factor R from 3.5 to 1.0 increases the rafter and column end moments at the knee by about 55% which is not proportional to the 350% increase in seismic demand when using $R=1.0$.

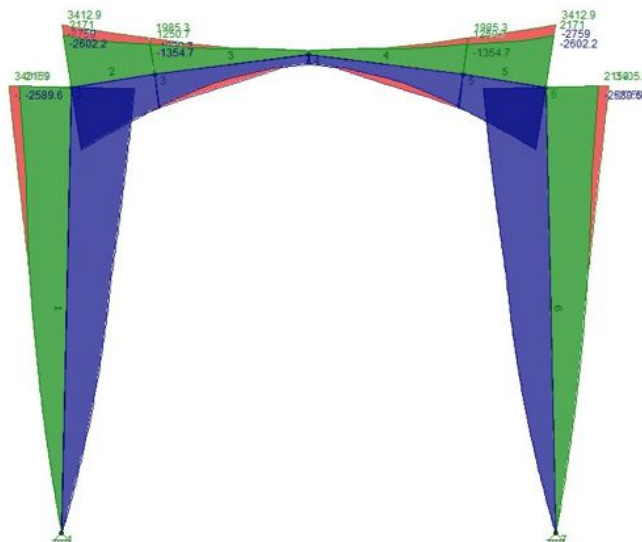


Figure 3. Flexural design envelope for a metal building frame (50 ft clear span and 50 ft height) with the seismic demand calculated using $R=3.5$ shown as green (positive) and blue (negative) moment and $R=1.0$ as the difference in red

A third example, this time a 150 ft (3 span) modular metal building shown in Figure 4 results in a 240% moment increase at the knee location when R is changed from 3.5 to 1.0. Modular metal building primary frame design is more sensitive to lateral demands because the gravity moments are decreased by a continuous rafter span supported by intermediate interior columns.

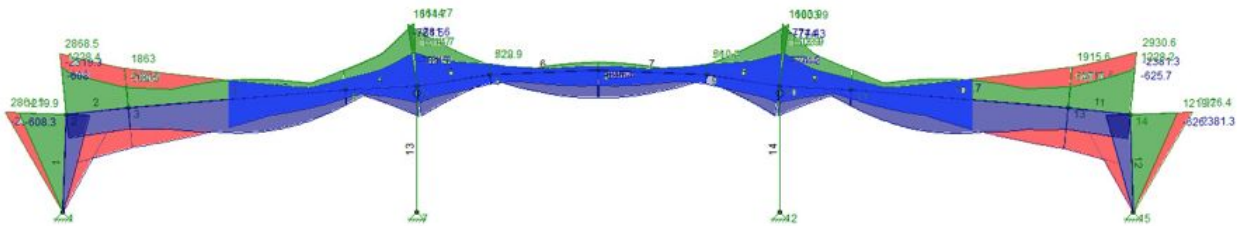


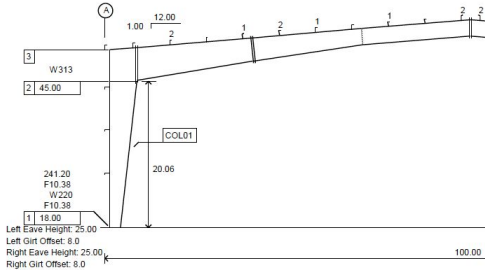
Figure 4. Flexural design envelope for a 150 ft modular 3 span metal building frame with the seismic demand calculated using $R=3.5$ shown as green (positive) and blue (negative) moment and $R=1.0$ as the difference in red

It is obvious from these results that the seismic response modification factor, R , sometimes plays an important role in the design of metal buildings and sometimes it does not, depending upon the building geometry and gravity load magnitudes. For example, snow demand loads are important in the northwest U.S. while they are not so important in the southeast U.S. The influence of location on metal building design is explored more in the next section.

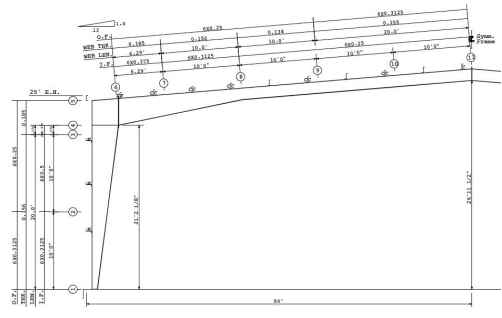
3.4. Influence of geographical location on metal building design

Designs completed by MBMA members provided further illustration of how lateral and gravity demands influence primary frame details. A series of buildings were selected: (A) 100 x 100 x 25 light wall; (B) 100 x 100 x 25 heavy wall; (C) 200 x 200 x 15 - 3 span modular light wall; (D) 200 x 200 x 15 - 3 span modular heavy wall metal buildings.

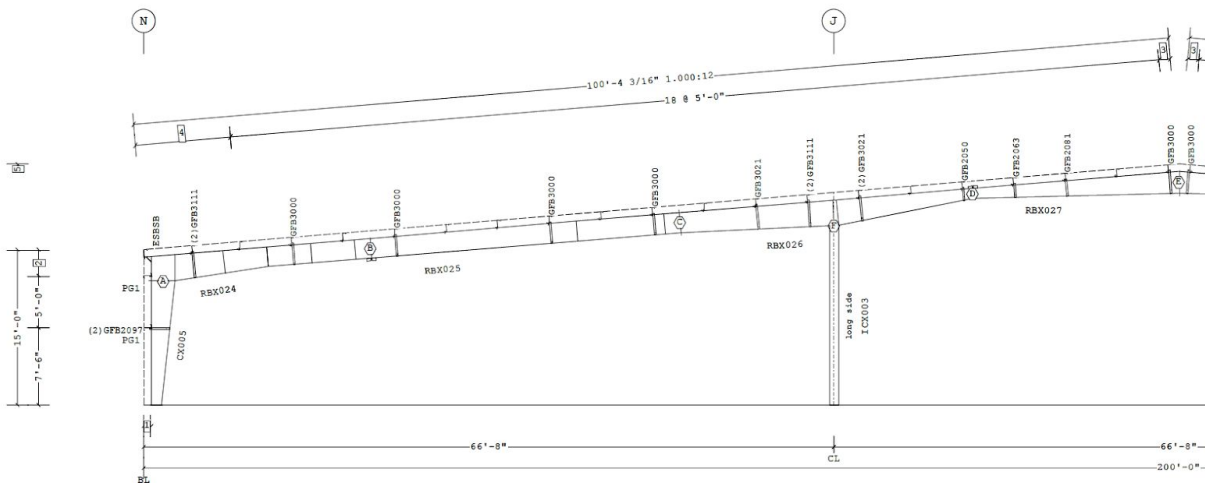
The frames are detailed in Figure 5 with dimensions summarized in Table 1.



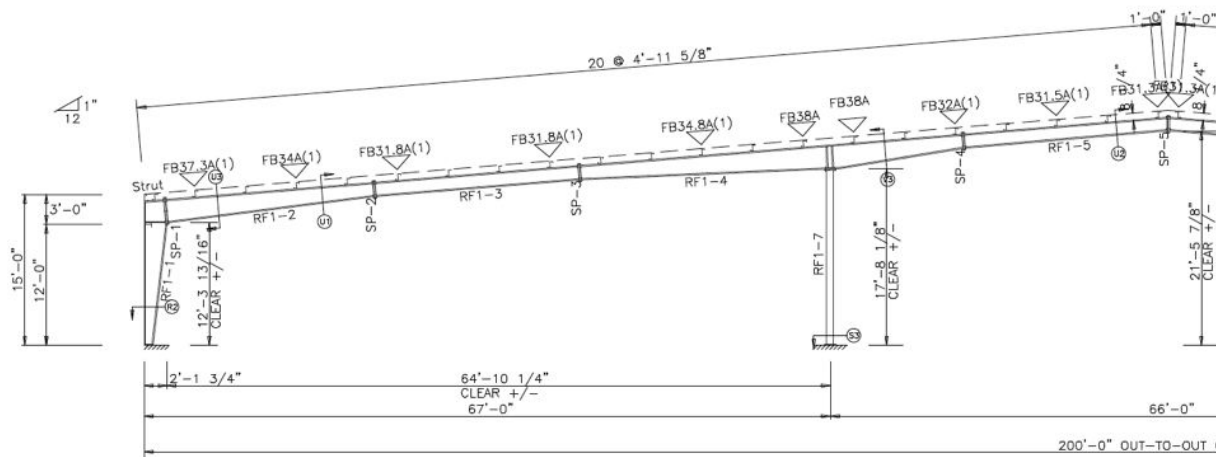
(A): 100 x 100 x 25 - Light wall



(B): 100 x 100 x 25 - Heavy wall



(C): 200 x 200 x 15 - 3 span modular - Light wall



(D): 200 x 200 x 15 - 3 span modular - Heavy wall

Figure 5. Metal buildings selected for geographical location study

Table 1. Metal buildings dimensions considered in geographical location study

Archetype	Size	Bays*	Roof Slope	Wall	Wall Weight (psf)	Drift Limit	Column Base	Design
Building A	100 x 100 x 25	4@25	(1:12)	Light	2	H/40	Pinned	NCI Group
Building B	100 x 100 x 25	4@25	(1:12)	Heavy	60	H/50	Pinned	Nucor (NBGGS)
Building C	200 x 200 x 15 3 span modular	8@25	(1:12)	Light	2	H/40	Pinned	BlueScope
Building D	200 x 200 x 15 3 span modular	8@25	(1:12)	Heavy	60	H/50	Pinned	MBS

* Number and Width

The geographical locations selected provide low, moderate, and high magnitudes of snow, wind and earthquake demands as summarized in Table 2. The demand load magnitudes, varying by location, are provided in Table 3, and seismic demand calculation details are provided in Table 4 considering a wide range of seismic base shear coefficients, with the equivalent seismic lateral load factor, C_s , ranging from 0.12 to 0.29. C_s has been determined per ASCE7 Equivalent Lateral Force Procedure.

Table 2. Range of demands considered in the metal building geographical location study

Location no.	1	2	3	4	5	6
County	Riverside	Lassen	Mississippi	Berkeley	Comanche	Anchorage
State	California	California	Arkansas	S. Carolina	Oklahoma	Alaska
Snow	Low	Moderate	Moderate	Low	Moderate	High
Wind	Moderate	Moderate	Moderate	High	Moderate	Moderate
Earthquake	High	Moderate	High	High	Low	High

Table 3. Demand magnitudes considered in the metal building geographical location study

Code: IBC 2012, ASCE7 2010						
Occupancy: Normal (Risk Category II)						
Frame Type: OMF						
Location no.	1	2	3	4	5	6
County State	Riverside California	Lassen California	Mississippi Arkansas	Berkeley S. Carolina	Comanche Oklahoma	Anchorage Alaska
Roof Live -reducible (psf)	20	20	20	20	20	20
Rain Load (psf)	0.0	0.0	0.0	0.0	0.0	0.0
Roof Dead Load (psf)	2.0	2.0	2.0	2.0	2.0	2.0
Collateral (psf)	1.0	1.0	1.0	1.0	1.0	1.0
Snow Load (psf)	5	15	10	5	10	50
Snow Exp	Partial	Partial	Partial	Partial	Partial	Partial
Snow Imp	1.0	1.0	1.0	1.0	1.0	1.0
Wind Load (mph)	110	110	115	140	115	134
Wind Exp Cat	B	B	B	B	B	B
Enclosed Buildings, GCpi	±0.18	±0.18	±0.18	±0.18	±0.18	±0.18

Table 4. Seismic demand calculations for the metal building geographical location study

Code: IBC 2012, ASCE7 2010						
Occupancy: Normal (Risk Category II)						
Frame Type: OMF						
Location no.	1	2	3	4	5	6
County State	Riverside California	Lassen California	Mississippi Arkansas	Berkeley S. Carolina	Comanche Oklahoma	Anchorage Alaska
Seismic Imp Factor	1.0	1.0	1.0	1.0	1.0	1
Seismic Design Cat	D	D	E	D	C	D
Site Class	D	D	D	D	D	D
F _a	1.00	1.09	1.00	1.00	1.51	1.00
F _v	1.50	1.68	1.50	1.50	2.38	1.50
S _s	0.15	0.10	0.33	0.25	0.36	0.15
S ₁	0.60	0.36	0.13	0.71	0.10	0.67
S _{DS}	1.00	0.74	2.22	1.69	0.36	1.03
S _{D1}	0.60	0.40	1.26	0.71	0.17	0.67
R	3.5	3.5	3.5	3.5	3.5	3.5
Ω_o	2.5	2.5	2.5	2.5	2.5	2.5
C_D	3.0	3.0	3.0	3.0	3.0	3
ρ	1.3	1.3	1.3	1.3	1.3	1.3
T	0.392	0.392	0.392	0.392	0.392	0.392
C_s	0.2857	0.2126	0.2857	0.2857	0.1212	0.2857

The influence of geographical location on metal building design is quantified with the ratio M_E/M_G and M_W/M_G where M_E is the maximum bending moment at the knee location resulted from load combinations including earthquake loads, and M_W is the maximum bending moment at the knee location from load combinations including wind loads, and M_G is the maximum bending moment at the knee location resulted from load combinations not including earthquake loads.

The M_E/M_G ratios summarized in Table 5 show that earthquake loading combinations only control the design of building (D) in locations 1, 3, and 4, see $M_E/M_G=1.03$. The designs of all other buildings and locations are not controlled by seismic load combinations when using $R=3.5$ and a redundancy factor of $\rho=1.3$. Wind loading conditions never control in the selected designs and locations. Gravity load combinations, including snow, are always more critical. The location 6 design (Anchorage, Alaska) stands out because of the heavy snow load and relatively large member sizes.

An important conclusion from this location study is that building mass is an influential parameter when seismic demands control the design. For example, compare $M_E/M_G=0.62$ for a light modular building (Building C) at location 1 to $M_E/M_G=1.03$ for a heavy modular building (Building D) at the same location. These trends and observations are considered when selecting the seismic building index archetypes in the next chapter.

Table 5. Archetype building design comparison (M_E/M_G , M_W/M_G) and member size comparison

Location no.	1	2	3	4	5	6
County	Riverside	Lassen	Mississippi	Berkeley	Comanche	Anchorage
State	California	California	Arkansas	S. Carolina	Oklahoma	Alaska
Bldg A						
100x100x25 light wall						
M_E/M_G ($\rho=1.3$)	0.43	0.33	0.48	0.46	--	0.31
M_W/M_G ($\rho=1.3$)	0.36	0.30	0.41	0.78	--	0.26
M_E/M_G ($\rho=1.0$)	0.40	0.31	0.44	0.42	0.31	0.28
M_W/M_G ($\rho=1.0$)	0.36	0.30	0.41	0.78	0.68	0.26
Knee Web Depth (in)	41	41	41	41	41	52
Knee Flange Width (in)	6	8	6	6	6	8
Knee Flange Thickness (in)	0.75	1	0.75	0.75	0.75	1
Apex Web Depth (in)	17.5	20	17.5	17.5	17.5	26
Apex Flange Width (in)	6	6	6	6	6	8
Apex Flange Thickness (in)	0.5	0.5	0.5	0.5	0.5	0.625
Bldg B						
100x100x25 heavy wall						
M_E/M_G ($\rho=1.3$)	0.82	0.56	0.86	0.86	--	0.5
M_W/M_G ($\rho=1.3$)	0.51	0.43	0.54	0.76	--	0.22
M_E/M_G ($\rho=1.0$)	0.7	0.49	0.74	0.74	0.5	0.44
M_W/M_G ($\rho=1.0$)	0.51	0.43	0.54	0.76	0.56	0.22
Knee Web Depth (in)	55	47	58	59	38	58
Knee Flange Width (in)	8.25	8.25	8.25	8.25	6.25	8.5
Knee Flange Thickness (in)	0.25	0.25	0.275	0.275	0.22	0.313
Apex Web Depth (in)	27	23	27	27	27	33
Apex Flange Width (in)	6.25	6.25	6.25	6.25	5.38	6.5
Apex Flange Thickness (in)	0.125	0.125	0.125	0.125	0.125	0.188
Bldg C						
200x200x15 3 span modular light wall						
M_E/M_G ($\rho=1.3$)	0.62	0.51	0.64	0.61	--	0.55
M_W/M_G ($\rho=1.3$)	0.54	0.54	0.52	0.6	--	0.66
M_E/M_G ($\rho=1.0$)	0.54	0.45	0.56	0.54	0.35	0.48
M_W/M_G ($\rho=1.0$)	0.54	0.54	0.52	0.6	0.52	0.66
Knee Web Depth (in)	31	30	31	31	31	40
Knee Flange Width (in)	6	5	5	5	5	6
Knee Flange Thickness (in)	0.25	0.25	0.25	0.25	0.25	0.3125
Apex Web Depth (in)	22	26	22	22	22	25
Apex Flange Width (in)	5	5	5	5	5	6
Apex Flange Thickness (in)	0.25	0.25	0.25	0.3125	0.3125	0.3125
Bldg D						
200x200x15 3 span modular heavy wall						
M_E/M_G ($\rho=1.3$)	1.03	0.87	1.03	1.03	--	0.83
M_W/M_G ($\rho=1.3$)	0.56	0.64	0.62	0.62	--	0.71
M_E/M_G ($\rho=1.0$)	1.03	0.82	0.95	0.96	0.77	0.76
M_W/M_G ($\rho=1.0$)	0.57	0.64	0.55	0.62	0.55	0.71
Knee Web Depth ($\rho=1.0$) (in)	23	30	23	28	25	36
Knee Flange Width ($\rho=1.0$) (in)	6	6	6	6	6	6
Knee Flange Thickness ($\rho=1.0$) (in)	0.5	0.375	0.5	0.375	0.5	0.5
Apex Web Depth ($\rho=1.0$) (in)	12	12	12	14	13	17
Apex Flange Width ($\rho=1.0$) (in)	6	6	6	6	6	6
Apex Flange Thickness ($\rho=1.0$) (in)	0.25	0.25	0.25	0.25	0.25	0.25

4. Metal Building Seismic Archetype Selection and Design

4.1. Archetype building dimensions and details

The metal building archetype performance group selected for seismic performance characterization are summarized in Figure 6. The four index archetypes - A1 to A4 are organized into heavy and light wall buildings, and short and long primary frame spans. Building dimensions are summarized in Table 6.

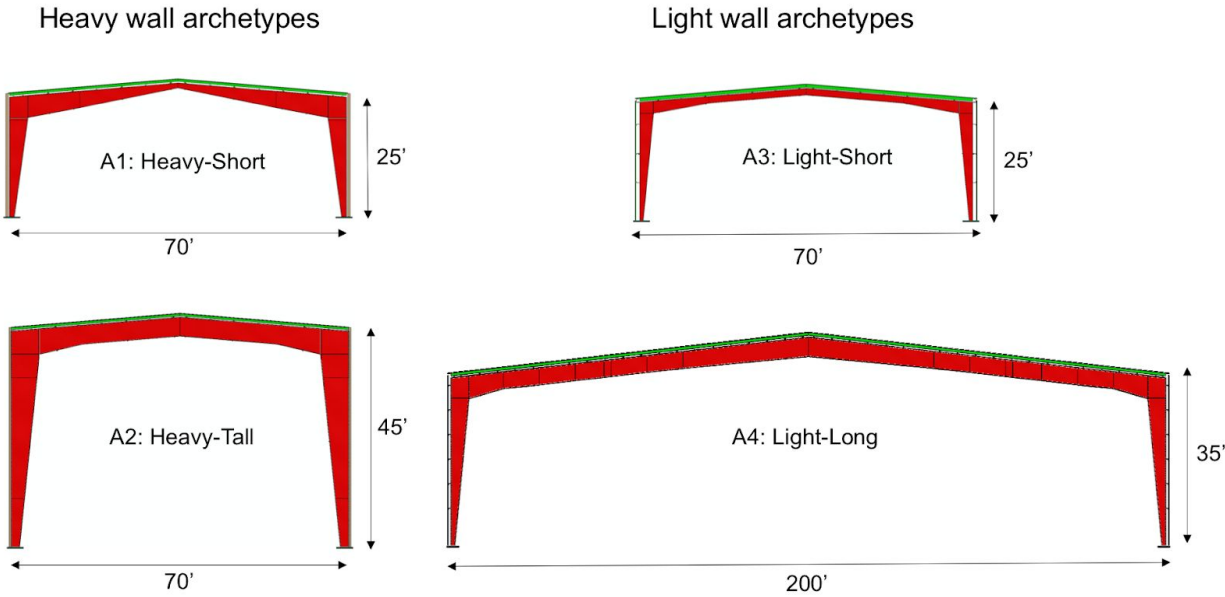


Figure 6. Metal building performance group made up of index archetypes

Table 6. Metal building index archetype dimensions and design loads

Parameters	Archetype			
	1	2	3	4
Building name	A1	A2	A3	A4
Building description	Heavy-Short	Heavy-Tall	Light-Short	Light-Long
Building dimensions	25'x70'x100'	45'x70'x100'	25'x70'x100'	35'x200'x200'
Bay spacing (ft)	25.0	25.0	25.0	25.0
Number of bays	4.0	4.0	4.0	4.0
Height of wall (ft)	25.0	45.0	25.0	35.0
Frame Span (ft)	70.0	70.0	70.0	200.0
Roof slope	1:12	1:12	1:12	1:12
Roof Dead Load (psf)	2.28	2.53	2.00	1.86
Self Weight (psf)	1.39	7.00	3.00	5.00
Collateral Load (psf)	7.00	7.00	7.00	7.00
Roof Live (reducible) (psf)	20.0	20.0	20.0	20.0
Snow Load psf	0.0	0.0	0.0	0.0
Rain Load (psf)	0.0	0.0	0.0	0.0
Wind speed (mph)	110.0	110.0	110.0	110.0
Wind Exposure Category	B	B	B	B
Enclosed GC _{pi}	± 0.18	± 0.18	± 0.18	± 0.18

Table 7. Metal building index archetype design assumptions

Design Method	ASD
Seismic load	Equivalent Lateral Force Procedure
Drift Limit	$\delta_x = H/40$
Metal Building Frame	MB-OMF Metal Building Ordinary Moment Frame
Seismic detailing specifications	Pinned Base, 3 plate members, No restriction on member compactness, No restriction on member splice locations, No restrictions on taper, pinch point, belly points, No special design of the panel zone
AISC 341 Seismic Provisions: Overstrength conditions	Design Knee Connection with $R=1.0$, Design Guide #16 Connection Type Design Column Axial Load only using Ω_o Forces Design Column Base Axial Load only using Ω_o Forces (Base PI, Anchor Rods, welding)
Material	Specified $F_y \leq 55$ ksi, $F_u \leq 70$ ksi
Welding	AWS D1.8 provisions, no protected zones
Anchor Rods	ASTM F1554 A36

4.2. Archetype building design parameters

Archetype buildings were designed by MBMA members using their design software with the parameters defined in Table 7. Seismic demands are considered without snow load combinations to provide a lower bound design for seismic performance evaluation. Roof purlins, girts, roof decks, diaphragm and lateral braces are designed for the average wind load in the United States ($V=110$ mph).

4.3. Archetype building seismic parameters (R , C_d , Ω_o)

The archetype metal buildings are designed with the seismic parameters in Table 8 for the Design Basis Earthquake (DBE) using ASCE 7-10 (ASCE 2010). The values chosen for the spectral response acceleration parameter at short periods, S_s , and for the spectral response acceleration parameter at a period of 1.0, S_1 , are based on recommendations provided in Chapter 5 of FEMA P695 for maximum values of spectral accelerations considering Seismic Design Category D . The redundancy factor, ρ , is assumed equal to 1.3 for all index archetype designs. This assumption is inconsistent with suggestions in FEMA P695 that $\rho=1.0$ when establishing R for a specific performance group, however $\rho=1.3$ is commonly chosen for metal buildings and is considered a baseline in this study. The metal building archetype gravity load and ELF lateral seismic force (V_b) are shown in Figure 7.

Table 8. Metal building index archetype seismic design parameters

Parameters	
Building Occupancy (Risk Category)	II
Seismic Importance Factor	1.0
Seismic Design Category	D
Site Class	D
F_a	1.0
F_v	1.5
S_s (g)	1.5
S_1 (g)	0.6
S_{DS}	1.0
S_{D1}	0.6
R	3.5
Ω_o	2.5
C_d	3.0
Redundancy factor (ρ)	1.3

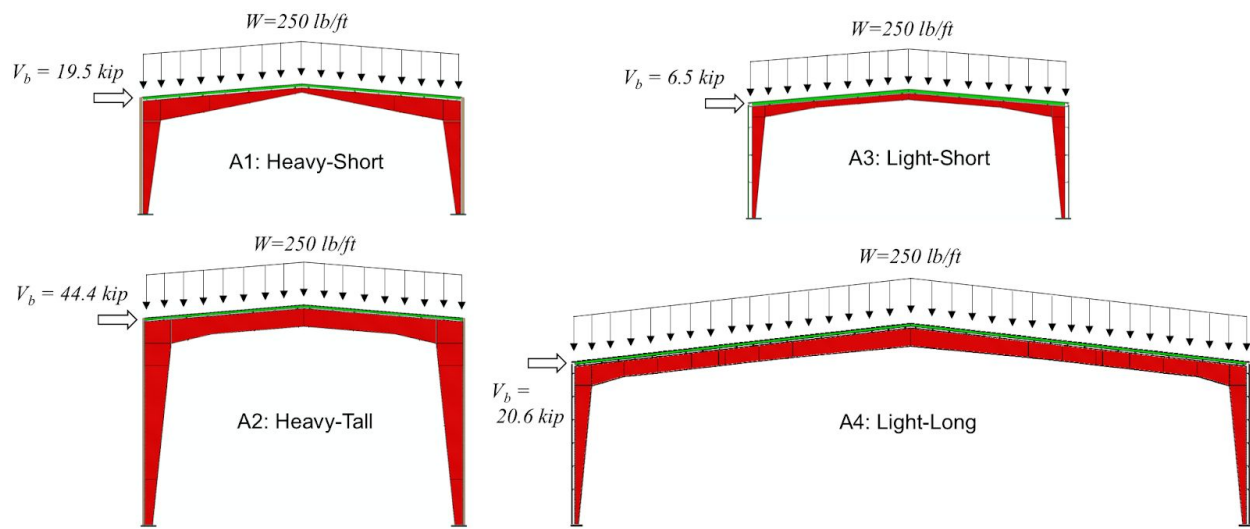


Figure 7. Metal building archetype gravity load and ELF lateral seismic force (V_b)

4.4. Archetype building performance evaluation strategy

With an archetype performance group now defined, the focus shifts to documenting and validating simulation capabilities that will be used to quantify metal building seismic performance within the FEMA P695 framework. The calculations and conclusions that follow should be considered only a partial treatment of the FEMA P695 process with only one performance group. A minimum of four performance groups are recommended by the FEMA guidelines - two seismic design levels and two period domains. Exploration of other performance groups, for example, modular buildings, is being considered as future work by MBMA.

A modeling protocol that can accurately simulate archetype cyclic building response to collapse, with computational efficiency, is essential for seismic performance evaluations within a probabilistic framework like FEMA P695. Modeling the unique load paths available in metal building systems (girts and purlins tying together primary frames with an outer skin) and sources of cyclic strength and stiffness degradation (local and lateral-torsional buckling deformation in tapered built-up frames) cannot be ignored. A high fidelity modeling protocol is introduced in the next chapter as a powerful tool for studying metal building system seismic performance.

5. High Fidelity Metal Building Modeling Protocol

5.1. The motivation for high fidelity simulation

This chapter describes the methodology to develop and validate a high fidelity modeling protocol that can directly predict the UCSD metal building seismic limit states - local and global buckling of the main frame controlled by discrete braces and localized yielding, buckling, and plastification of the panel zone. The protocol details, ranging from finite element types to residual stresses to connection modeling are all documented in the following sections.

5.2. Programming, platform, and choice of finite element software

All of the metal building models in this study are evaluated using the commercial finite element software ABAQUS (Simulia 2014). Many models are generated - both for validation and for the FEMA P695 archetype studies, which precludes the use of a Computer Aided Engineering (CAE) interface which would have been too slow and cumbersome. Instead, model generation was automated with Matlab functions (Mathworks 2016) written by NBM that take as inputs the anatomy of a 3D metal building - main frame flange sizes, tapers, purlin sizes and shapes, panel type, main frame flange bracing, and even frame-to-frame rod bracing, e.g., the horizontal roof truss diaphragm, and generate an ABAQUS .inp (input) file.

5.3. Main frame modeling

The main frame is modeled with 4-node S4R shell elements in ABAQUS, as shown in Figure 8, following mesh density guidelines defined in Schafer et al. (2010) that set a minimum of 4 nodes per local buckling half-wavelength. The flanges, webs, and panel zone stiffeners are rigidly linked at coincident nodes. Frame tapers and splice transitions, where plate widths and thicknesses change, are also considered with coincident nodal links.

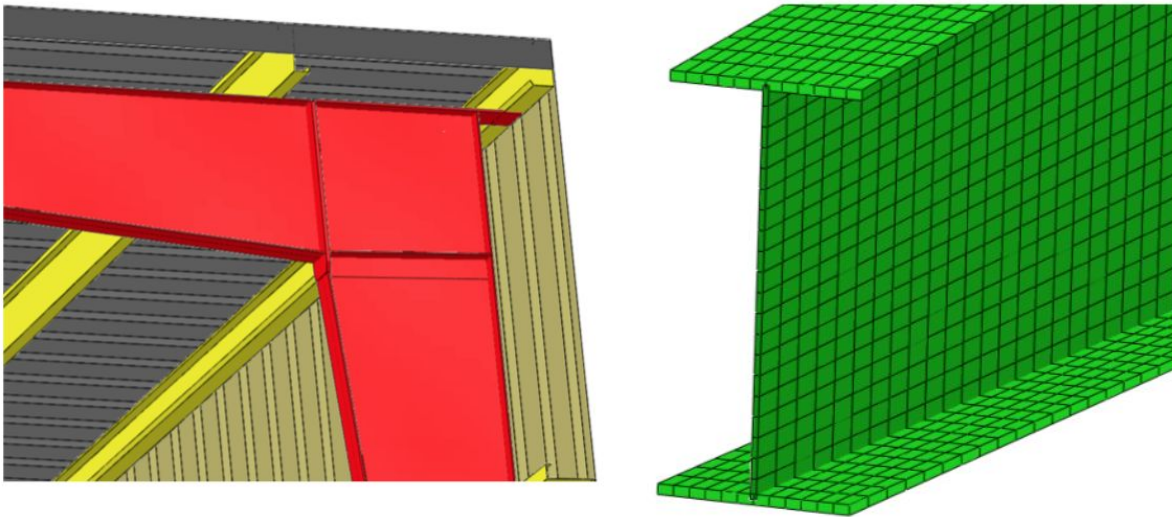


Figure 8. Typical high fidelity metal building model composition where every component is modeled with shell elements

The bolted end plate connection is not modeled with the bolts or pretensioning explicitly, but instead assumes a warping continuous connection. This assumption means that the rafter end plate and the knee end plate, also the column and knee plates, are modeled to always stay in contact assuming that the precompression from bolt tensioning across the surfaces is not exceeded during the simulations.

Main frame imperfections are input as a cross-sectional distortion at the distortional buckling half-wavelength with the maximum web imperfection as $\delta=h/250$ and where h is the depth of the web, as shown in Figure 9. A global out-of-plane sweep in the main frame span of $L/1000$ is also included based on measurements taken in the UCSD cyclic subassembly tests (Smith et al. 2013).

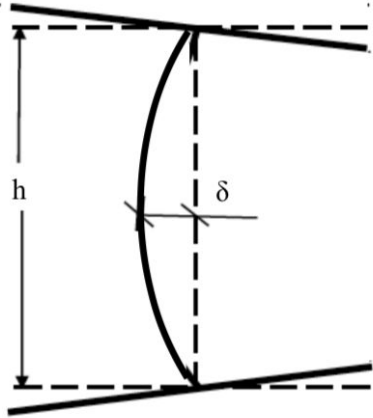


Figure 9. Main frame cross-sectional geometric imperfection pattern

Thermal self-equilibrating residual stresses are modeled in the main frames with the stress distributions in Figure 10. The stress magnitudes are chosen based on suggestions from Prawel (1974) and Kim (2010) for built-up steel members.

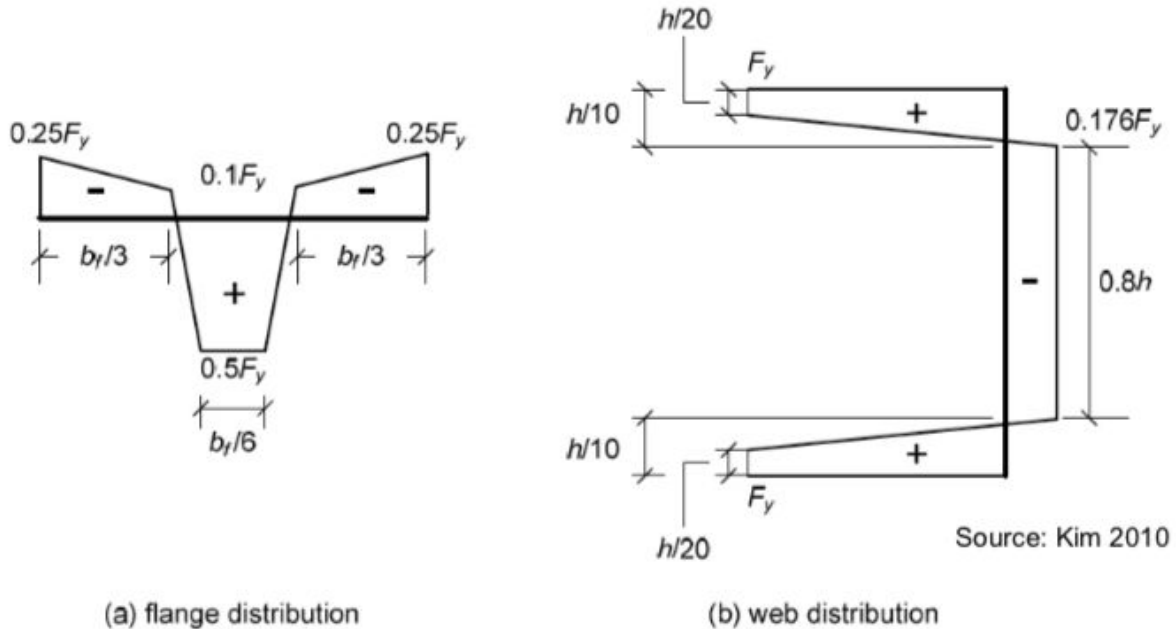


Figure 10. Main frame thermal residual stress pattern applied in high fidelity models

5.4. Modeling of purlins, girts, and eave struts

Purlins and girts are also modeled with S4R shell elements, with a cross-section node pattern extruded along the length as shown in Figure 11. The purlins are connected to the main frames with numerical constraints that link a group of nodes in the web and bottom flange of the secondary member to a group of nodes on the main frame flange. These constraints are an approximation of a typical clip connection. The girts and purlins are connected to the wall and roof panels by fasteners, where the fastener connection is modeled as a rigid constraint between coincident nodes. Initial geometric imperfections and residual stresses from manufacturing are not considered for any secondary members.

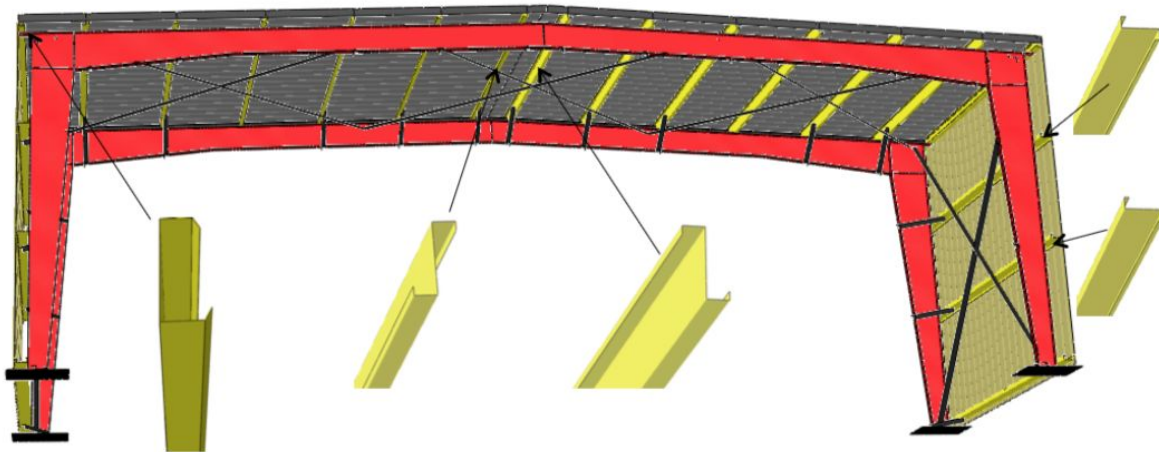


Figure 11. Girts, purlins and eave strut are modeled as shell elements

5.5. Rod brace and flange brace modeling

Rod bracing is modeled with B33 beam elements in ABAQUS and multi-point constraint (MPC) connections made at the web near the top flange, see the X-bracing in Figure 11 for an example. Flange brace angle cross-sections are extruded and modeled with S4R shell elements, and the brace ends are numerically constrained to node groups in the main frame flange and the purlin, again see Figure 11 for an example.

5.6. Roof and wall panel modeling

R-panel wall and roof sheeting are represented with S4R shell elements as shown in Figure 11. Side laps and end laps are assumed numerically continuous. Screw-fastened roofs are evaluated in this study, and each panel-to-purlin and panel-to-girt screw connection is modeled with a single node rigid multi-point constraint.

5.7. Steel material modeling

The steel constitutive law assumed for both primary and secondary structural systems (frame, girts, purlins) is shown in Figure 12. The steel yield stress is 55 ksi and the ultimate stress as 84 ksi. All quasi-static pushover models employ an isotropic material model where the Von Mises yield surface is stationary and expands to simulate strain hardening based on the stress-strain curve in Figure 12. All quasi-static and dynamic cyclic simulations employ an isotropic-kinematic plasticity model where the Von Mises yield surface both expands and shifts to include residual stresses that remain after elastic unloading (i.e., the Bauschinger Effect).

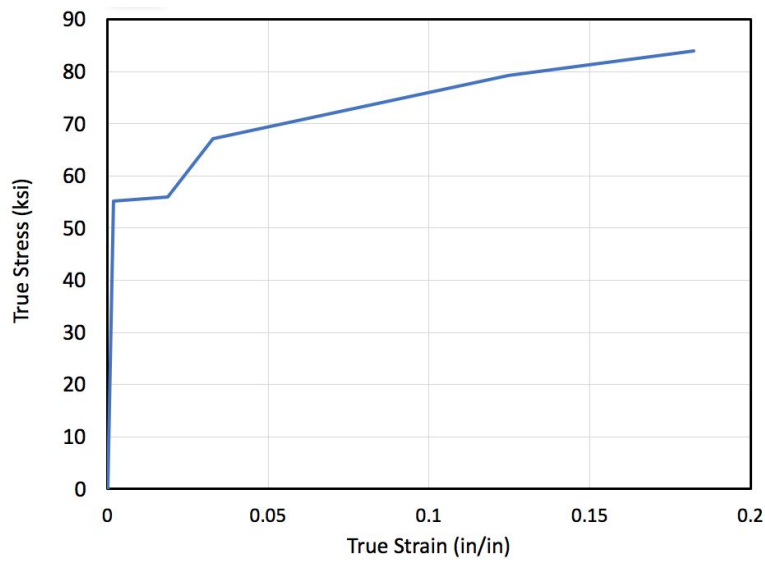


Figure 12. True stress-strain curve for both primary and secondary structural systems

5.8. Hard wall modeling

Concrete hard walls in index archetypes A1 and A2 are simulated in ABAQUS with S4R shell elements. The wall connection to the main frame is important to consider since a large proportion of the building inertial forces move through these connections. In the UCSD shake table tests, the hard walls were bolted to the main frame at midheight and at the eave, and these connections were modeled in ABAQUS as multi-point constraints assuming no contact or bearing elsewhere along the wall and frame.

The details at the bottom of the wall are also important to consider for modeling. Simulation studies showed that drift, acceleration, and natural period were all sensitive to the hardwall base connection. In the UCSD shake table experiments, the bottom of the precast concrete walls rested inside steel supports connected to the strong floor, as shown in Figure 13. These provided rotational restraint to the wall, and this stiffness is approximated with calculations shown in Figure 14.

Both weight of the wall and brackets counter act tipping of the wall.

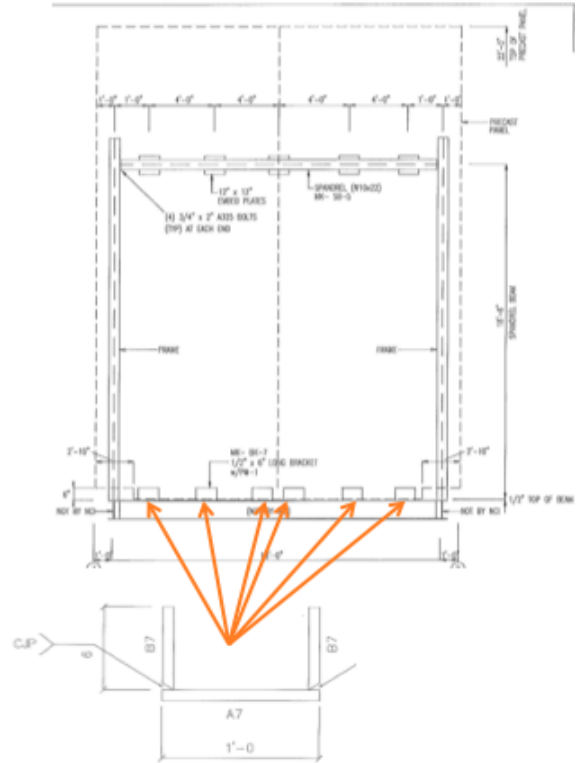
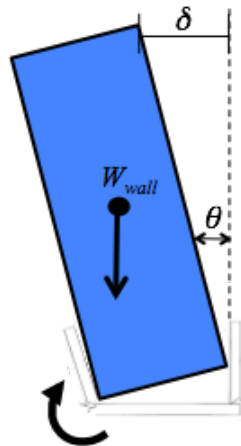
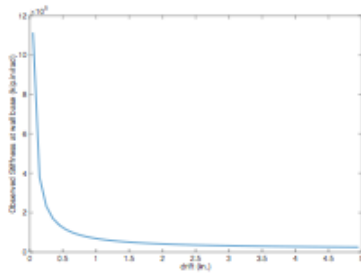
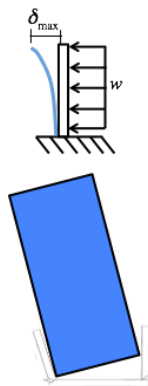


Figure 13. UCSD hard wall lower contact point modeled with a rotational spring that includes steel channel support stiffness and the pivot of the wall about the corner which cannot be modeled explicitly when using shell elements for the wall



$$I \text{ for each plate: } I = \frac{bh^3}{12} = \frac{6 \times 1^3}{12} = 0.0625 \text{ in}^4$$

$$EI \text{ for all plates: } EI_{tot} = 6 \times 29500 \times 0.0625 = 11062 \text{ kip} \cdot \text{in}^2$$

$$\delta_{max} = \frac{wL^4}{8EI}$$

$$\theta_{avg} = \frac{\delta_{max}}{L} = \frac{wL^3}{8EI}$$

$$M = \frac{wL^2}{2}$$

$$k_{rot} = \frac{M}{\theta_{avg}} = \frac{4EI}{L}$$

$$k_{rot} = 7375 \text{ kip} \cdot \text{in} / \text{rad}$$

Figure 14. The rotational restraint provided by the steel supports holding the hard wall base in the UCSD shake table experiments was calculated assuming that each vertical leg of the support acted as a cantilever

Another consideration is that the UCSD hard walls were chosen to be modeled with shell elements which means that the point of rotation of the wall is defined at the wall centerline, even

though the wall rotates about the wall corner as it bears into the floor; see Figure 13 for a drawing of the kinematics. The distance between the wall centerline and the wall corner results in a restoring moment. A nonlinear spring was placed at the base of the hard walls to account for both the steel support rotational restraint and the wall restoring moment with the magnitude defined in Figure 15. An improvement in future models could be to model the hard walls with solid finite elements if the bottom corner contact point is deemed important to seismic response.

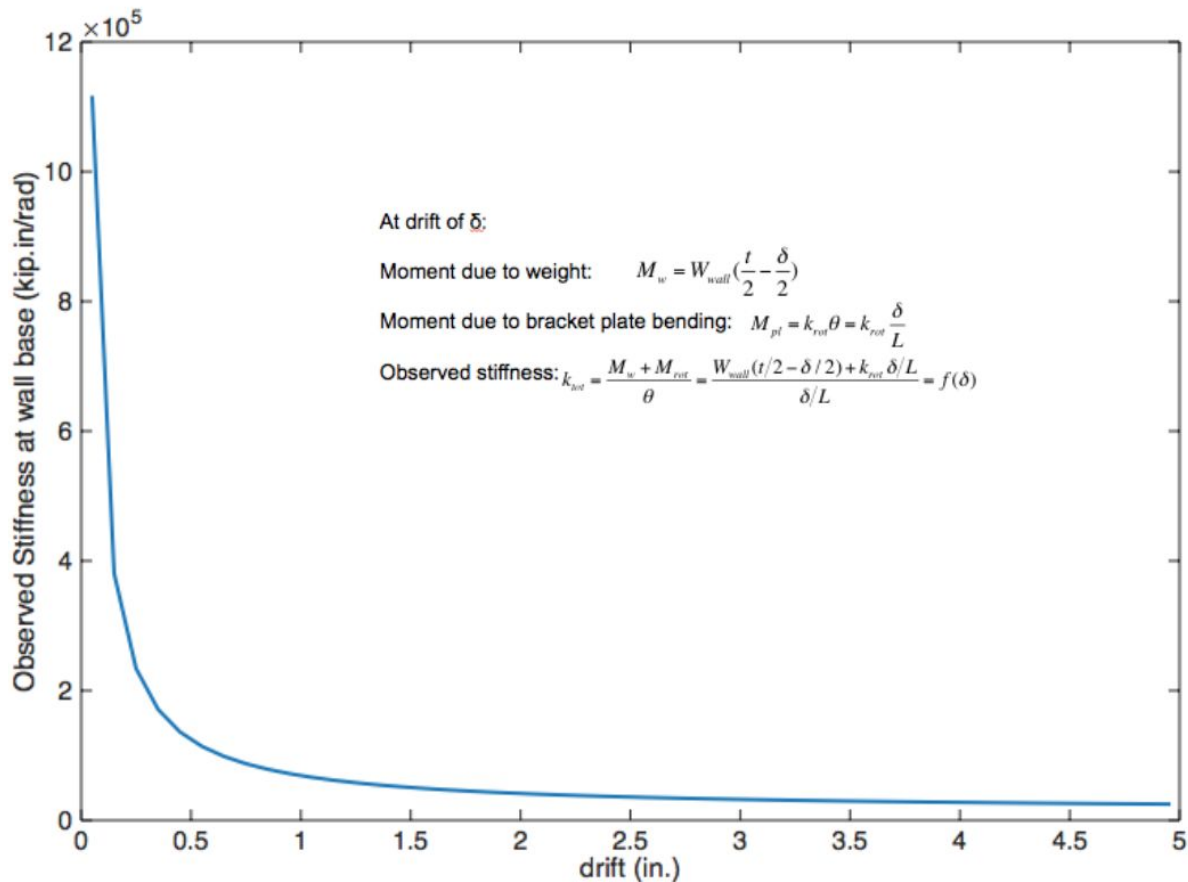


Figure 15. Nonlinear rotational stiffness applied at the hard wall base that simulates the combination of rotational restraint from the steel supports and the restoring moment from the wall mass as it rotates about a corner

5.9. Roof mass modeling

To account for the adjacent half-bay loads and mass, additional plates were added to the main frames in the UCSD shake table tests with bolted connection to the main frame top flange

through the roof panels. This mass was modeled in ABAQUS by increasing the density of the frame top flanges; see the blue color in Figure 16.

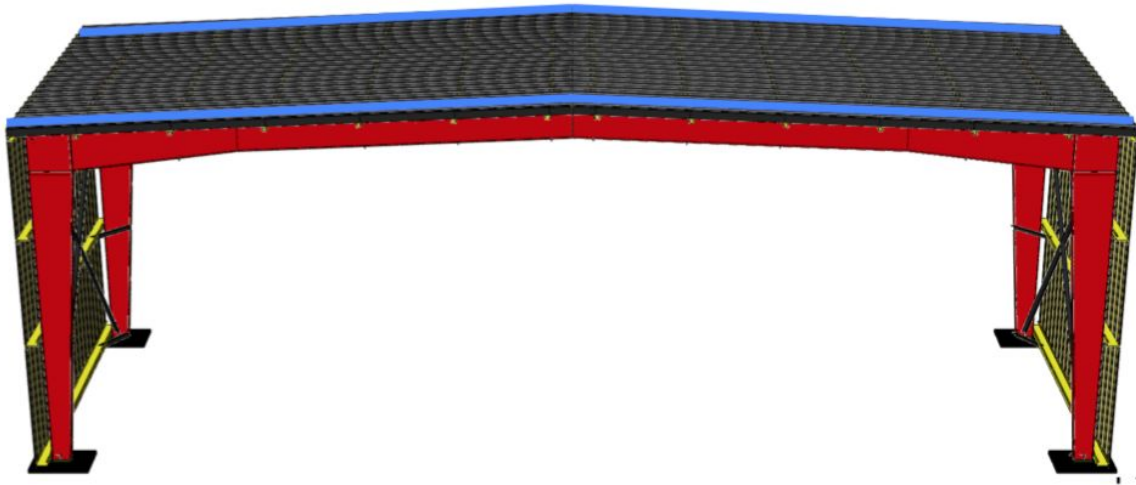


Figure 16. Roof mass in the UCSD shake table tests was simulated by increasing the density of the main frame top flanges

5.10. Mezzanine modeling

The key differentiating detail in UCSD shake table Specimen B3 was a mezzanine, and this was modeled with B33 beam elements assuming pinned frame-to-frame connections as shown in Figure 17. A concrete floor slab rested on the horizontal framing members at 4 points in the experiments, and this slab was modeled with S4R shell elements to capture the influence of the midheight floor mass in the simulated building performance.

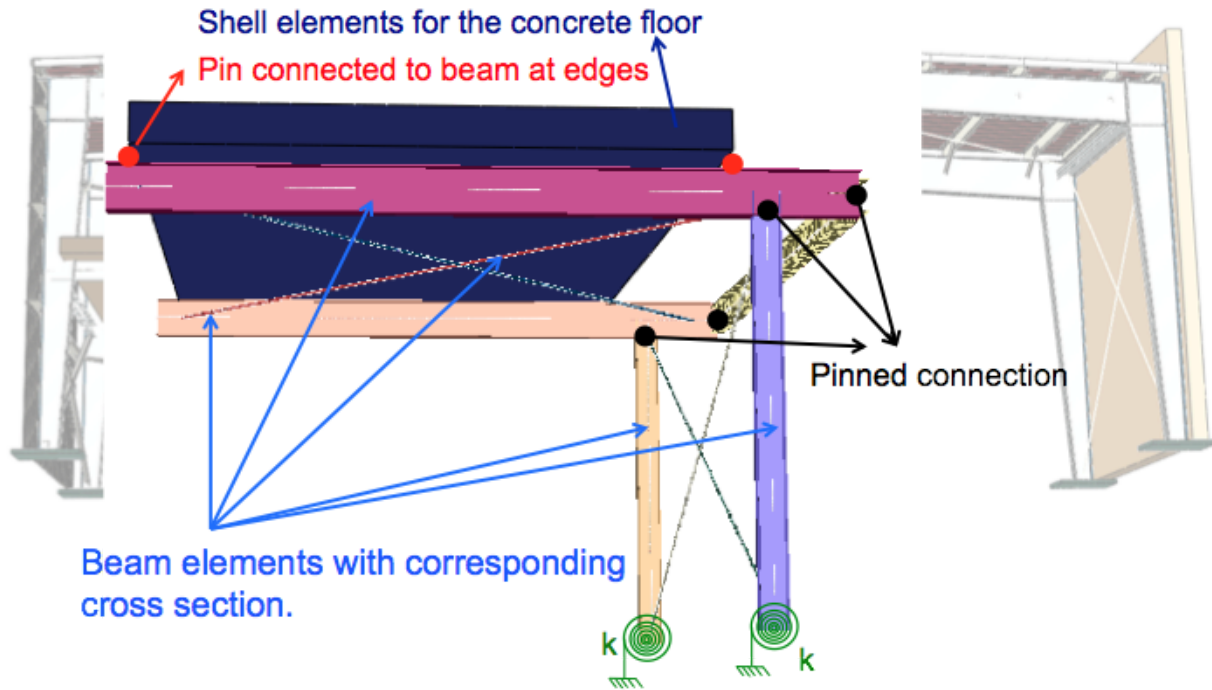


Figure 17. UCSD shake table Specimen B3 mezzanine modeling details

5.11. Primary frame baseplate modeling

The connection of the main frame column to the foundation in a metal building are typically made with an anchored baseplate, and this baseplate provides rotational stiffness that affects the building dynamic properties and seismic response. Significant effort was expended in this project to develop a realistic moment-rotation response that could be used to verify the simulation protocol with the UCSD shake table tests.

Baseplate connection modeling is always a challenge because it includes pretensioned anchor rods and a plate in contact with the foundation. In the UCSD project, this complexity was compounded by the ‘research’ style details required to connect the specimen to the shake table strong floor. Notably, due to the limitation of the UCSD shake table footprint, a steel base frame is used as the building foundation. Also, the Specimen B1 baseplate experienced damage and had to be retrofitted. Specifically, anchor rods fractured in the first Specimen B1 Imperial Valley tests and so some of the B1 test results have undamaged baseplate connections and some have damaged connections, and some were run with a repaired baseplate connection. See Figure 18 for a summary.

Period is shifting from test to test even when there is not damage to the building. Period shift is a result of baseplate failure that occurred after IV100% tests.

Table 5.2 Specimen 1 Identified Dynamic Characteristics

Test	T_1 (sec)	ζ_1 (%)
Impulse (Initial)	0.395	2.2
White Noise (Initial)	0.388	1.9
Impulse (after 25% Tests)	0.384	1.6
Impulse (after IV50)	0.390	1.7
Impulse (after IV100)	0.432	1.8
White Noise (after IV100)	0.437	2.1
Impulse (after IV150)	0.438	2.4
Impulse (after IV200)	0.480	2.5
Impulse (after IV250) ¹	0.502	2.1
Impulse (after IV250) ²	0.464	2.1
Impulse (after IV300)	0.532	1.9

Anchor failure during IV150.
Base plate repaired using welds.

Base plates repaired again.

¹ Prior to base plate weld repairs
² After base plate weld repairs

UCSD draft report to MBMA

Figure 18. UCSD shake table base plate submodel used to generate response curve for baseplate nonlinear rotational spring

Submodels of the bolted baseplate and primary frame column were created to identify the nonlinear moment-rotation response including yielding of the baseplate as shown in Figure 19. The baseplate is modeled with solid elements, surface contact (to prevent penetration of the elements into each other), and the anchor rods or bolts are represented as axial springs.

Surrogate baseplate model

Separate FE model

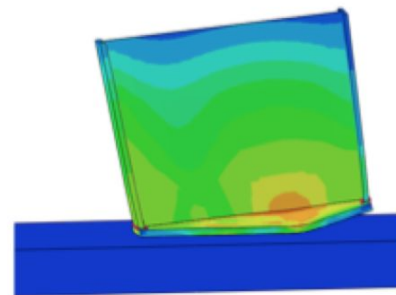
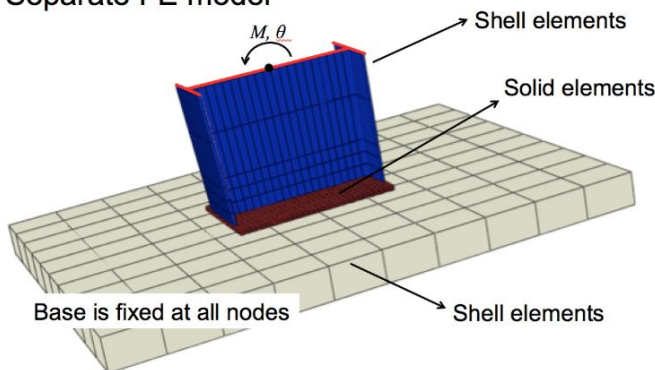


Figure 19. UCSD shake table base plate submodel used to generate response curve for baseplate nonlinear rotational spring

A summary of the UCSD Specimen B1 baseplate simulated response is provided in Figure 20. Damage in the Specimen B1 connections was assumed to initiate at a rotation of 0.0175 radians. Tests performed with a fully damaged baseplate were represented by reducing the load levels along the backbone by one-third. The baseplate response is modeled in the full building models as a nonlinear rotational spring. Hysteretic models with energy dissipation for the baseplate are not included because reliable test data was not available.

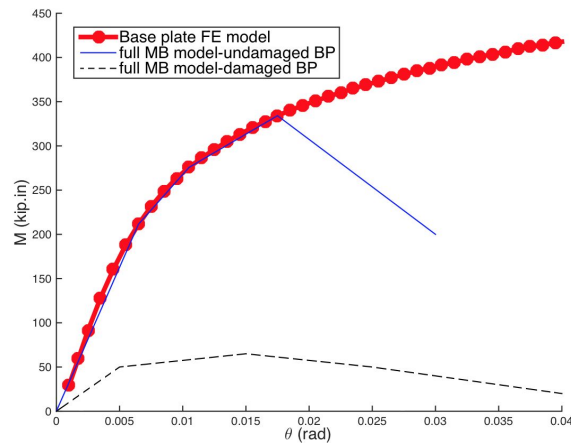


Figure 20. UCSD Specimen B1 baseplate moment-rotation curve considering undamaged, damage initiation during loading, and damage

The B1 damage resulted in the redesign of the connections for Specimens B2 and B3, moving from anchor rods to A490 bolts which increased the connection stiffness as shown in Figure 21. The same damage model, i.e., reducing the backbone moment magnitudes by a third, was employed for the redesigned connections (B2 was damaged at IV100 and B3 was damaged at IV150).

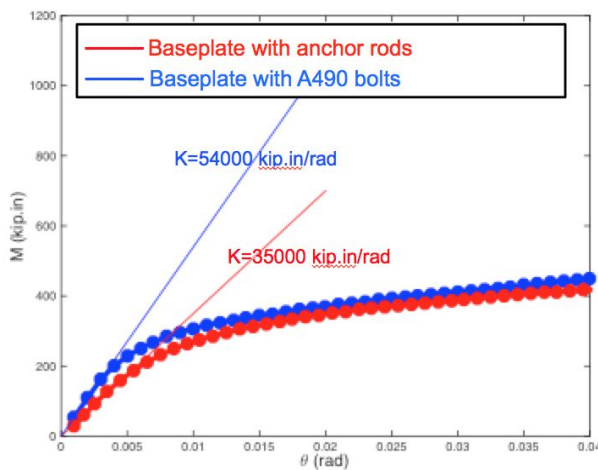


Figure 21. UCSD Specimen B2 and B3 baseplate initial stiffness considering A490 bolts instead of the Specimen B1 anchor rods

5.12. Modeling protocol summary

It is estimated that more than half of the effort by NBM engineers on this project was dedicated to developing this high fidelity cyclic modeling capability for metal buildings. The heavy emphasis highlights how important and valuable a 'real life' simulation capability can be to an industry, both for understanding current systems and for innovating with new systems. The fruits of this modeling labor become evident in the next section, where simulated experiments considering all the geometry and physics defined in the modeling protocol predict consistent tested response for both UCSD cyclic frame subassembly tests and shake table tests without calibration or empirical adjustments.

6. Validation of the High Fidelity Metal Building Frame Modeling Protocol

6.1. High fidelity simulation of selected UCSD cyclic lateral-torsional buckling tests

Benchmark quasi-static cyclic frame subassembly tests (Smith et al. 2013) were selected to demonstrate that high fidelity simulation can capture hysteretic response including strength and stiffness degradation developing from lateral-torsional buckling. The cyclic subassembly benchmark test setup is shown in Figure 22, where a reusable loading column was bolted to rafter specimens with different geometry and bracing configurations. The cyclic loading protocol followed AISC 341 recommendations (AISC 2010).

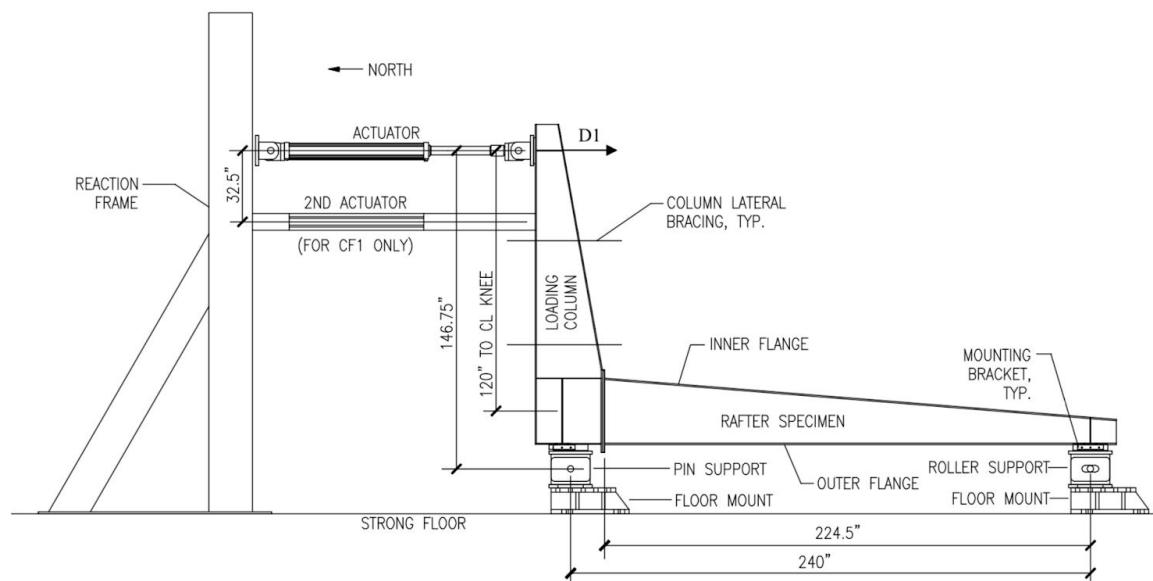


Figure 22. UCSD main frame rafter-column test setup used to study lateral-torsional buckling between inner flange discrete brace points

The specimens utilized for the high fidelity model benchmarking are PF2 and CS3. Specimen PF2 in Figure 23 is distinctive because it has a tapered pinch point within the 'CS' zone where lateral torsional buckling is expected. The frame cross-section is singly symmetric (inner flange is thicker than the outer flange), the flanges are locally noncompact, and the web is locally slender according to AISC definitions.

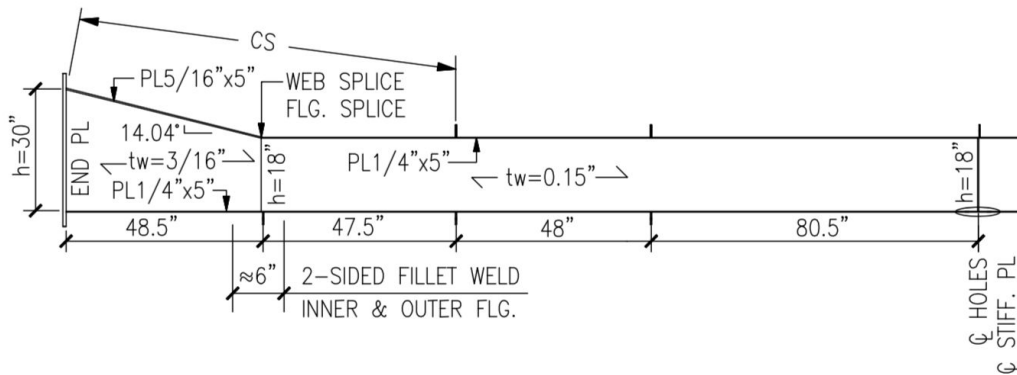


Figure 23. UCSD specimen PF2 details with a mostly untapered web and unbraced length (marked as CS) that contains the welded taper transition

The hysteretic response for specimen PF2 in Figure 24 is asymmetric with lower peak strength and noticeable stiffness degradation in the upper right quadrant where the inner flange was in compression. The stiffness degradation resulted from inner flange lateral-torsional buckling deformation that led to flange local buckling in the first 2% drift cycle. The lower left hand quadrant (outer flange in compression) maintained stiffness from cycle to cycle after some strength loss from flange local buckling leading up to 3% drift. Stiffness decreased in later cycles when the inner flange welded splice cracked at a 5% drift cycle.

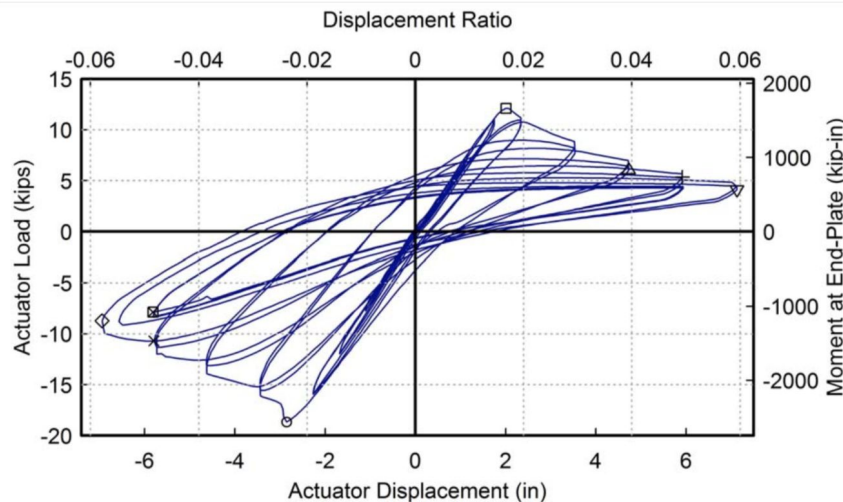


Figure 24. UCSD specimen PF2 cyclic load deformation response where the upper right quadrant shows the stiffness and strength degradation in the compressed main frame inner flange from lateral-torsional buckling localizing at the web taper

The CS3 specimen is different from the PF2 test because there is a constant taper, with no kink, in the beam part of the main span as shown in Figure 25. The cross-section is doubly symmetric, the flanges are compact, and the web is locally slender. Inner and outer flange

splices were added at the middle of the expected lateral-torsional buckling zone (the CS zone in Figure 25).

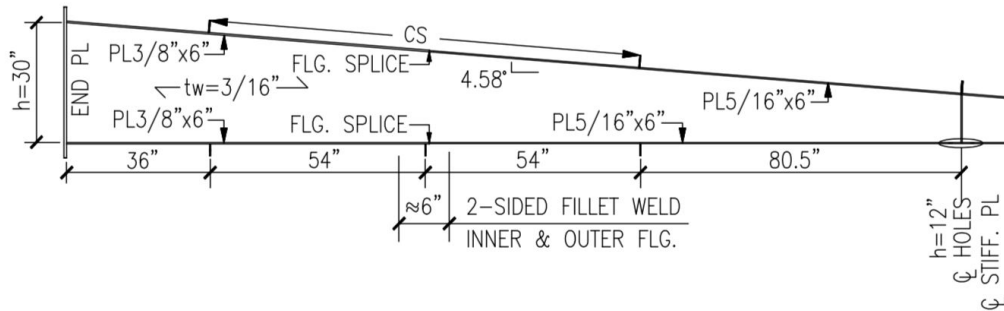


Figure 25. UCSD specimen CS3 details with a constant web taper and unbraced length (marked as CS) towards the quarter-point of the main frame span

Significant lateral-torsional buckling deformation developed as two half-waves in the inner flange at a drift of 3.5% which resulted in a rapid strength drop in the following cycles, as shown the upper right hand quadrant in Figure 26. Outer flange local buckling near the bolted end plate initiated at 4% drift, resulting in the strength decay in lower left hand quadrant. Strength and stiffness degradation from local buckling was much less than strength degradation from lateral-torsional buckling. No fracture was observed at the welded splices.

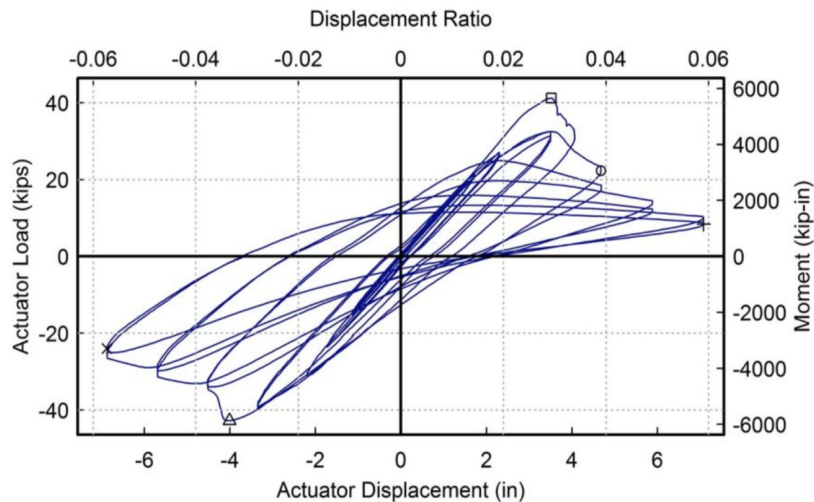


Figure 26. UCSD specimen CS3 cyclic load deformation response where the upper right quadrant shows similar stiffness and strength degradation to specimen SP2 along with a drop in strength from flange local buckling in the lower left hand quadrant at 4 in.

The high fidelity simulation protocol is able to capture the hysteretic influence of this observed local and global buckling in specimens PF2 and CS3 as shown in Figure 27 and Figure 28. Local buckling in specimen PF2 is predicted at consistent rotation demands to those applied in the experiments (Figure 29). Asymmetric load-deformation response from lateral-torsional buckling deformation that develops in specimen CS3 is also predicted (Figure 30) only in the inner flange because of the discrete flange brace spacing.

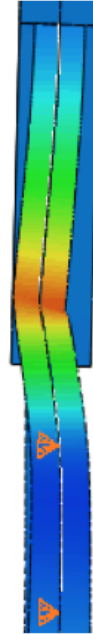
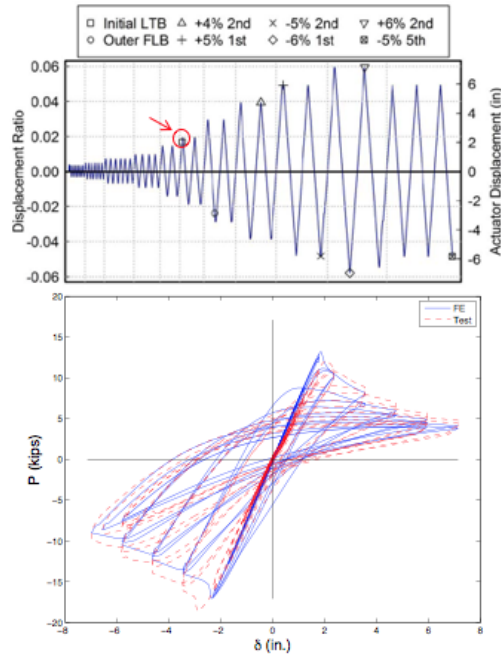


Figure 27. Initial LTB: UCSD Specimen PF2 subject to AISC 341 cyclic loading protocol versus high fidelity FE model results

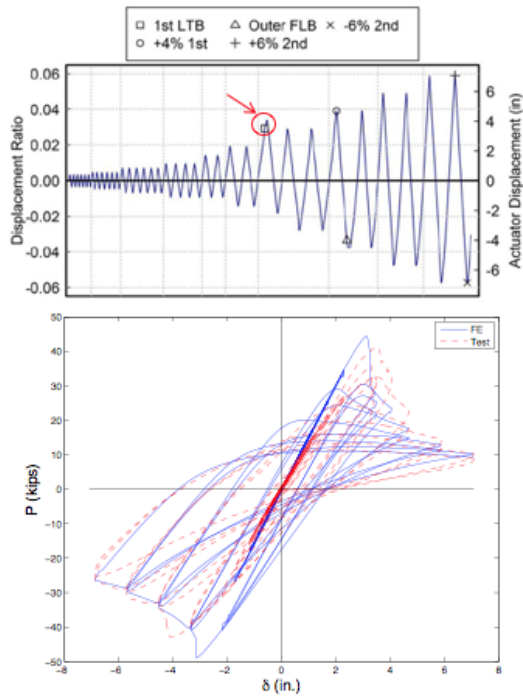


Figure 28. 1st LTB: UCSD Specimen CS3 subject to AISC 341 cyclic loading protocol versus high fidelity FE model results

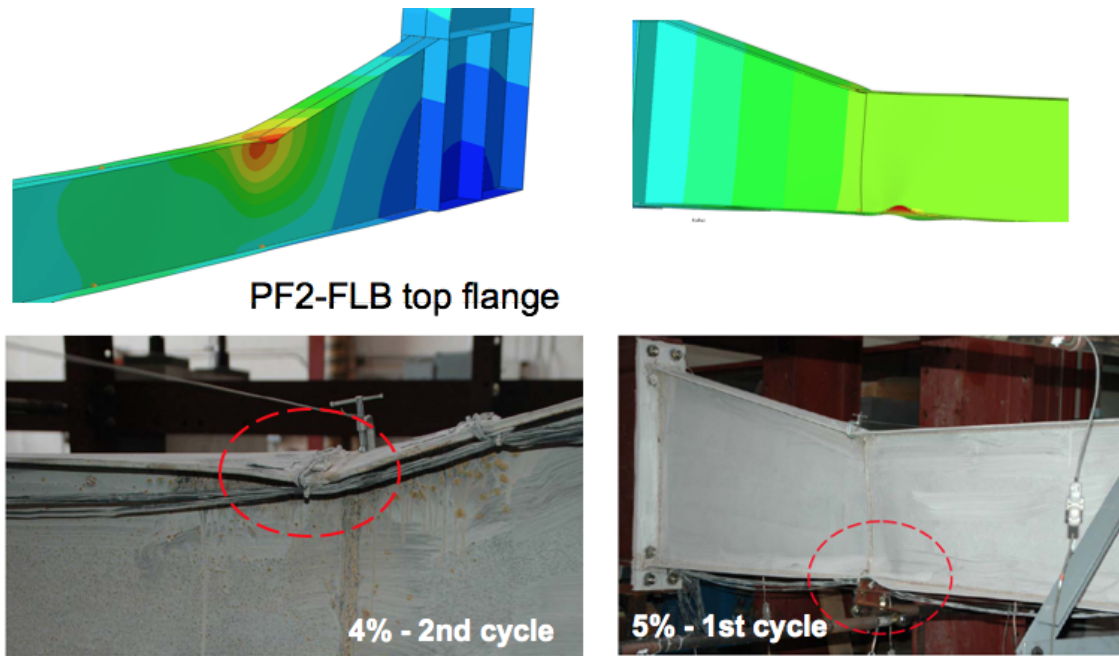


Figure 29. Top and bottom flange local buckling at 4% and 5% applied rotation: UCSD Specimen PF2 subject to AISC 341 cyclic loading protocol versus high fidelity FE model results

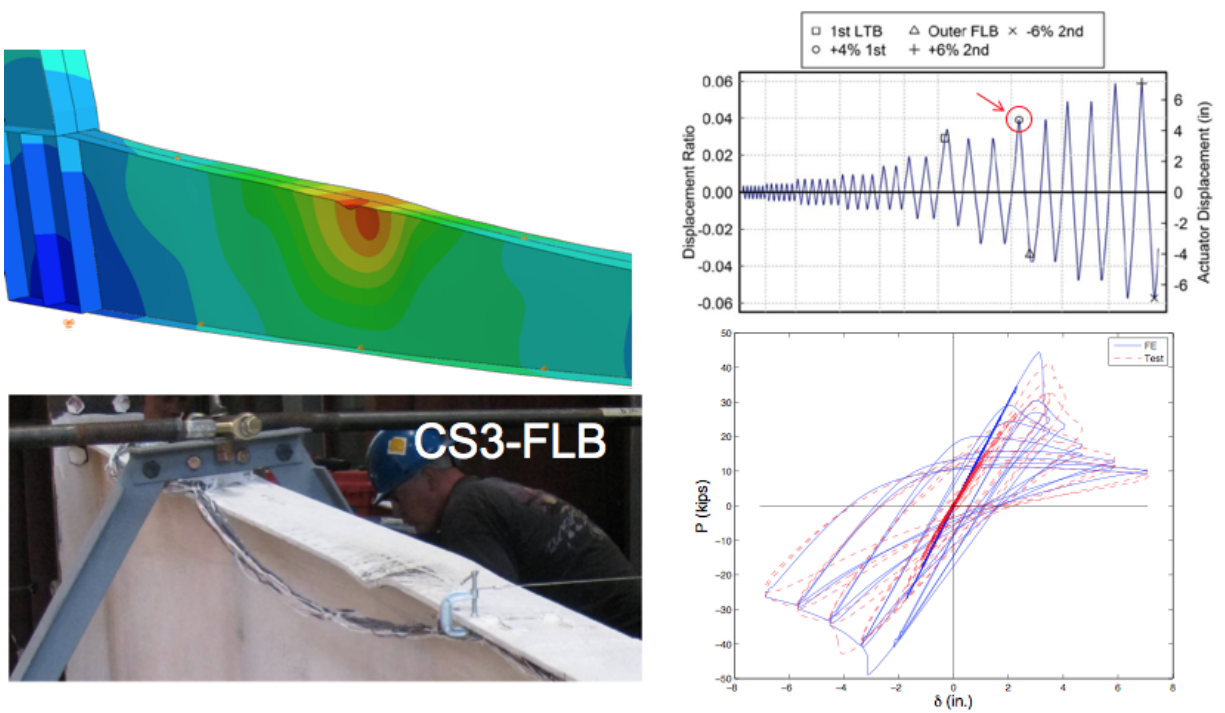


Figure 30. Flange local buckling at 4% (1st cycle) applied rotation: UCSD Specimen CS3 subject to AISC 341 cyclic loading protocol versus high fidelity FE model results

6.2. High fidelity simulation of selected UCSD shake table tests

Simulated tests of UCSD shake table Specimens B1 (light wall), B2 (heavy wall), and B3 (mezzanine) are performed with the high fidelity simulation protocol introduced in Chapter 5. High fidelity incremental dynamic analysis (IDA) is not used for the seismic evaluations later in the report (nonlinear SDOF is chosen instead for higher computational efficiency), however IDA is still interesting to explore because it highlights high fidelity modeling capabilities at the boundaries of high performance computing.

UCSD Shake Table Specimen B1

The UCSD Specimen B1 light wall configuration shown in Figure 31 was selected as a benchmark for exploring the high fidelity modeling protocol because it is considered a ‘control’ or baseline archetype in the UCSD test matrix. White noise tests determined that the first natural period of the building specimen was 0.39 seconds and the Design Basis Earthquake (DBE) ground motion scaling factors were defined based on this period.

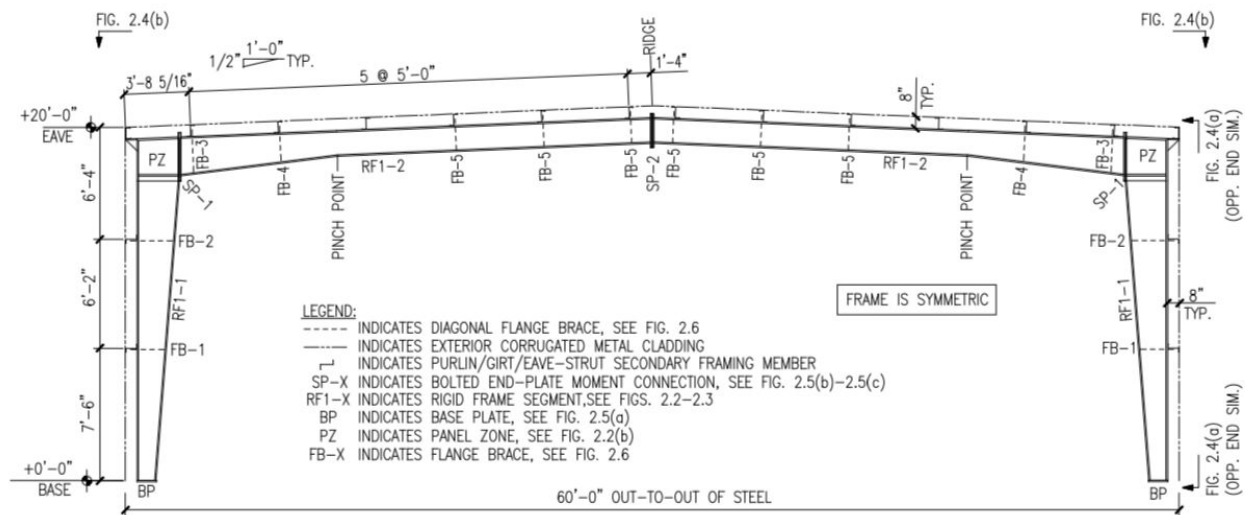


Figure 31. UCSD light wall shake table Specimen B1 made up of two parallel main frames connected with girts, purlins, and panels

The ground motion magnitudes were scaled from IV50 up to IV300, i.e., from 50% to 300% of the DBE for the Imperial Valley earthquake record. No damage was observed in the specimen and the load-deformation response remained mostly elastic (Figure 30) until the IV250 test when lateral-torsional buckling initiated at the frame inner flange web taper transitions. The buckling caused purlin tearing where the flange brace connected and led to a crack from the inner flange up through the web at the taper point with local folding developing from large lateral cyclic deformation. Drift levels up to 3% (7 in.) were accommodated without signs of collapse.

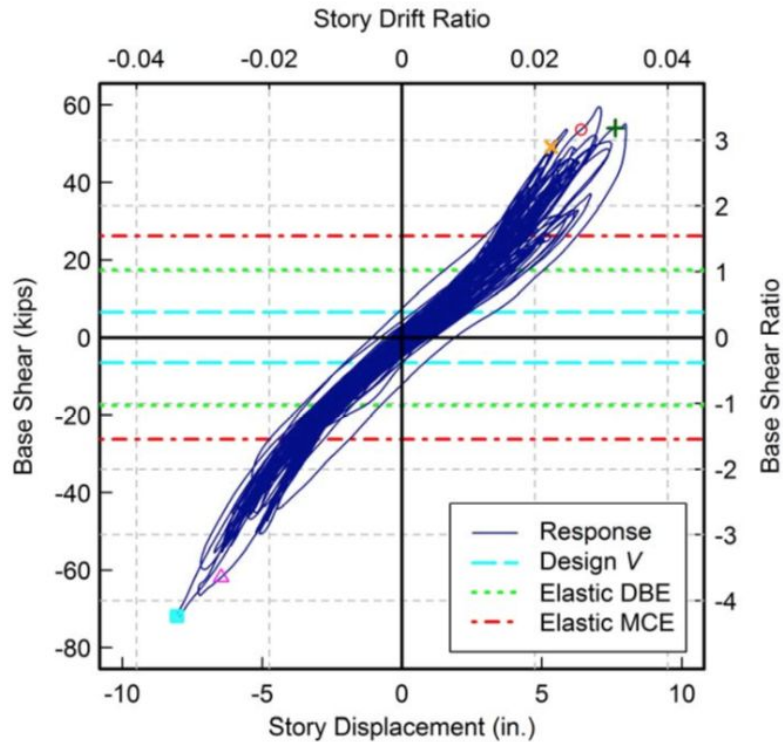


Figure 32. UCSD Specimen B1 tested light wall cyclic response with all loadings from IV50 to IV300 overlaid exhibits a mostly elastic response even at large drifts

The nonlinear response history test results and high fidelity simulation response are compared for Specimen B1 in Figure 32. The acceleration and displacement (drift) time history responses are consistent in some time domain regions and inconsistent in others, see results for IV100 in Figure 33 and IV250 in Figure 34. The spectral response analyses are similar at IV100 and IV250 which means that the simulated model dynamic properties (mass, stiffness, natural period) are consistent with the test and that the period shift caused by damage is also represented in the simulation. Even with the inconsistencies between tested and simulated time history responses, the high fidelity IDA predicts maximum tested drift well, as summarized in Table 9. The dominant source of cyclic strength and stiffness degradation, lateral-torsional buckling at the northeast frame pinch point in Figure 35, is also predicted to occur at the same frame location and a similar time in the ground motion record.

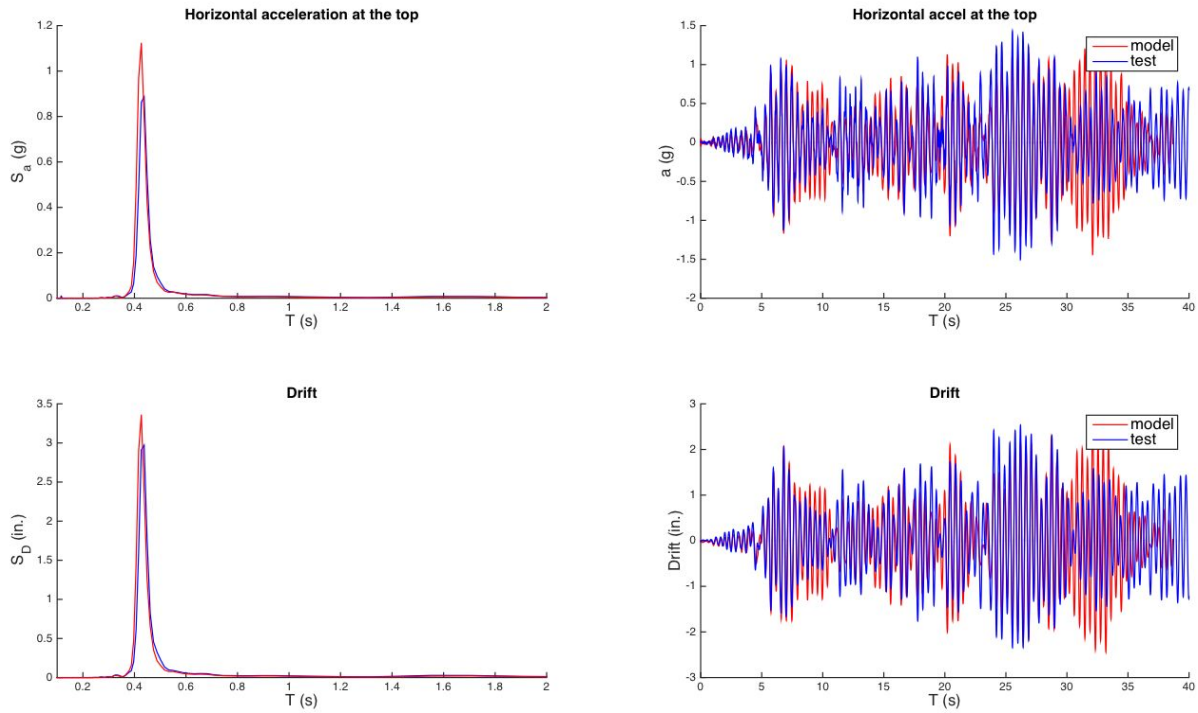


Figure 33. UCSD shake table specimen B1 acceleration and displacement (drift) spectral and time history response for high fidelity simulation and tests at IV100

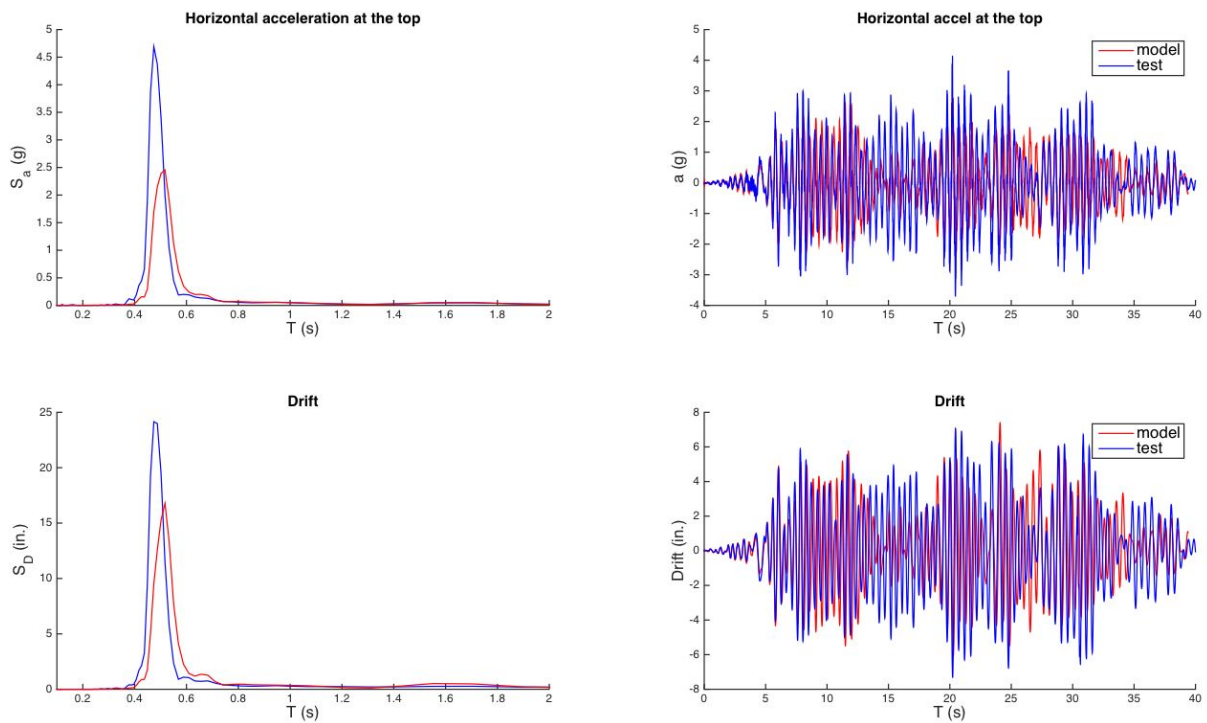


Figure 34. UCSD shake table specimen B1 acceleration and displacement (drift) spectral and time history response for high fidelity simulation and tests at IV250

Table 9. UCSD shake table specimen B1 natural period and maximum displacement (drift) test-to-predicted summary

Building	Record	Period test (s)	Period model (s)	Period test/predicted	Max drift test (in)	Max drift model (in)	Max drift test/predicted
B1	IV50	0.42	0.43	0.98	0.97	1.06	0.92
	IV100	0.44	0.43	1.02	2.54	2.61	0.97
	IV200	0.45	0.44	1.02	5.71	5.71	1.00
	IV250	0.47	0.52	0.90	7.31	7.40	0.99

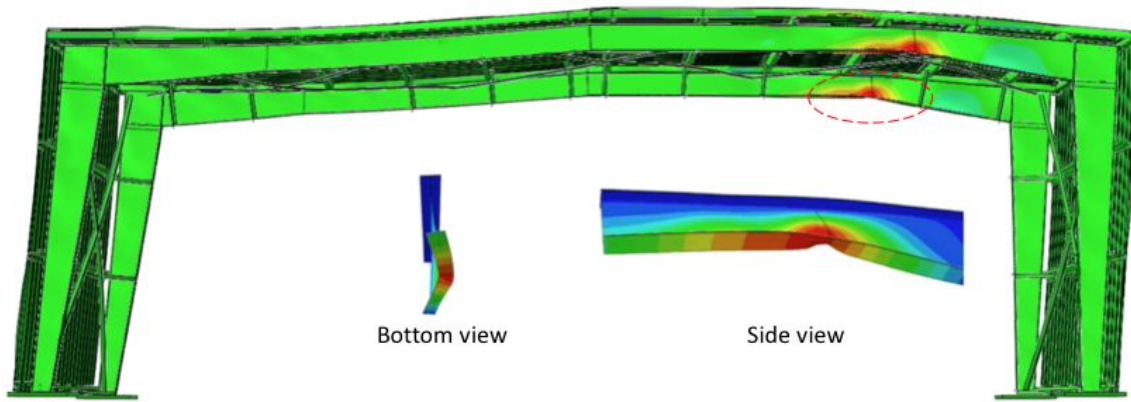


Figure 35. UCSD shake table specimen B1 lateral-torsional buckling at the northeast pinch point is observed in the test and predicted by simulation at IV250

UCSD Shake Table Specimen B2

The Specimen B2 frame in Figure 36 has a similar span to Specimen B1 with columns that support precast concrete walls. The walls rest in a channel member connected transversely across both frames and they are bolted to the primary frames at midheight and near the eave.

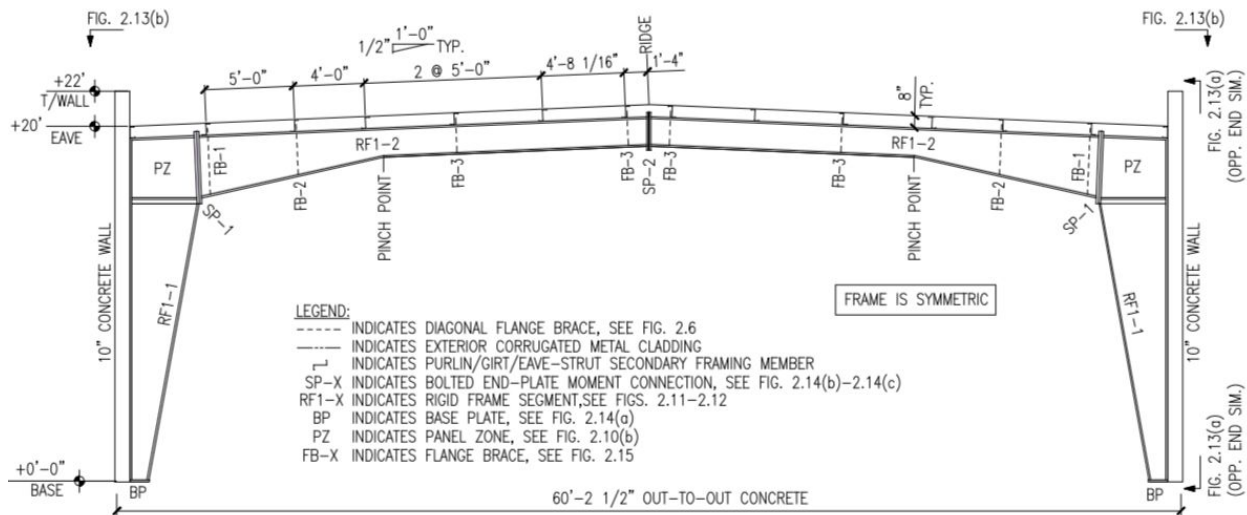


Figure 36. UCSD heavy wall shake table Specimen B2 with two parallel main frames connected with girts, purlins, roof panels, and precast concrete hard walls

The white noise test determined that first natural period of the building was 0.48 seconds. Lateral-torsional buckling developed at all four web pinch points in the IV100 test, with significant damage to the inner flange braces connected to the purlins at IV150. Fracture in an inner flange at a pinch point developed, consistent with Specimen B1. Lateral drift exceed 2% (5 in.) at IV150, and more energy dissipation is observed in the hysteretic loops compared to Specimen B1, as shown in Figure 37.

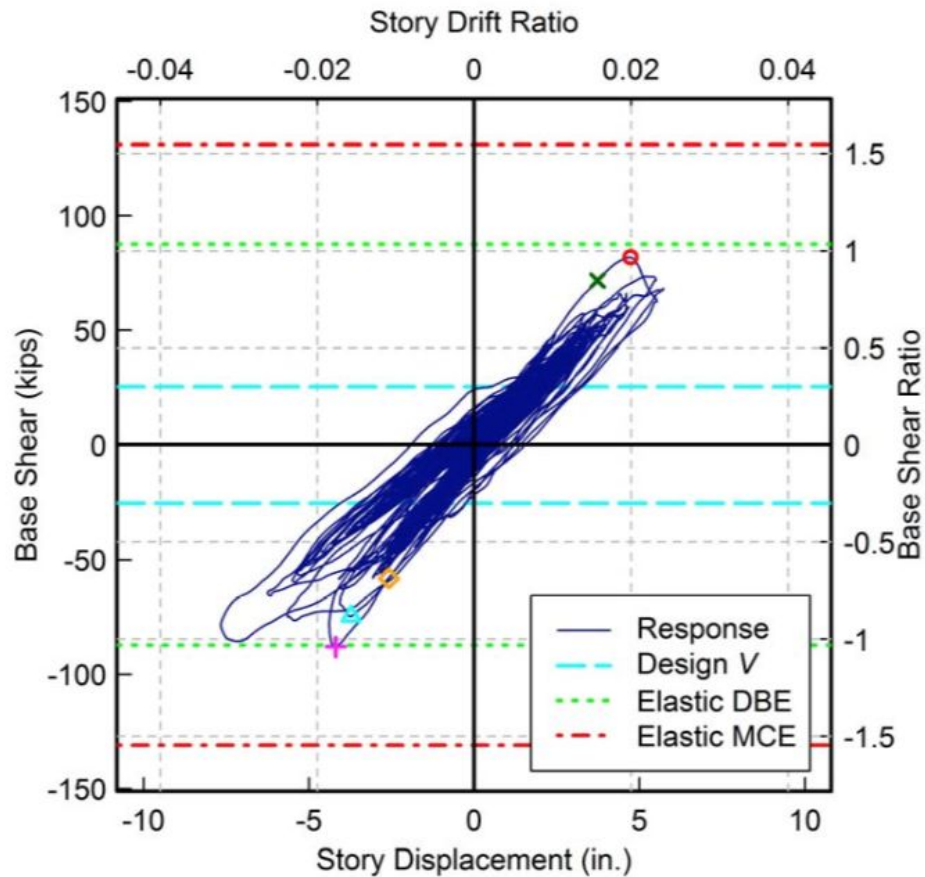


Figure 37. UCSD Specimen B2 heavy wall cyclic response with all loadings up to IV150 overlaid exhibits more inelasticity and stiffness degradation than Specimen B1 because of main frame lateral-torsional buckling deformation and associated damage caused by the precast concrete wall mass

Acceleration and displacement (drift) time history response test and simulated responses are similar for Specimen B2 at IV50 as shown in Figure 38. The natural period and maximum drift are consistent between test and simulation, as shown in Table 10, and buckling in the primary frame bottom flange is captured in the simulation at the same location as in the test, as shown in Figure 39.

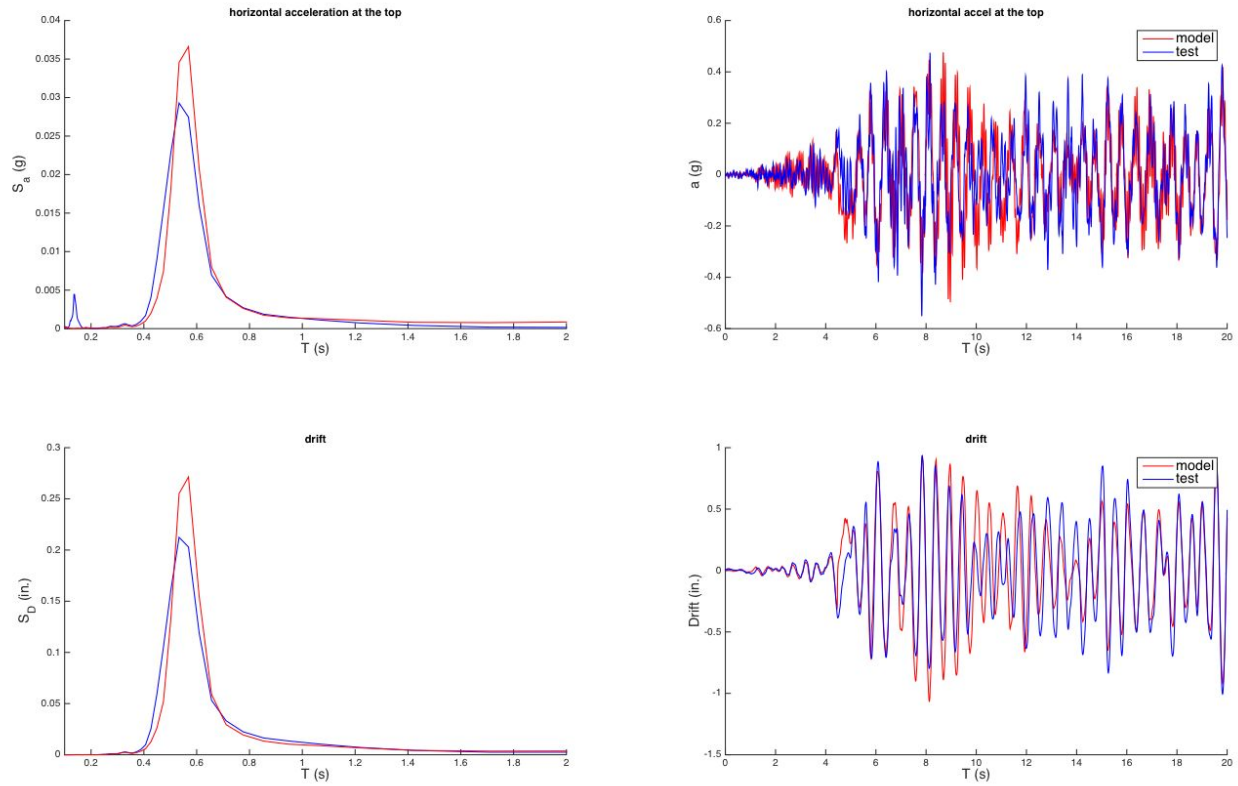


Figure 38. UCSD shake table specimen B2 tested and simulated acceleration and displacement (drift) spectral and time history response at IV50

Table 10. UCSD shake table specimen B2 tested and simulated natural period and maximum displacement (drift)

Building	Record	Period test (s)	Period model (s)	Period test/predicted	Max drift test (in)	Max drift model (in)	Max drift test/predicted
B2	IV50	0.55	0.53	1.04	1.50	1.57	0.96
	IV100	0.66	0.66	1.00	5.53	5.49	1.01

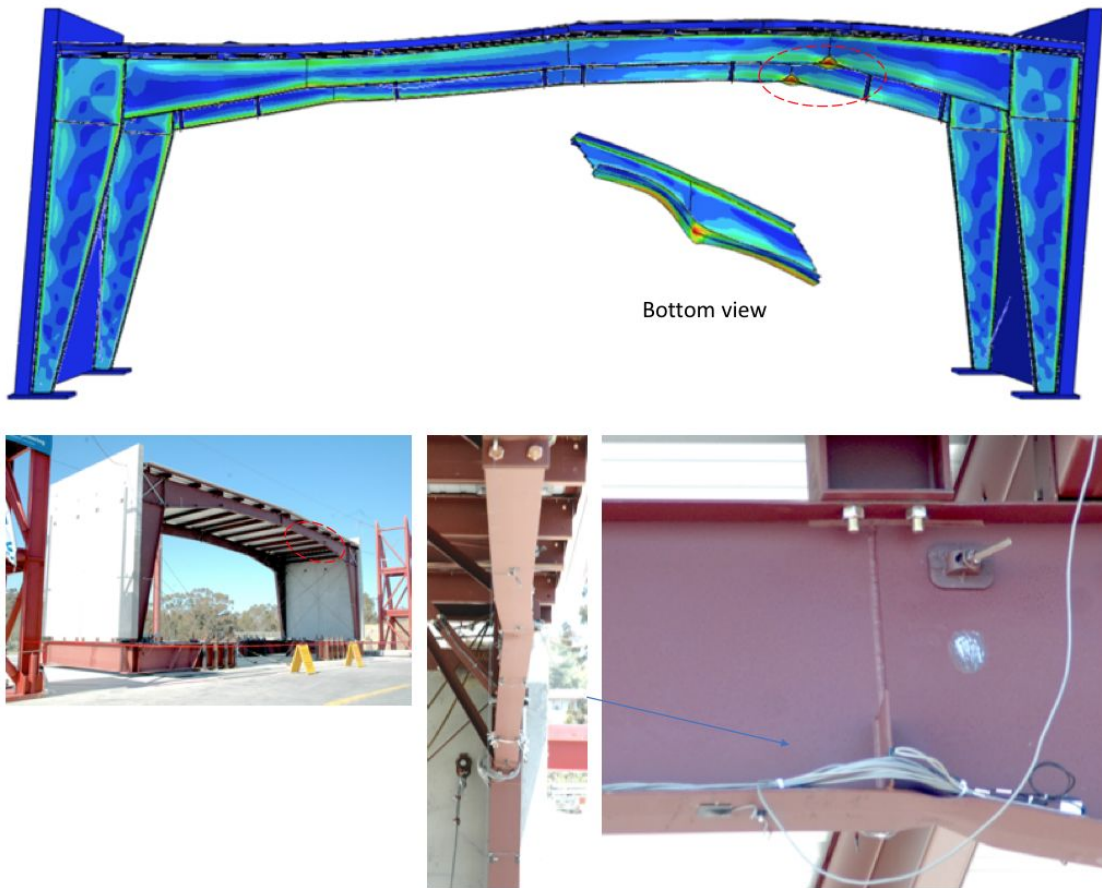


Figure 39. UCSD shake table Specimen B2 local and lateral-torsional buckling at northeast and southeast pinch points: simulation results versus test observations at IV150

UCSD Shake Table Specimen B3

UCSD Specimen B3 in Figure 40 has a similar span and height to Specimens B1 and B2, heavy walls, and a half height mezzanine bolted to one column side. The first natural period of the building is 0.52 seconds, again measured with white noise tests.

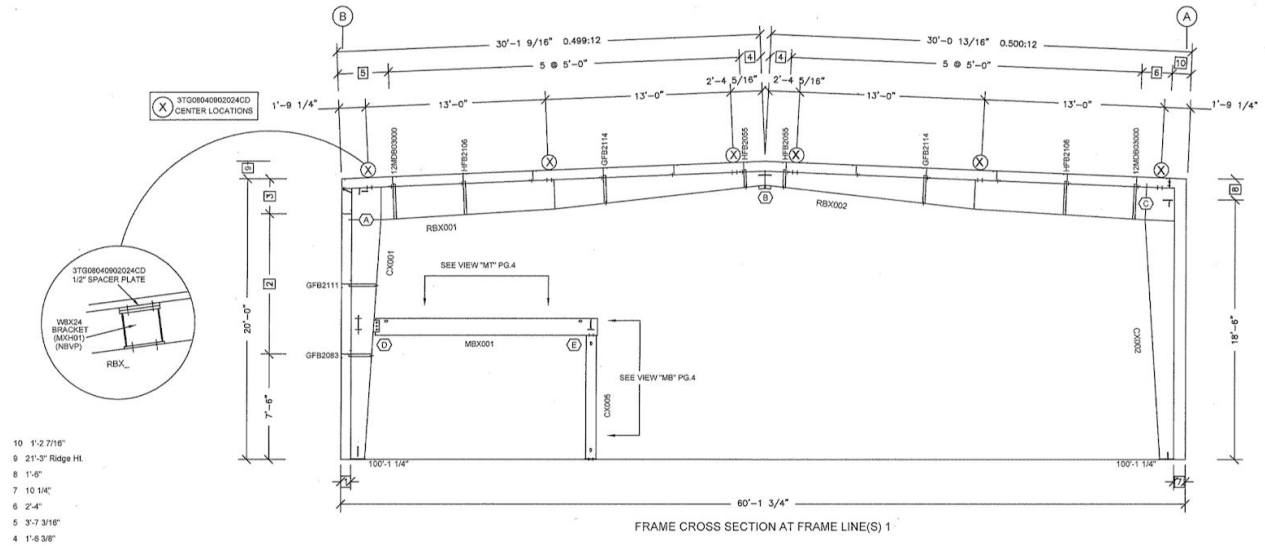


Figure 40. UCSD shake table Specimen B3 with a mezzanine bolted to one column at midheight

The hysteretic response in Figure 41 for Specimen B3 is asymmetric because of the mezzanine. Maximum drift of approximately 5% (10 in.) is highest when the inertia from the mezzanine mass (a horizontal concrete slab) pushes the column to the left, placing the column inner flange in compression, see the lower left hand quadrant. Panel zone buckling in the primary frame developed on the side where the mezzanine is connected at IV200, and repeated cycles in the buckling fold lines at IV250 resulted in panel zone fracture and significant stiffness degradation. This response is much different than the response of Specimens B1 and B2, with a different limit state (panel zone buckling) driving cyclic degradation.

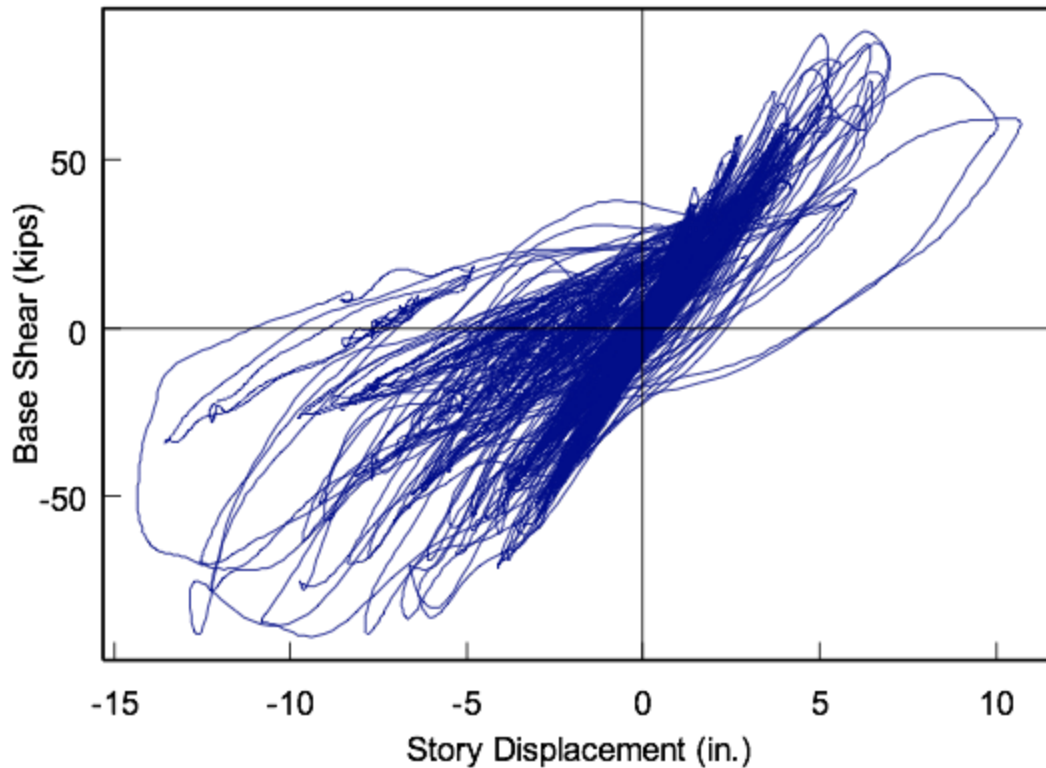


Figure 41. UCSD shake table Specimen B3 cyclic response with all loadings up to IV250 overlaid exhibits the most inelasticity and stiffness degradation out of the three specimens because most of the damage - buckling leading to fracture along the half-wave fold lines, concentrated in the main frame knee panel zones

The acceleration and displacement (drift) time history responses are again consistent when comparing test and simulation, this time at IV150 as shown in Figure 42. Test-to-predicted results in Table 11 highlight the viability of the simulation protocol even when a building with a mezzanine is considered. Panel zone deformations that result in the cyclic strength and stiffness degradation are captured in the simulation, as shown in Figure 43.

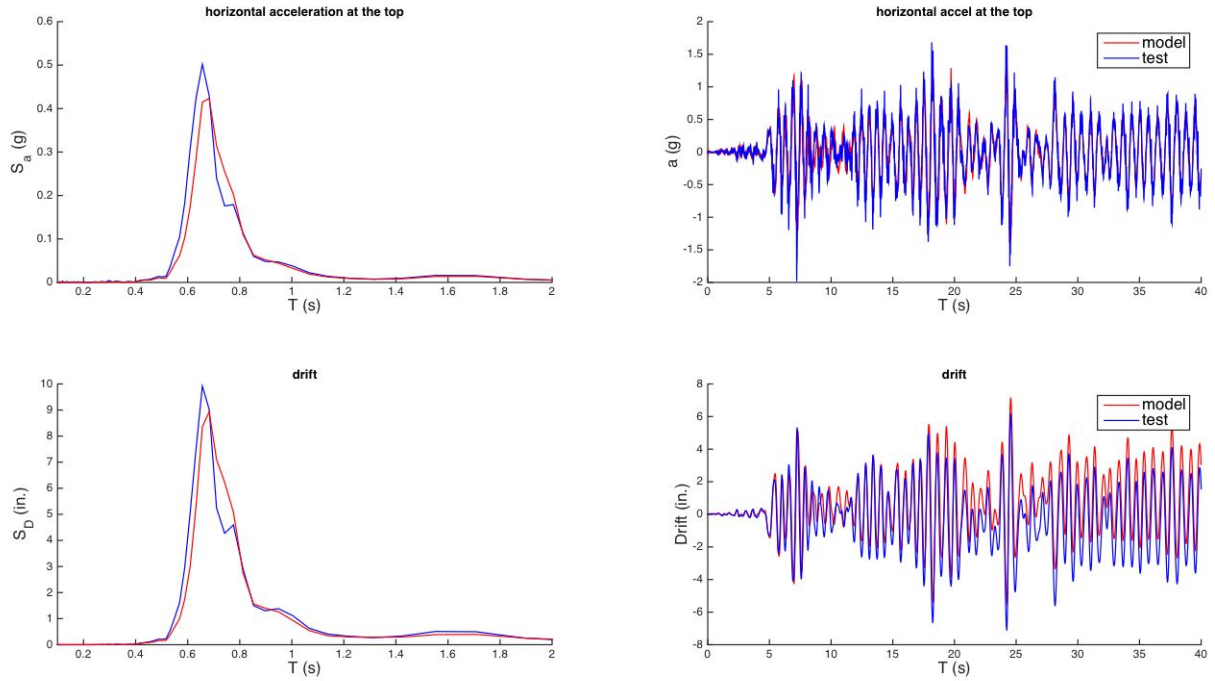


Figure 42. UCSD shake table specimen B3 tested and simulated acceleration and displacement (drift) spectral and time history response at IV150

Table 11. UCSD shake table specimen B3 tested and simulated natural period and maximum displacement (drift)

Building	Record	Period	Period model	Period	Max drift test	Max drift model	Max drift
		(s)	(s)	test/predicted	(in)	(in)	test/predicted
B3	IV50	0.52	0.55	0.95	1.62	1.47	1.10
	IV100	0.59	0.61	0.97	5.32	5.60	0.95
	IV150	0.66	0.68	0.97	7.10	7.13	1.00

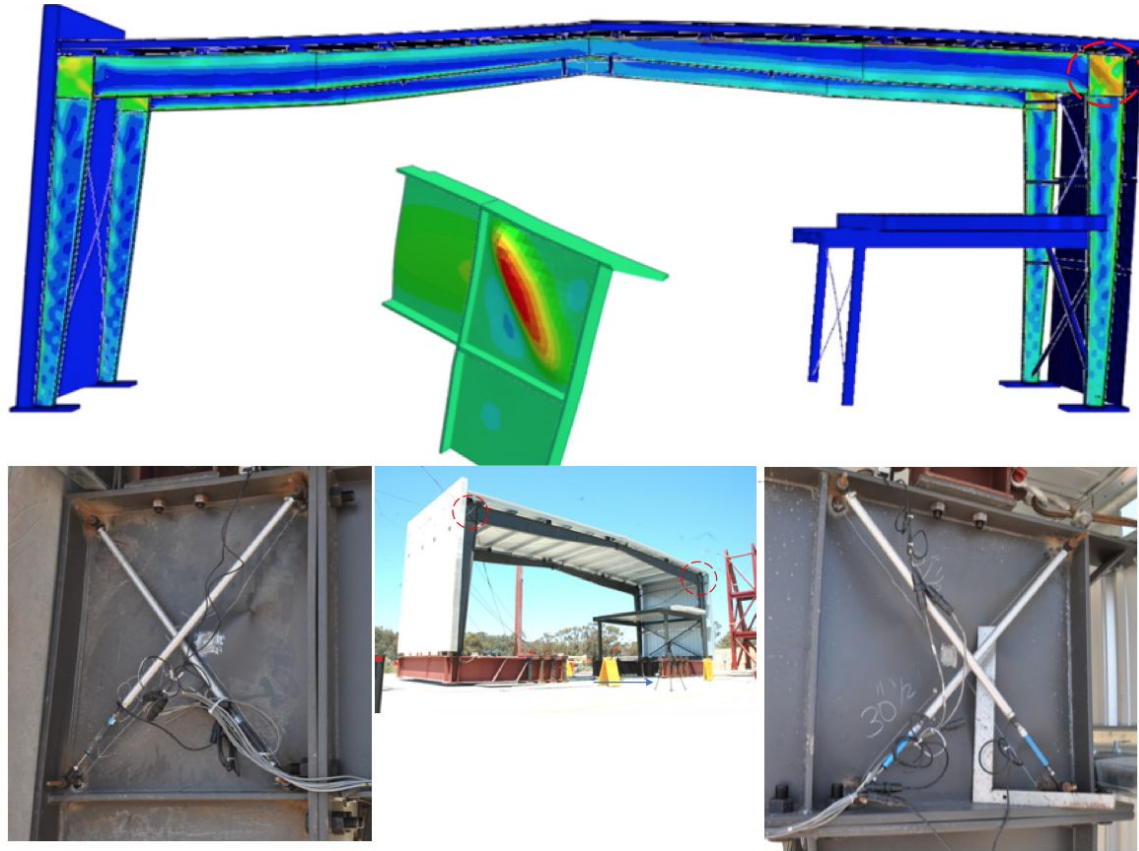


Figure 43. UCSD shake table Specimen B3 panel zone buckling: model results versus test observations at IV150

6.3. High fidelity simulation accuracy: maximum drift as a function of earthquake intensity

The UCSD shake table test matrix designs were successful in developing a variety of seismic limit states and the modeling protocol introduced in Chapter 5 is confirmed to predict these limit states. The maximum drift trends, as a function of earthquake intensity, are defined by these limit states as shown in Figure 44 and Table 12, which vary with each building specimen configuration. If lateral-torsional buckling is controlled as it was in the shake table Specimen B1 light wall configuration with flange braces, then a large drift capacity is available. The hard walls in shake table Specimen B2 add more mass, which caused lateral-torsional buckling to develop sooner, and the magnitude of the buckling deformation is higher which caused more performance degradation as the flange braces work harder and then fail. Specimen B3 drift trends in Figure 44 are similar to Specimen B2 because of the same lateral-torsional buckling deformation. The similar maximum drift trends also show that the mezzanine did not have a significant effect on seismic response below IV150. The performance difference for Specimen B3 is that at higher magnitudes (IV 300) the mezzanine restricted one column from swaying

laterally, which caused lateral deformation to concentrate at the frame knee causing panel zone buckling, cracking, and failure with high stiffness degradation compared to Specimens B1 and B2. The Specimen B3 primary frame also had seismically compact flanges which minimized the influence of local buckling deformation (i.e., a locally softening cross-section) that can initiate lateral-torsional buckling. A discussion of metal building limit states and the ability of high fidelity simulation to predict their initiation of system collapse is put forth in the next Chapter.

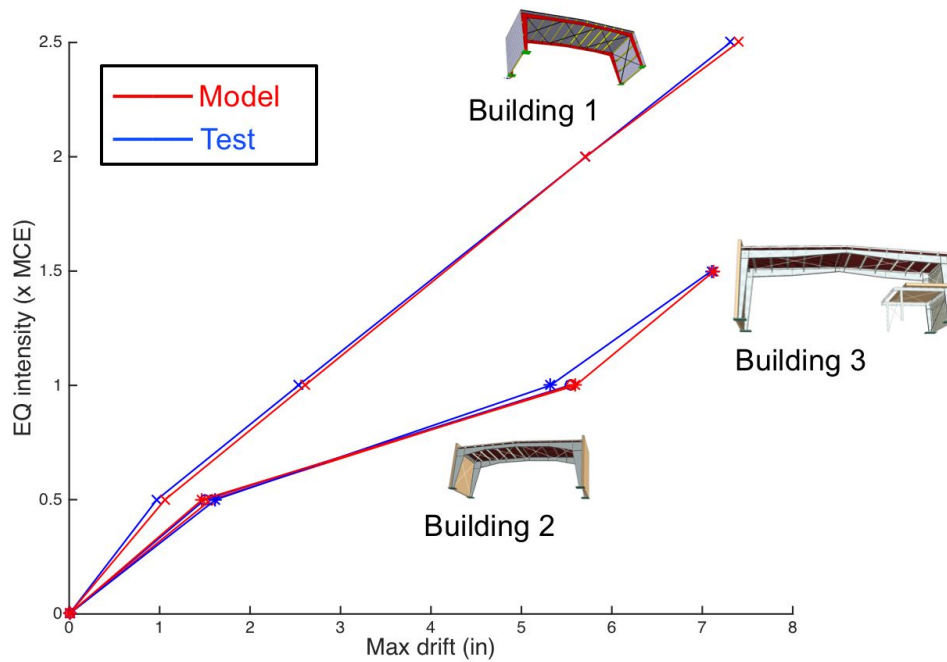


Figure 44. Earthquake intensity and maximum drift of the high fidelity models versus test results for UCSD shake table specimens

Table 12. Maximum drifts and failure modes observed in the UCSD shake table tests

Building	Record	Max Shake-table test drift	Collapse on Shake-table	Observed failure mode on shake-table
B1	IV300%	3.50%	No	LTB
B2	IV150%	3.60%	No	LTB, FLB
B3	IV250%	5.40%	No	Panel Zone Buckling/Yielding

7. Observing and Modeling Metal Building Seismic Limit States

7.1. Metal building seismic limit states captured by the high fidelity modeling protocol

The key limit states identified in the UCSD experimental programs are main frame local-global buckling interaction and panel zone yielding, both of which are known as primary contributors of cyclic stiffness and strength degradation that cannot be easily modeled in typical frame analyses.

The impact of lateral-torsional buckling on the cyclic response in the UCSD shake table tests was not significant until either the flange braces failed or fracture at the pinch point evolved enough such that the frame load path was compromised, and this performance degradation is captured with the geometric and material nonlinearities included in the high fidelity modeling protocol.

Flange local buckling in well-braced primary frame regions did not cause significant system distress in the UCSD subassembly frame tests (Specimen CS3 results in Figure 25). It is still important to consider because when local buckling initiates in unbraced primary frame regions, it can drive global buckling deformation as cross-section stiffness degrades. All of this is included in the modeling strategy presented herein.

Panel zone yielding in UCSD shake table Specimen B3 (with the mezzanine) was observed to be an key source of energy dissipation at high seismic magnitudes (Figure 41). Shear deformation demands resulted in shear buckling and tension field action (yielding along the buckled fold lines), even with stiffeners in place. The panel zone is discretized with shell elements in the high fidelity simulations, and all of this behavior is explicitly captured.

7.2. Metal building seismic limit states excluded in the high fidelity modeling protocol

Low cycle fatigue and associated fracture like that observed in the UCSD shake table tests at high earthquake amplitudes is not considered in the high fidelity seismic simulations, primarily because computationally efficient treatments for this phenomenon are not readily available and validated for steel structures. Element deletion and crack propagation would have required

significant time to explore, implement, and run, especially for the quantity of FEMA P695 time history analyses needed to define collapse margin ratios. Instead, the study summarized in the next section was performed to relate equivalent plastic strains calculated in the high fidelity simulations to fracture initiation and limits.

7.3. Plastic strain demands from high fidelity seismic simulation

Plastic strains are easily tracked in high fidelity simulations and they can be used as an indicator of fracture. The challenge is defining reasonable limits on the strain magnitude, and the region over which this strain can occur, that corresponds to fracture.

Equivalent plastic strain (PEEQ) is the scalar magnitude of the plastic strain vector which is the strain in each element direction beyond the steel yield strain. It can be used as a predictor of fracture by using a uniaxial tension coupon test results which provides the amount of plastic strain available before the coupon fractures, and typically 10% is used as a conservative limit.

The UCSD building specimen peak PEEQ magnitudes taken from the nonlinear dynamic simulations vary as a function of Imperial Valley earthquake intensity and the building type as shown in Figure 45. Specimen B1 (light wall) and B2 (heavy wall) experience the highest plastic strains at the main frame welded flange transitions accompanying lateral-torsional buckling, and Building 3 (with the mezzanine) experienced the highest plastic strains at the frame knee panel zone.

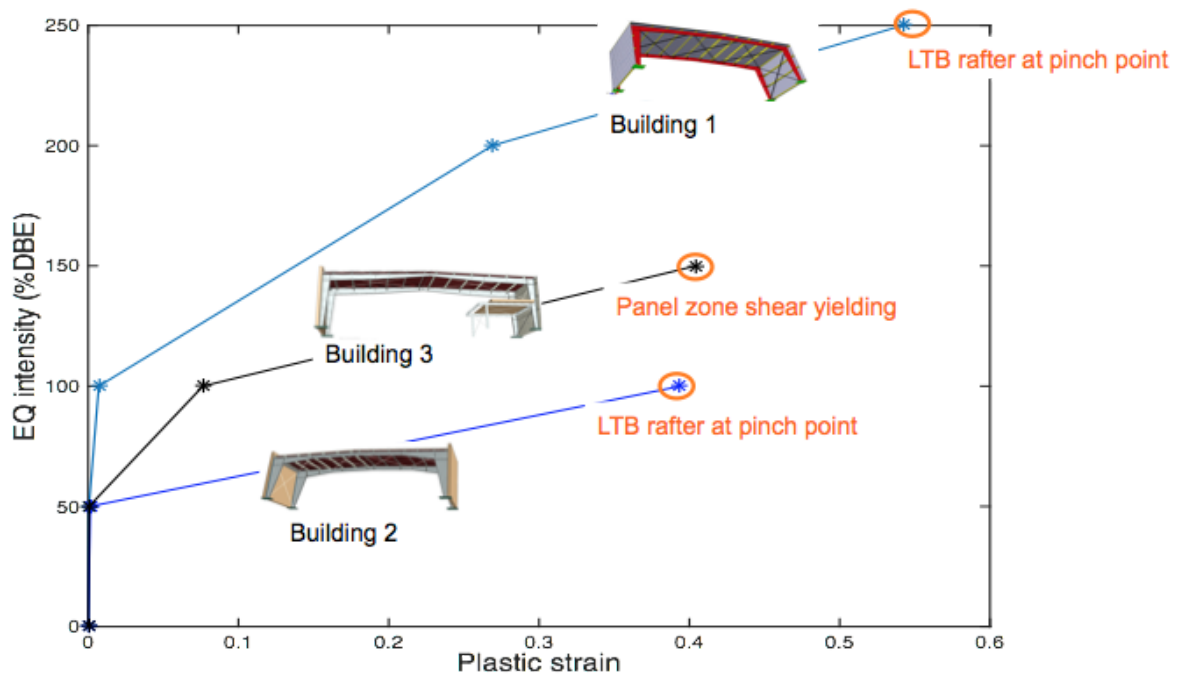


Figure 45. Maximum equivalent plastic strain magnitudes (PEEQ) calculated in high fidelity nonlinear time history simulations and the limit state associated with these strains

The maximum PEEQ magnitudes per element are plotted in Figure 46 as a function of the stress triaxiality or hydrostatic stress to the von Mises stress in the Imperial Valley cyclic time history analyses. The lighter Specimen B1 has PEEQ magnitudes mostly less than 0.10 at IV250, while Building 2 experiences PEEQ as high as 0.40 at IV100. Note, “IV” stands for Imperial Valley record and the subsequent percentage is showing the record magnification with respect to the MCE. Plastic strains in the secondary members (girts and purlins) are negligible.

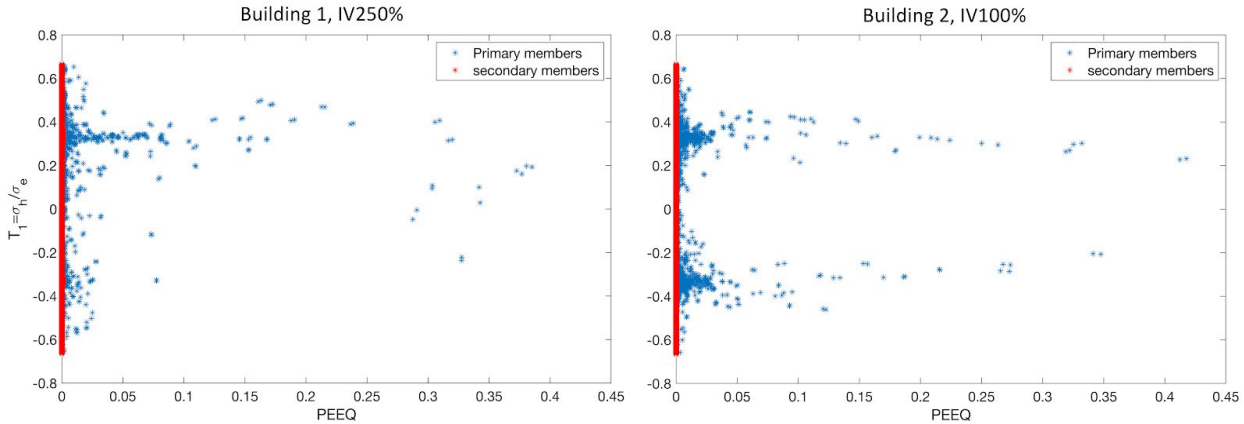


Figure 46. Maximum equivalent plastic strain magnitudes (PEEQ) in each finite element for UCSD Specimen B1 (IV250) and Specimen B2 (IV100) from nonlinear time history simulations.
 Note: T_1 is stress triaxiality

When the earthquake magnitude is increased in Specimen B2 to IV150 (see Figure 47), peak PEEQ reaches as high as 1.0 at main frame locations where lateral-torsional buckling initiates, and exceeds 1.6 for IV200 (Figure 47 again). It is clear that at these strains that fracture will occur, and this was observed in the shake table tests.

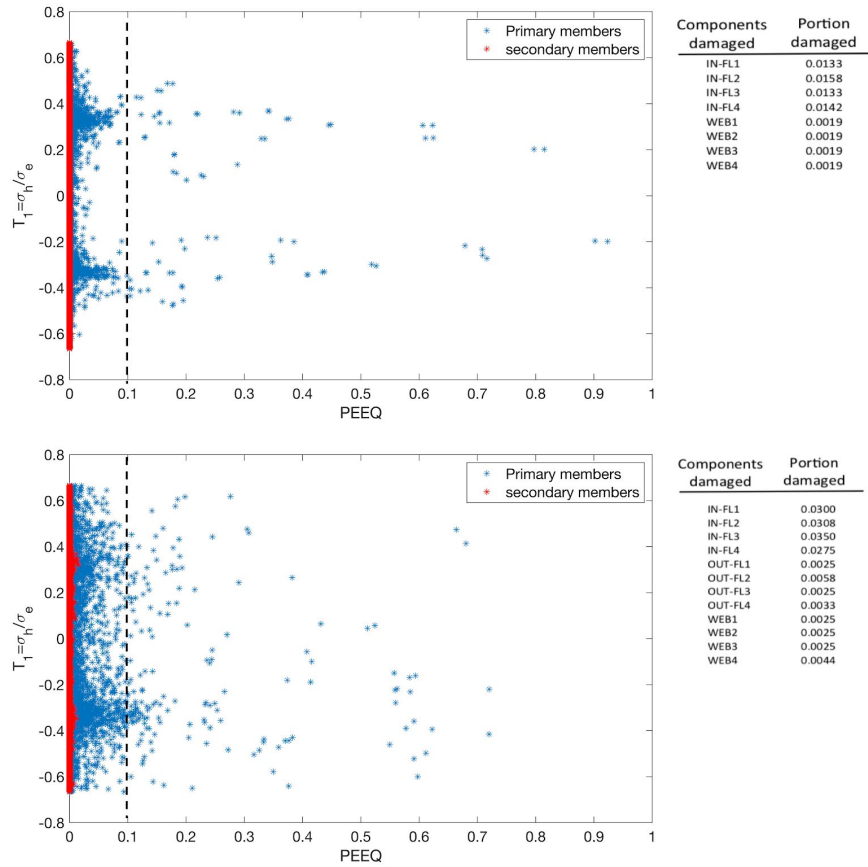


Figure 47. Maximum equivalent plastic strain magnitudes (PEEQ) in each finite element for UCSD Specimen B2 subjected to IV150 (first plot) and IV200 (second plot) from nonlinear time history simulations along with tabulated damaged area percentages per main frame region

The PEEQ is plotted element by element in Figures 46 and 47, however the size of the region over which these strains occur is also important to consider when establishing fracture limits. UCSD Specimen B2 is split up into regions in Figure 48, and the portion of that building segment that exceeds 10% PEEQ is provided for IV150 and IV200. The damaged portion of the primary frame segment ranges from about 1% to 3%.

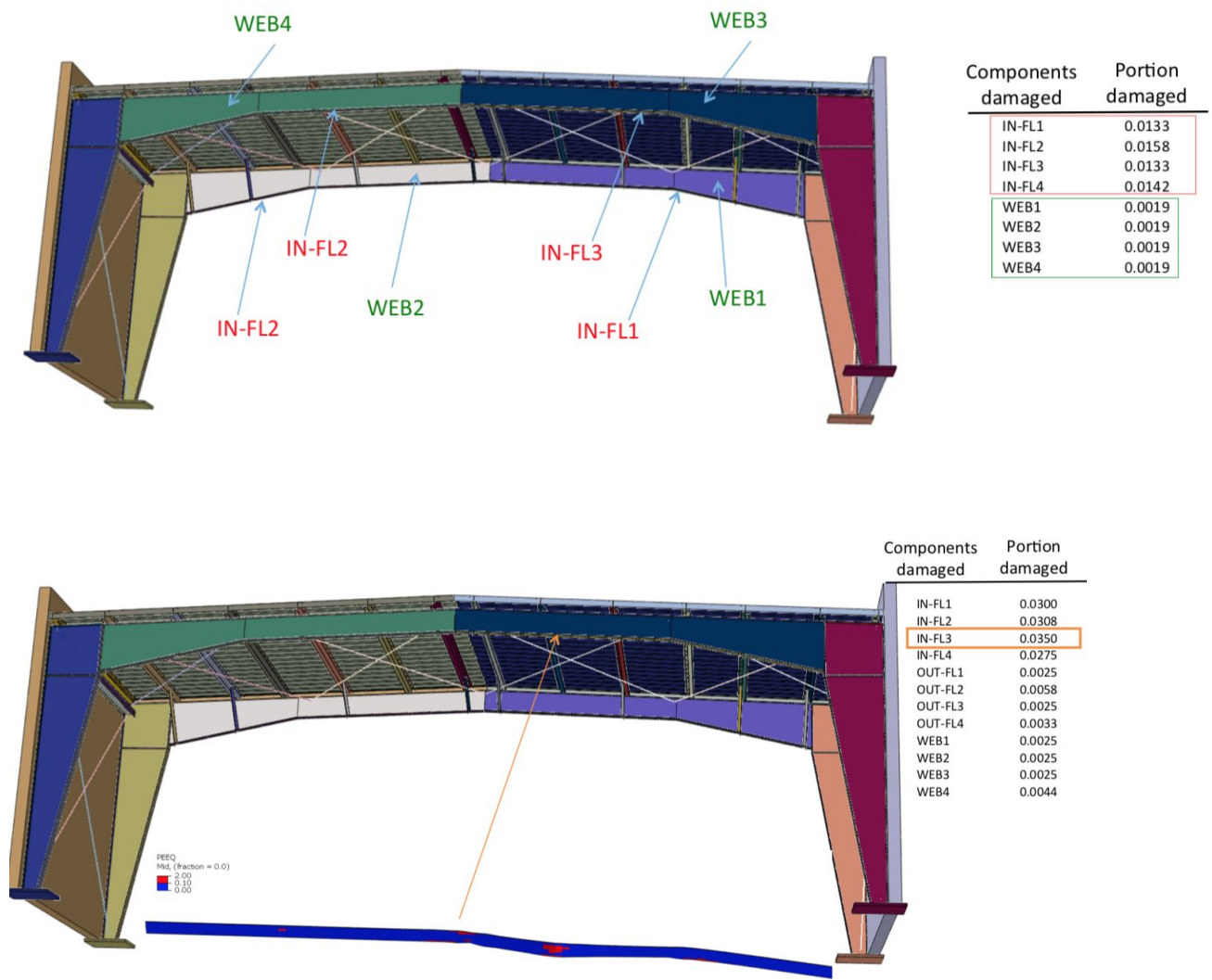
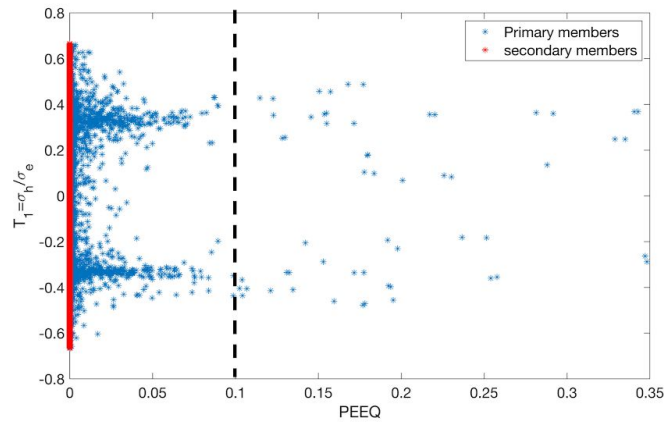


Figure 48. Portion of equivalent plastic strain (PEEQ) exceeding 10% in UCSD Specimen B2 main frame components at IV150 and IV200

7.4. A drift-based fracture limit for defining metal building system collapse

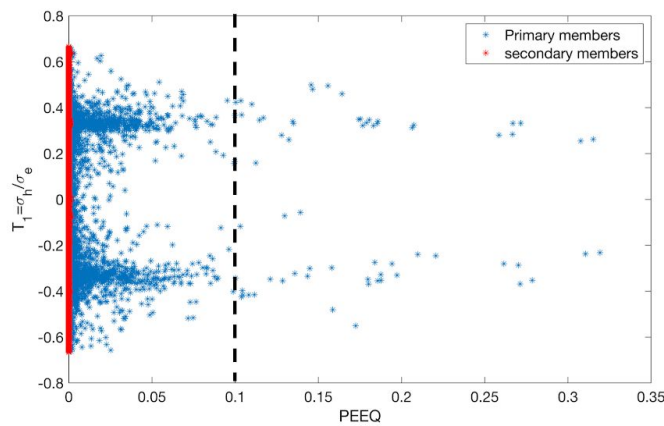
Another way to interpret the PEEQ magnitudes is to study them at a drift limit of 4%, as shown in Figure 49. Here the damage portion of the inside flanges (IN-FL1 for example) is around 1%. By setting the damage portion limit to 2% established along with the 10% PEEQ limit, a conservative fracture criteria that can be used as a building system collapse limit in the context of FEMA P695 are defined. Tying this criteria to a drift limit, i.e., that system-debilitating fracture may occur between 4% and 5%, allows for the identification of fracture-prone archetypes in studies on seismic simulation to collapse that begin in the next chapter.

Plastic strains from time history analysis, IV150%, max drift ~ 4%



Components damaged	Portion damaged
IN-FL1	0.0133
IN-FL2	0.0158
IN-FL3	0.0133
IN-FL4	0.0142
WEB1	0.0019
WEB2	0.0019
WEB3	0.0019
WEB4	0.0019

Plastic strains from cyclic analysis max drift = 4%



Components damaged	Portion damaged
IN-FL1	0.0100
IN-FL2	0.0117
IN-FL3	0.0108
IN-FL4	0.0092
OUT-FL3	0.0008
OUT-FL4	0.0008
WEB1	0.0019
WEB2	0.0019
WEB3	0.0019
WEB4	0.0019

Figure 49. Portion of equivalent plastic strain (PEEQ) exceeding 10% in UCSD Specimen B2 main frame components at a drift limit of 4%

8. A Computationally Efficient Nonlinear Metal Building Seismic Time History Modeling Protocol

8.1. Using high fidelity simulation to inform computational efficient seismic modeling

It was confirmed in the previous chapters that high fidelity simulation can consistently and accurately predict the structural response of metal buildings to earthquake ground motions. This validated capability is powerful because it allows us to examine, comprehend, and generalize behavior in a fraction of the time and expense of a shake table experiment. For example, a simulated pushover test can be performed in a few hours of CPU time to obtain system overstrength for a specific metal building archetype, and many different archetypes can be ‘constructed’ and ‘tested’ without making a single weld. High fidelity incremental dynamic analysis (IDA) is also available, however the computational cost is significant, and for this project, it was deemed to be too expensive for a probabilistic characterization framework like FEMA P695. A practical modeling approach is described in the following sections, where the high fidelity simulations are used to characterize metal building hysteretic response, and this response is used in a nonlinear SDOF model that includes metal building seismic limit states.

8.2. Nonlinear SDOF metal building response to seismic ground motions

Metal building earthquake response is represented in a classical SDOF dynamic model by lumping mass, M , and stiffness, K_t , and damping, C , as shown in Figure 50 such that the dynamic properties, specifically the natural period of vibration, T , are consistent with what would be expected if measured in a real building. Strength and stiffness degradation and the period shift as the building experiences damage during an earthquake is approximated by making K_t nonlinear, i.e., fitting the cyclic hysteretic response to a material model.

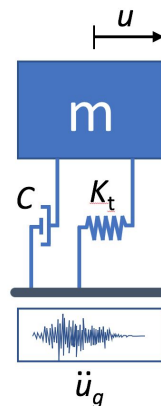


Figure 50. Metal building nonlinear SDOF model definitions

8.3. Metal building SDOF seismic simulation parameter: stiffness, K_t

A viable SDOF approximation of a metal building starts with the characterization of the relationship between the displacement (u in Figure 50) and the external force in the SDOF model. In the SDOF modeling approach the developed force in the spring, along with the other dynamic forces such as the inertial force and the damping force, are in equilibrium with the support reaction force. This reaction force is the “base shear” and the displacement of the mass with respect to the base is defined as “story drift”. The stiffness K_t provides the relationship between base shear and the story drift when all other dynamic force components (i.e., inertial and damping forces) are zero.

The high fidelity cyclic simulation capability for a metal building comes in handy here, because it can be used to define K_t . In this study a quasi-static cyclic displacement loading history is produced with the high fidelity simulation protocol described in Chapter 5 considering the roof height (top of the panel zone region) as the SDOF. With this high fidelity to SDOF mapping, the SDOF cyclic response includes local and system level responses including rafter lateral-torsional buckling and local buckling, the nonlinear baseplate response, and bracing from the secondary structural system (purlins, girts, braces, X-bracing, and panels).

The quasi-static cyclic response of UCSD shake table Specimen B1(light wall) and Specimen B2 (heavy wall) from high fidelity simulation are presented in Figure 51 and Figure 52. These high fidelity results are matched to a Pinching 04 material model in OpenSees (McKenna et al. 2004) where the minimum of the building response in the first and third quadrants are used as backbone targets. Cumulative energy dissipation, also plotted in Figure 51 and Figure 52, confirm that the Pinching 04 model is consistent with the simulated cyclic response.

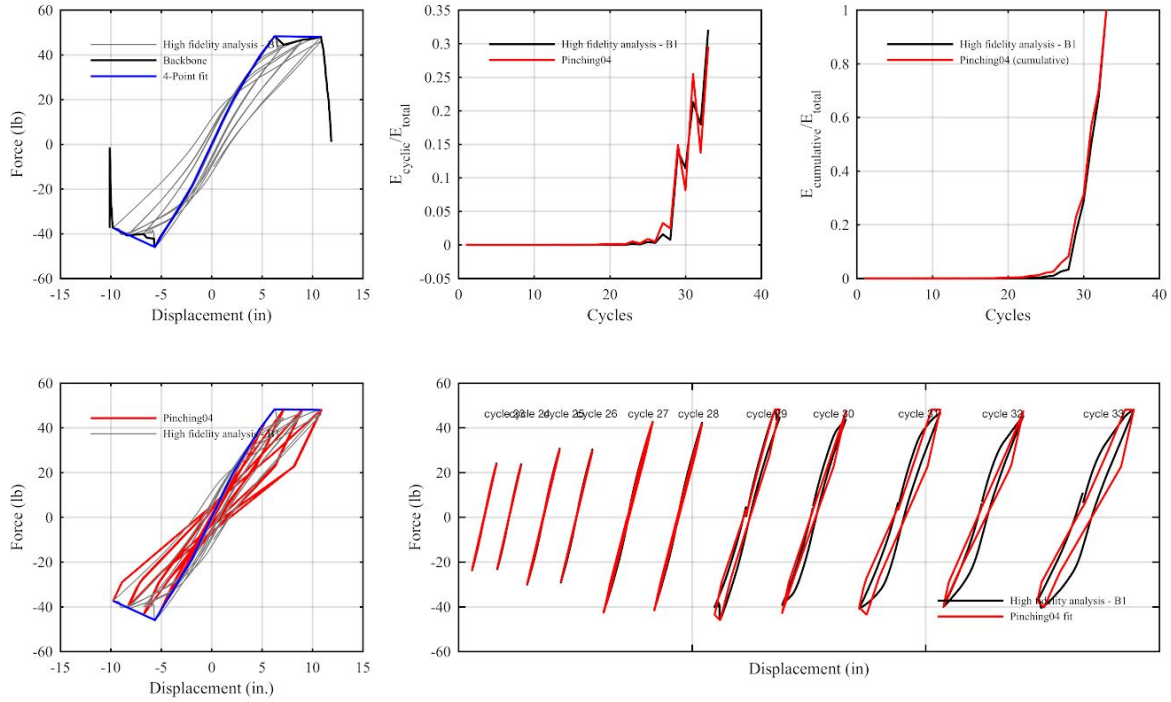


Figure 51. Quasi-static cyclic response of UCSD Specimen B1 - high fidelity simulation and fitted response using Pinching 04 hysteretic model in OpenSees

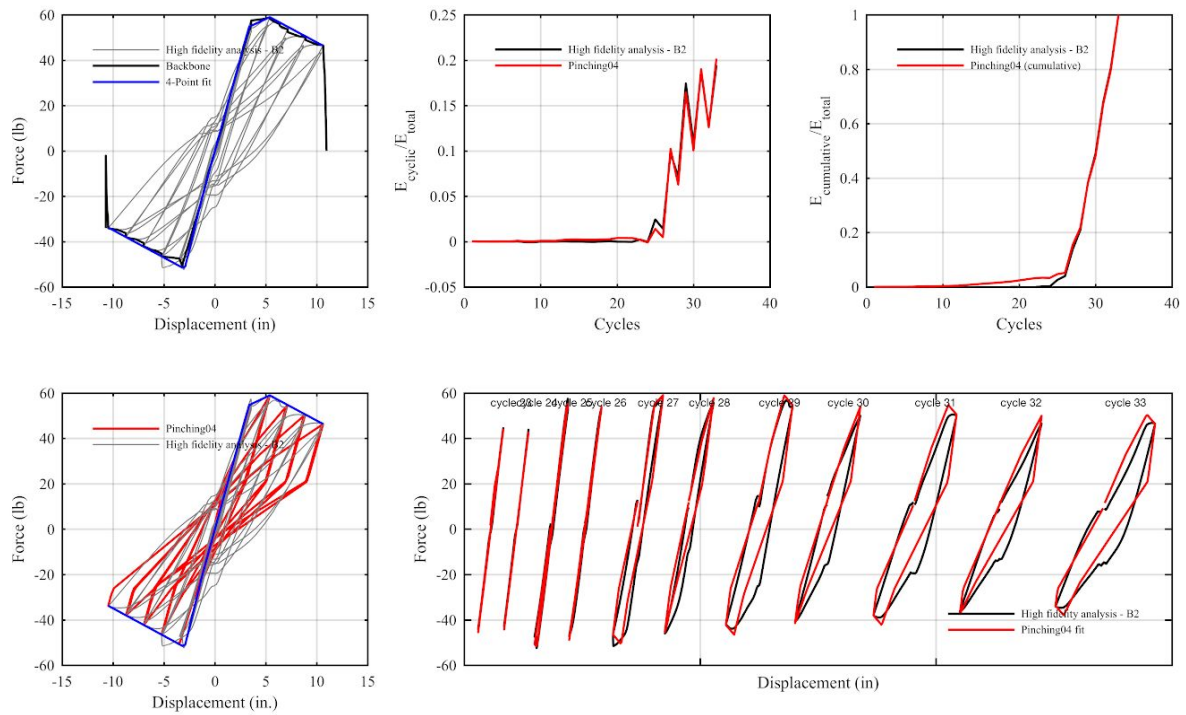




Figure 52. Quasi-static cyclic response of UCSD Specimen B2 - high fidelity simulation and fitted response using Pinching 04 hysteretic model in OpenSees

8.4. Metal building SDOF seismic simulation parameter: period, T

The cyclic load-deformation response provides the initial structural stiffness that defines the fundamental building period, T . It is important that the SDOF model used for incremental dynamic analysis later in this report has a T that is consistent with test results and in this case, the high fidelity metal building model response.

The fundamental vibration mode and associated periods of vibration (T) of UCSD shake table Specimens B1 and B2 are compared for both tested and high fidelity simulation in Table 13. High fidelity simulation is used to calculate T in two ways, an elastic modal eigenvalue solution and with white noise excitation, and these are consistent with the tested T from white noise tests conducted at UCSD.

Table 13. Modal response of UCSD shake table Specimens B1 and B2 high fidelity simulation characterized with an eigenvalue solution and with a white noise simulation

	Specimen B1	Specimen B2
First mode deformation		
Period (modal-initial)	0.40 sec.	0.50 sec.
Period (white noise-sim.)	0.39 sec.	0.52 sec.
Mass participation in first mode	77%	73%

8.5. Metal building SDOF seismic simulation parameter: mass, m

Defining the relevant mass in the SDOF model is challenging because the metal building mass is not all concentrated at the roof level. For example, in UCSD shake table Specimen B2, a large portion of the seismic mass is attributed to the vertical concrete walls on either side of the

building. In this study the seismic mass, m , for a metal building is always assumed equal to the mass used to calculate the design seismic weight in an equivalent lateral force procedure.

8.6. Metal building SDOF seismic simulation parameter: equivalent initial stiffness, k_{eq}

It is desirable to match the fundamental building period to the SDOF model so that elastic behavior is consistent. The relationship between the mass, initial stiffness, and the period of the building can be written as follow:

$$T_1 = 2\pi\sqrt{m/k_i}$$

where m is the seismic mass, k_i is the initial stiffness of the building in the SDOF model, and T_1 is the fundamental period of the SDOF model. Since the period of the building is determined by both high fidelity analysis and shake-table testing, and seismic mass of the building is also defined in the seismic design of the building, an equivalent initial stiffness is required to match the actual building period to the SDOF model.

FEMA P695 (Chapter 6) addresses this challenge by defining an effective yield roof drift displacement, $\delta_{y, eff}$, as follow:

$$\delta_{y, eff} = C_o [V_{max}/W] [g/4\pi^2] (\max(T, T_1))^2$$

where T is the fundamental period ($C_u T_a$) per ASCE 7, T_1 is the fundamental period of the building models computed using eigenvalue analysis, W is the seismic weight of the building, g is the acceleration of gravity, and V_{max} is the maximum base shear of the building. For a single story structure like a metal building, the modal coefficient C_o is 1.0, and by assuming that the actual period of the building is larger than the ASCE 7 prediction ($T_1 > T$), the above equation can be simplified to:

$$V_{max}/\delta_{y, eff} = 4\pi^2 m/T_1^2$$

By assuming $k_{eq} = V_{max}/\delta_{y, eff}$, the equivalent initial stiffness for the SDOF model, k_{eq} , can be calculated as:

$$k_{eq} = 4\pi^2 m/T_1^2$$

This equivalent initial stiffness is used in the Pinching 04 models.

8.7. Metal building SDOF seismic simulation parameter: damping ratio, ξ

The last term to consider in the SDOF dynamic equation is energy dissipation treated with the viscous damping ratio, ξ . The viscous damping ratio is typically determined by experiment and is reported for the UCSD shake table tests (Smith 2013). The shake table tests showed that the damping ratio increased with earthquake magnitude and when buckling limit states initiated. For all simulations in this study, $\xi=2\%$ is selected corresponding to a low intensity elastic response assuming that energy dissipation from yielding, buckling, and damage are accounted for in the hysteretic response.

8.8. Validation of metal building nonlinear SDOF seismic modeling protocol

The mass, stiffness, and damping parameters employed in the SDOF simulations are summarized in Table 14. The SDOF models receive as input the acceleration time history recorded at the base of each building specimen on the shake table.

Table 14. SDOF mass and stiffness parameters for UCSD Specimens B1 and B2

Specimen	Design Base Shear V_b	Design Seismic Weight W_e	Seismic mass m	equivalent initial stiffness k_{eq}
	kip	kip	kip.sec ² /in	kip/in
B1	6.52	18.96	0.04912	12.75
B2	25.4	74.00	0.1918	28.00

The viability of the SDOF models as a computationally efficient surrogate for high fidelity IDA is confirmed with comparisons to the UCSD shake table test results in Figure 53 and Figure 54. In the elastic range of behavior (i.e., at IV50), the SDOF models for Specimen B1 and B2 follow the linear trend in maximum drift with earthquake intensity and this accuracy continues for the Specimen B1 SDOF model into higher intensities as shown in Figure 53.

The SDOF approximation of Specimen B2 (heavy wall) building in Figure 54 is less consistent with the tests at higher intensities because the building with heavy facade walls has more mass distributed away from the roof height. The building system collapse threshold, hinted at by the flattening of the SDOF intensity-drift curve, is conservatively predicted however with the SDOF model when compared to the tested and high fidelity simulation trends (which are not flattening). This observation is valuable when applying and interpreting the SDOF results within the FEMA P695 guidelines.

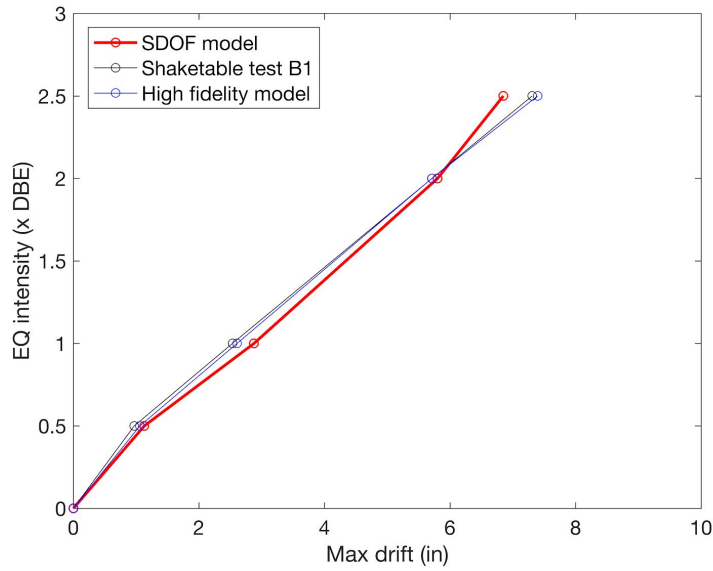


Figure 53. UCSD shake table specimen B1 earthquake intensity (as a multiplier of Design Basis Earthquake DBE) versus maximum drift at the metal building knee level as tested, with high fidelity simulation and with the SDOF model

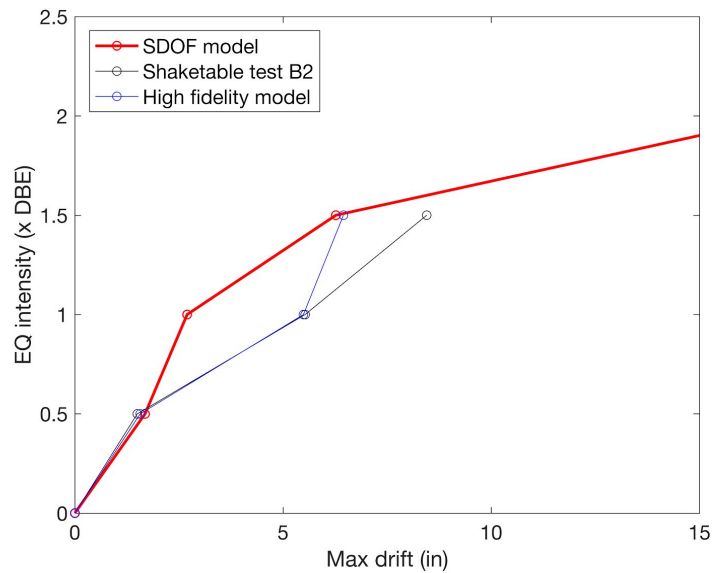


Figure 54. UCSD shake table specimen B2 earthquake intensity (as a multiplier of Design Basis Earthquake DBE) versus maximum drift at the metal building knee level as tested, with high fidelity simulation and with the SDOF model

8.9. Employing high fidelity and nonlinear dynamic SDOF metal building models in archetype seismic studies

The long story of seismic testing, modeling protocol development, and simulation validation for metal buildings is now complete. It is now time to apply the verified capabilities within a probabilistic seismic evaluation framework. The next chapter utilizes both high fidelity and SDOF models to calculate the collapse margin ratios defined by FEMA P695 for the metal building archetypes considered in the UCSD shake table tests. The same seismic performance quantification is then performed for the performance group of 4 index archetypes from Chapter 4, leading to general observations and recommendations for advancing metal building seismic design concluding the report.

9. Probabilistic Seismic Evaluation of UCSD Metal Building Shake Table Specimens

9.1. Using FEMA P695 to conduct seismic hazard characterization of metal buildings

It is challenging to succinctly describe the seismic performance of a structural system. The FEMA P695 guidelines approaches this challenge by defining four parameters from which to draw performance conclusions on index archetypes and performance groups - system overstrength (Ω), period-based ductility (μ_T), median collapse capacity (\widehat{S}_{CT}), and collapse margin ratio (CMR). The performance groups are typically organized to consider: (1) basic structural configuration; (2) gravity load level; (3) seismic design category; and (4) period domain. All of these are calculated for the UCSD metal building shake table Specimens B1 and B2 in this chapter.

Figure 55 summarizes the idealized nonlinear static pushover curve that defines system overstrength (Ω) and period-based ductility (μ_T). The system overstrength is the ratio of the maximum base shear, V_{max} , to the design base shear, V_b , which is the lateral demand at the Design Basis Earthquake (DBE). The period-based ductility, μ_T , is the ratio of the ultimate roof drift displacement, δ_u , defined as the roof displacement at $0.8V_{max}$, to the effective yield roof drift displacement $\delta_{y,eff}$ defined in Figure 55.

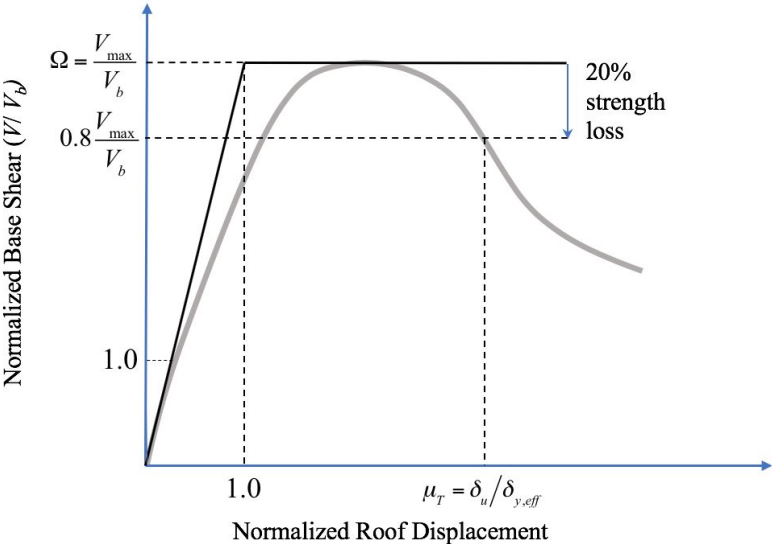


Figure 55. Idealized static pushover curve definitions for quantifying seismic response

The median collapse capacity, \hat{S}_{CT} , is the spectral acceleration when 50% of the applied ground motions collapse the structure. The collapse margin ratio (*CMR*) is defined as $CMR = \hat{S}_{CT} / S_{MT}$ where S_{MT} is the spectral acceleration corresponding to the Maximum Considered Earthquake (MCE). The *CMR* is the ratio of the seismic demand with respect to the MCE demand that causes collapse in half of the ground motion records. It is adjusted to $ACMR = SSF \times CMR$ with the spectral shape factor, *SSF*. The *SSF* is a function of the building fundamental period, T , and period based ductility, μ_T .

An acceptable *ACMR* defined by FEMA P695 is a 10% probability of average system collapse for a performance group of index archetypes. Another acceptable *ACMR* is defined as the 20% probability of collapse for the outlier index archetype within a performance group. The acceptable *ACMR* is calculated by assuming the distribution of collapse level spectral intensities is lognormal, with a median equal to \hat{S}_{CT} , and standard deviation of β_{TOT} . The total system uncertainty, β_{TOT} , is calculated as:

$$\beta_{TOT} = \sqrt{\beta_{RTR}^2 + \beta_{DR}^2 + \beta_{TD}^2 + \beta_{MDL}^2}$$

where β_{RTR} is the record-to-record collapse uncertainty defined as:

$$\beta_{RTR} = 0.1 + 0.1\mu_T \leq 0.4$$

The design uncertainty β_{DR} , test data-related collapse uncertainty β_{TD} , and the modeling-related collapse uncertainty β_{MDL} all typically range between 0.10 and 0.50. A lower β_{DR} is used when all collapse mechanisms are considered and a higher β_{DR} when there is no special consideration for nonlinear mechanisms. A lower β_{TD} is used when there are tests supporting the design methods and a higher β_{TD} is selected when insufficient experimental data is available. A lower β_{MDL} is used when the model employed can capture component and system behavior that contributes to the collapse and a higher β_{MDL} is used if the model cannot predict cyclic strength degradation.

The following section begins the UCSD shake table specimen FEMA P695 seismic characterization with high fidelity nonlinear pushover analyses that are used to calculate system overstrength. The pushover curves are also valuable because they will support assumptions for a drift-based collapse limit used to calculate the *ACMR* since uncontrolled system collapse has not been observed in tests or simulation.

9.2. Nonlinear static pushover analysis to calculate UCSD shake table Specimen B1 and B2 system overstrength

Simulated pushover experiments are performed on UCSD shake table Specimens B1 and B2 with the high fidelity modeling protocol defined in Chapter 5. The pushover response in Figure 56, where drift is the lateral building displacement at the top of the panel zone, highlights the significant ductility and overstrength in a metal building, with drifts calculated out to more than 15 inches and peak base shear of 57 kips and 42 kips, compared to design base shears of 25.4 and 6.52 kips for Specimens B1 and B2. The first drop in load after peak is caused by lateral-torsional buckling in the primary frame span, with load redistribution and a second peak established when the lateral braces engaged against the lateral movements.

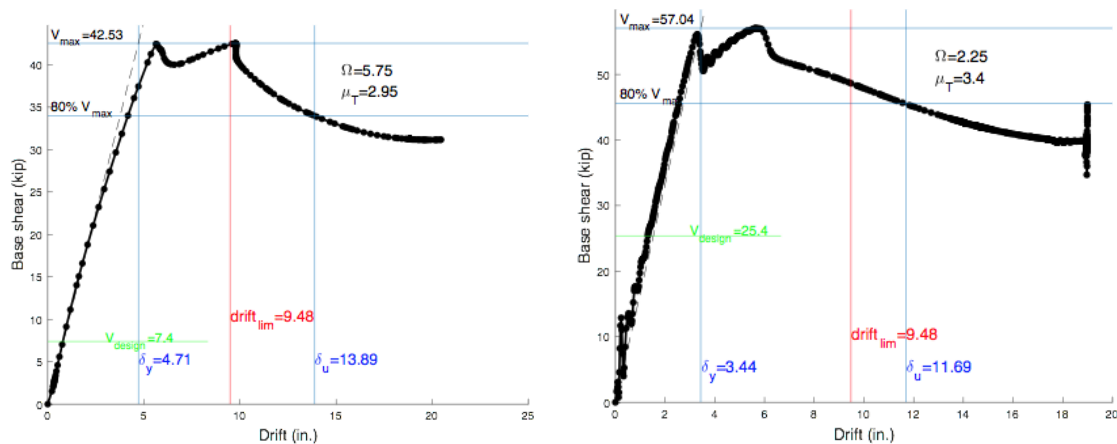


Figure 56. Nonlinear static pushover results for UCSD shake table Specimens B1 and B2

The maximum base shear capacity, V_{max} , the ultimate lateral displacement, δ_u , and the lateral displacement at $0.80V_{max}$ (20% degradation) are also labeled in Figure 56. These values are used to calculate the system overstrength and period-based ductility:

$$\Omega = V_{max}/V$$

$$\mu_T = \delta_u/\delta_{y,eff}$$

where V is the design base shear, and $\delta_{y,eff}$ is the effective yield roof drift displacement calculated as,

$$\delta_{y,eff} = C_o [V_{max}/W] [g/4\pi^2] (\max(T, T_1))^2$$

The system overstrength of Specimen B1 is higher than Specimen B2 because the seismic demand for Specimen B1 is very low and the frame has been mostly designed for gravity loads. The higher lateral demands for Specimen B2 from the heavy walls result in a design with a higher pushover capacity however the design base shear for Specimen B2 is also higher, resulting in a lower system overstrength.

9.3. Incremental dynamic analysis analysis and fragility curves for UCSD shake table Specimen B1 and B2

Incremental dynamic analyses are performed using the nonlinear SDOF modeling protocol introduced and verified in Chapter 8. The IDA effort considers the far-field record set of 44 ground motions in Appendix A of FEMA P695. The IDA procedure starts by defining the median spectral intensity of the far-field record set, S_T , measured at the fundamental period of the structure and then the far-field record set is scaled by $\alpha(S_{MT}/S_T)$, where α is the intensity factor and S_{MT} is the MCE intensity.

The trends in spectral acceleration, S_T , with maximum drift ratio are presented for UCSD shake table Specimens B1 and B2 in Figure 57 and Figure 58. Specimen B1 has low sensitivity to the different ground motions (closely spaced IDA curves in Figure 57) and resists collapse up until high spectral accelerations (minimal IDA curve flattening even at spectral accelerations exceeding 3g). The trends confirm the high system overstrength in Specimen B1. Specimen B2 IDA trends in Figure 58 highlight that it experiences buckling sooner because the IDA curves become nonlinear at lower drifts.

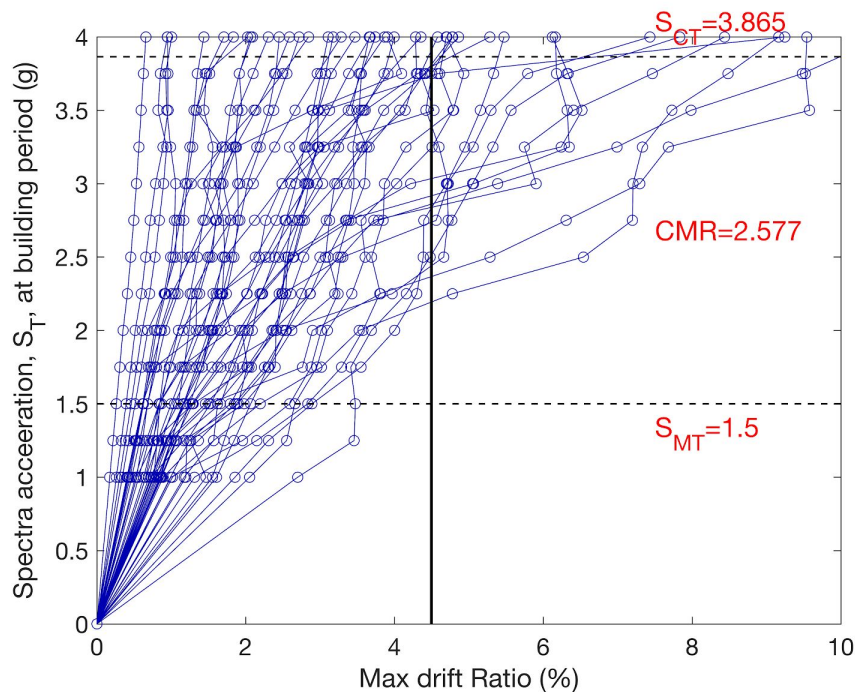


Figure 57. UCSD shake table Specimen B1 incremental dynamic analysis with the nonlinear SDOF modeling protocol (drift limit=4.5%)

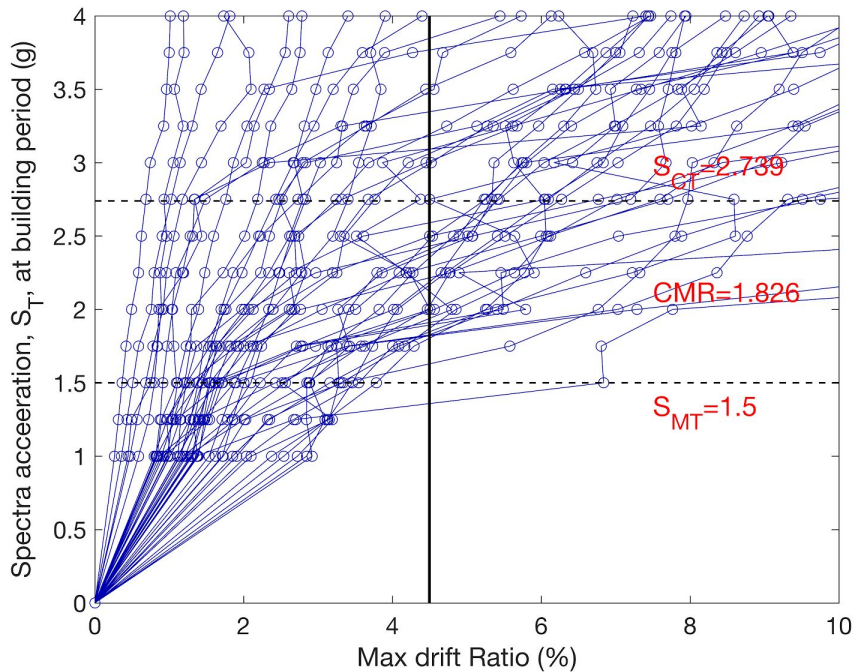


Figure 58. UCSD shake table Specimen B2 incremental dynamic analysis with the nonlinear SDOF modeling protocol (drift limit=4.5%)

9.4. Building system collapse definition and fragility curves for UCSD shake table Specimen B1 and B2

Uncontrolled collapse has not been observed for metal buildings in earthquakes. A collapse limit is still required however to calculate the probability of collapse and the ACMR. In Chapter 7, plastic strain analysis of the tested models showed that about 4.5% story drift could lead to initiation of rafter or panel zone fracture. This fracture limit state is not included in the high fidelity or SDOF simulation protocols. It is therefore prudent to select the lower range of this drift limit for a non-simulated collapse criterion of 4.5% drift which can be used to calculation of the ACMR. This collapse limit could also be interpreted as one that prevents significant structural damage to a metal building that would be difficult to repair after an earthquake.

The IDA curves in Figure 57 and Figure 58 and the selected collapse drift limit of 4.5% lead to the collapse fragility curves in Figure 59 and Figure 60 for Specimens B1 and B2. The fragility curves are cumulative collapse probability versus spectral intensity of the far-field record set, S_T . The median of the spectral intensity is the spectral intensity that corresponds to the 50% probability of collapse. A log-normal distribution is fit to the results to obtain this median, S_{CT} , as shown in Figures 59 and 60.

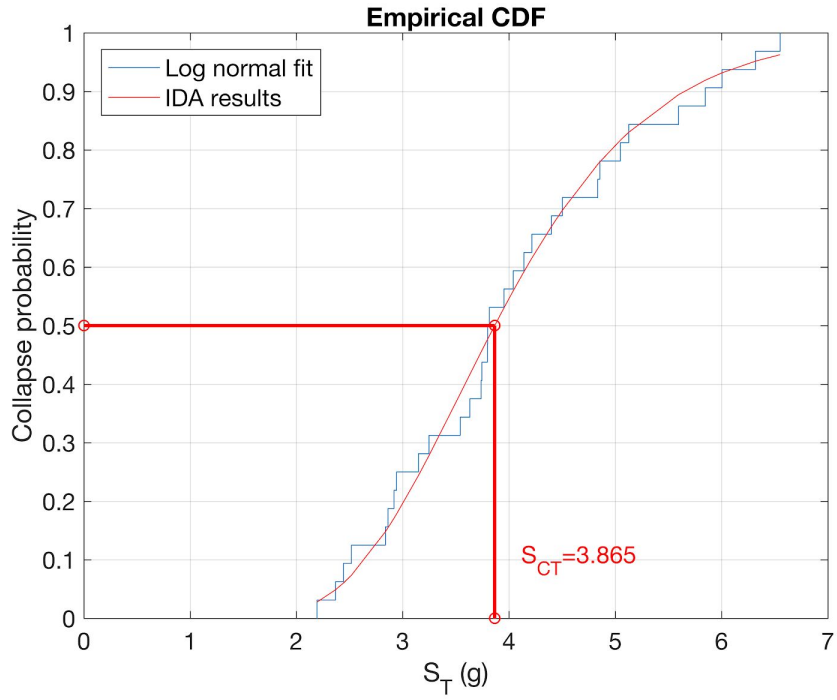


Figure 59. Collapse CDF (fragility curve) for UCSD shake table Specimen B1 (drift limit=4.5%)

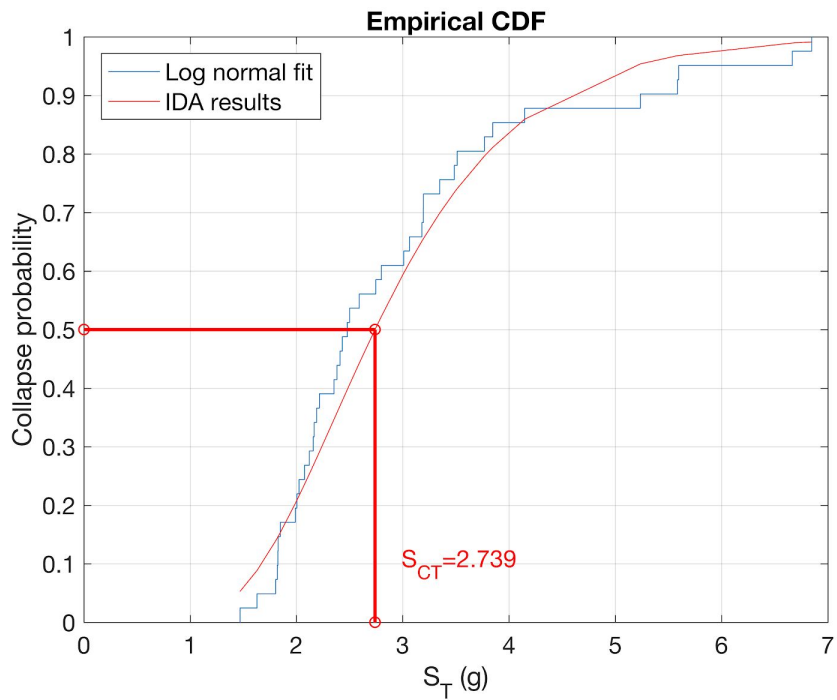


Figure 60. Collapse CDF (fragility curve) for UCSD shake table Specimen B2 (drift limit=4.5%)

9.5. Calculation of collapse margin ratio (ACMR) for UCSD shake table Specimens B1 and B2

The median of the spectral intensity of the far-field record set from the fragility curves in Figure 59 and Figure 60 lead to calculated S_{CT} =3.86 and 2.74 for Specimens B1 and B2. The CMR is then calculated as 2.58 and 1.83 for Specimens B1 and B2, respectively. The ACMR is 3.09 and 2.15 assuming SSF of 1.20 and 1.18 for Specimens B1 and B2.

The ACMR for Specimens B1 and B2 are then compared to the recommended acceptable collapse probability defined by FEMA P695, $ACMR_{20\%}$ =1.56 and $ACMR_{10\%}$ =1.96. The assumed uncertainty when calculating $ACMR_{10\%}$ and $ACMR_{20\%}$ is β_{TOT} =0.50, where β_{RTR} =0.40, β_{DR} =0.20, β_{TD} =0.20, and β_{MDL} =0.10. The record-to-record uncertainty β_{RTR} is high because μ_T is high. The test data-related uncertainty β_{DR} is low since shake table test data is available for the archetypes. The modeling-related uncertainty β_{MDL} is low because collapse characteristics including local and global buckling are represented well in both high fidelity and nonlinear SDOF models.

9.6. Seismic evaluation summary for UCSD metal building shake table Specimens B1 and B2

Seismic performance of the UCSD shake table specimens designed with common industry assumptions and details are summarized in Table 15. System overstrength is almost 2 times higher than designed for Specimen B1 because the building has low mass and the frame design demand envelope is minimally affected by seismic load combinations. Specimen B2, with its heavier walls, was governed by seismic demands and therefore its system overstrength is more consistent with design parameters.

Table 15. Adjusted Collapse Margin Ratio for Specimen B1 and B2

Specimen	Seismic Design Parameters R, Ω_o, C_d	Overstrength Ω	Period-Based Ductility μ_T	Collapse Margin Ratio CMR	Spectral Shape Factor SSF	Adjusted Collapse Margin Ratio $ACMR$
B1	3.5, 3, 3	5.75	2.95	2.58	1.20	3.09
B2	3.5, 3, 3	2.25	3.40	1.83	1.18	2.15

Specimens B1 and B2 can be assumed to be from the same performance group because their basic structural configurations including the lateral load resisting system, redundancy, type of the members, and connection configurations are similar. The buildings have the same gravity load and different seismic mass from the heavy walls in Specimen B2. Also, the same seismic

design category is assumed for both specimens. The measured natural periods are similar and the design natural periods were identical because the specimens are of the same height.

The average ACMR of this performance group is 2.62 in Table 16 which is about 30% higher than the acceptable adjusted collapse margin ratio $ACMR_{10\%}$ of 1.96. This means the performance group passes the evaluation procedure which is consistent with conclusions from the UCSD shake table tests, i.e., that the metal buildings performed without signs of uncontrolled collapse at the MCE level. The same ACMR calculations are performed in the next chapter with the larger performance group of metal building index archetypes defined in Chapter 4.

Table 16. Seismic Evaluation of UCSD Specimen B1 and B2 with FEMA P695

Specimen	Total system collapse uncertainty β_{TOT}	Adjusted Collapse Margin Ratio $ACMR_i$	Acceptable adjusted collapse margin ratio $ACMR_{20\%}$	Acceptable adjusted collapse margin ratio $ACMR_{10\%}$	Pass/Fail
B1	0.50*	3.09	1.56	1.96	Pass
B2	0.50	2.15	1.56	1.96	Pass
Average of the group		2.62	-	1.96	Pass

* The value is 0.495 but rounded to 0.50

10. Probabilistic Seismic Evaluation of Selected Metal Building Archetypes

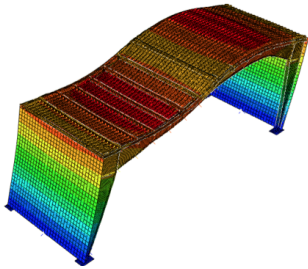
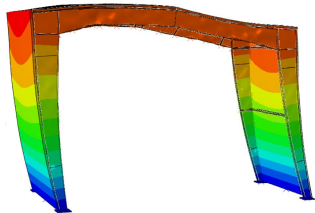

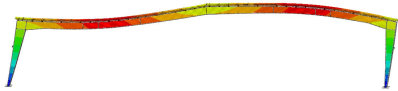
10.1. Defining the performance group of metal building index archetypes

A performance group of 4 index archetypes are evaluated in this chapter. The archetypes were selected based on the studies in Chapter 3 and designed with the details described in Chapter 4. The index archetypes are organized as A1 - a heavy, short metal building (70 ft span by 25 ft eave height); A2 - a heavy, tall metal building (70 ft span by 45 ft eave height); A3 - a light, short building (70 ft span by 45 ft eave height); and A4 - a light, long span building (200 ft span by 35 ft eave height).

10.2. Calculation of performance group natural periods with high fidelity modal analysis

High fidelity modal analysis provides the index archetype natural periods and first mode mass participation in Table 17. Archetypes A2 to A4 have similar natural periods ranging from 1.02 to 1.17 seconds with A1 - a heavy, short, tall building as the lowest at 0.79 seconds.

Table 17. Summary of the modal analysis results of the high fidelity models and period evaluation of the archetype buildings per FEMA P695 method ($C_u T_a$)

	First mode deformation	Period (modal) sec.	$T=C_u T_a$ (FEMA P695) sec.	Mass Participation ratio
Archetype A1 Heavy-Short		0.79	0.52	77%
Archetype A2 Heavy-Tall		1.16	0.82	82%
Archetype A3 Light-Short		1.02	0.52	83%
Archetype A4 Light- Long span		1.17	0.73	76%

10.3. Nonlinear static pushover analysis to calculate performance group system overstrength

Pushover response and system overstrength for the index archetypes A1 to A4, obtained with high fidelity simulation, are presented in Figure 61 to Figure 64. Index archetype A2 (heavy-tall building) has the highest system capacity $V_{max}=98.5$ kips with gradual post-peak strength degradation dominated by panel zone buckling and yielding, consistent with archetype A1 and UCSD shake table Specimen B2. Panel zone buckling and yielding concentrates shear in the frame knee in buildings with stiff, heavy walls. Archetypes A3 and A4 are more sensitive to rafter

span Lateral-Torsional Buckling (LTB) and post-peak system response holds constant until the flange braces fail. Post-peak drift capacity at 20% strength loss is less in archetypes A3 and A4 because of this LTB sensitivity, resulting in lower μ_T , compare 2.95 for A1 to 1.65 for A3.

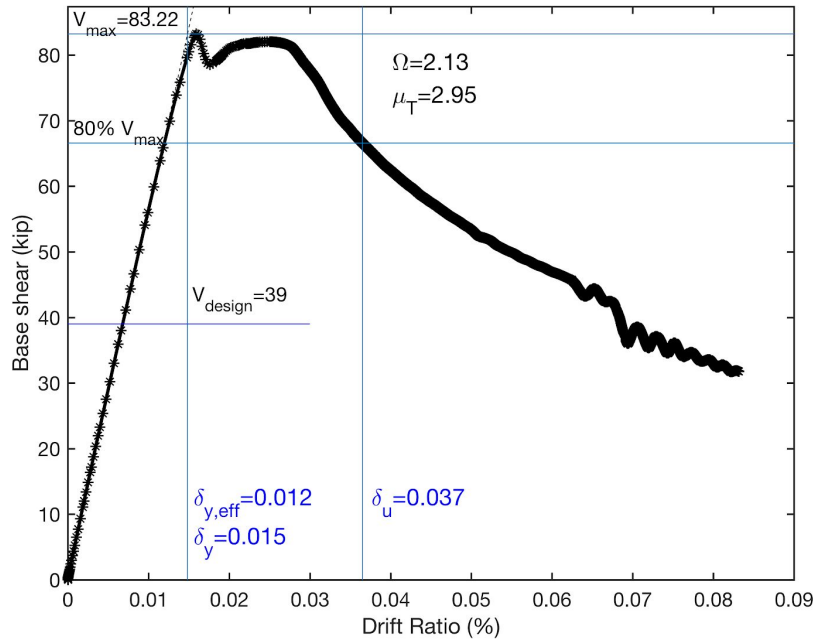


Figure 61. Nonlinear static pushover response for index archetype A1

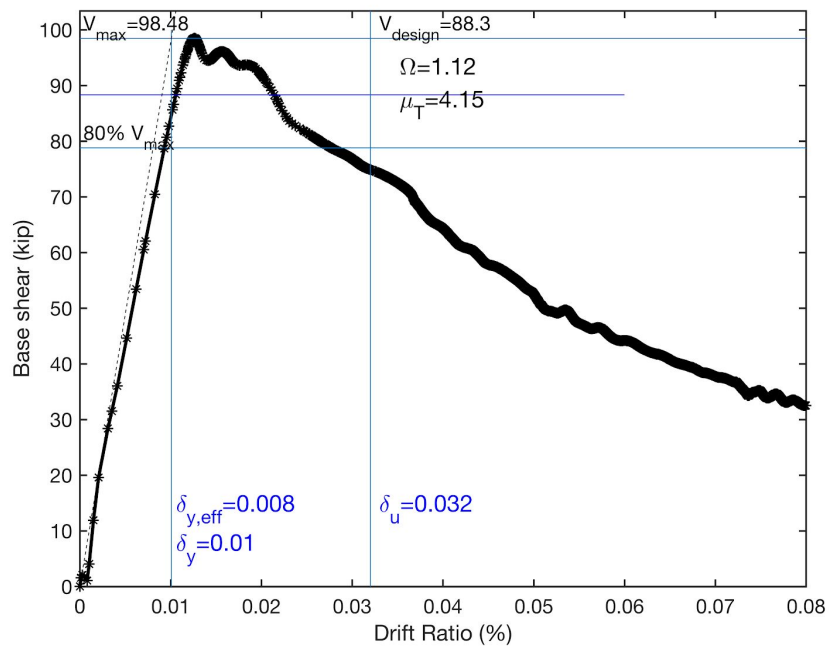


Figure 62. Nonlinear static pushover response for index archetype A2

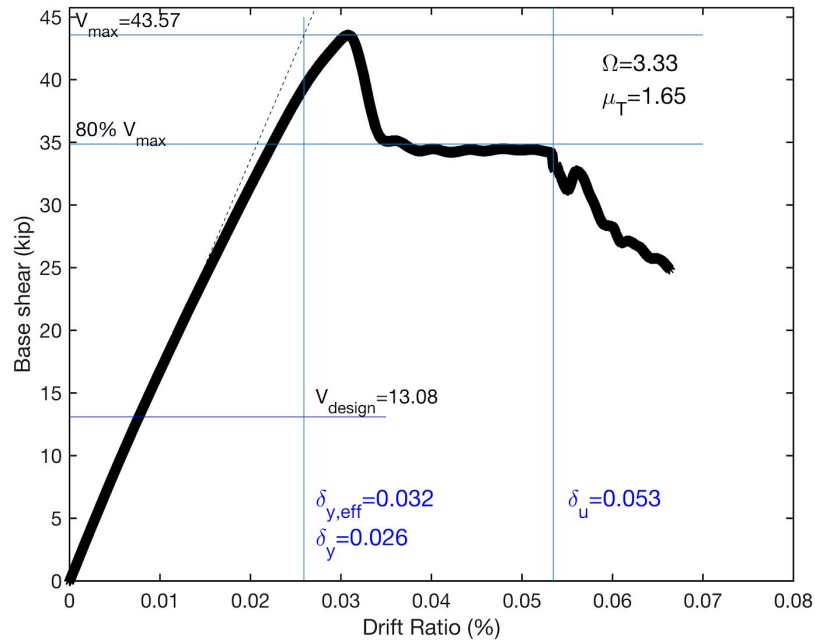


Figure 63. Nonlinear static pushover response for index archetype A3

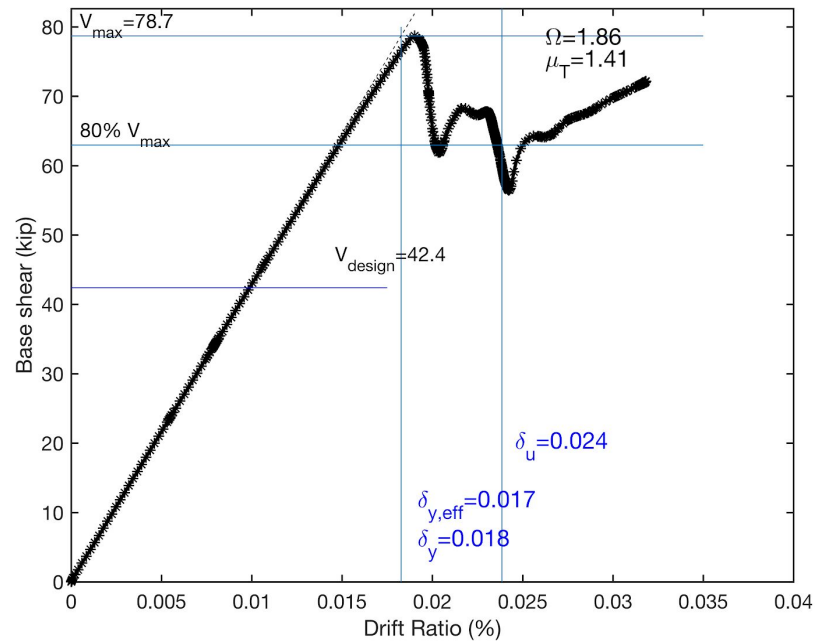


Figure 64. Nonlinear static pushover response for index archetype A4

Table 18. Metal building index archetype seismic design and performance parameters

Archetype	Design Base Shear V_b	Design Seismic Weight W_e	Seismic mass m	Equivalent initial stiffness k_{eq}
	kip	kip	kip.sec ² /in	kip/in
A1: Heavy - Short	39.0	137.6	0.354	22.37
A2: Heavy - Tall	88.3	311.0	0.805	23.6
A3: Light - Short	13.08	45.7	0.118	4.5
A4: Light - Long Span	42.4	148.4	0.384	11.3

10.4. Quasi-static high fidelity cyclic archetype simulation and SDOF spring model calibration

The high fidelity pushover models for archetypes A1 to A4 are used again, this time to characterize their quasi-static cyclic response including strength and stiffness degradation. Each archetype metal building is subjected to cyclic displacements at the knee level and the cyclic response is defined as base shear versus story drift (displacement or percentage), see Figure 65. Local and lateral-torsional buckling influences consistent with the UCSD shake table experiments are captured as shown in Figure 66 to Figure 68.

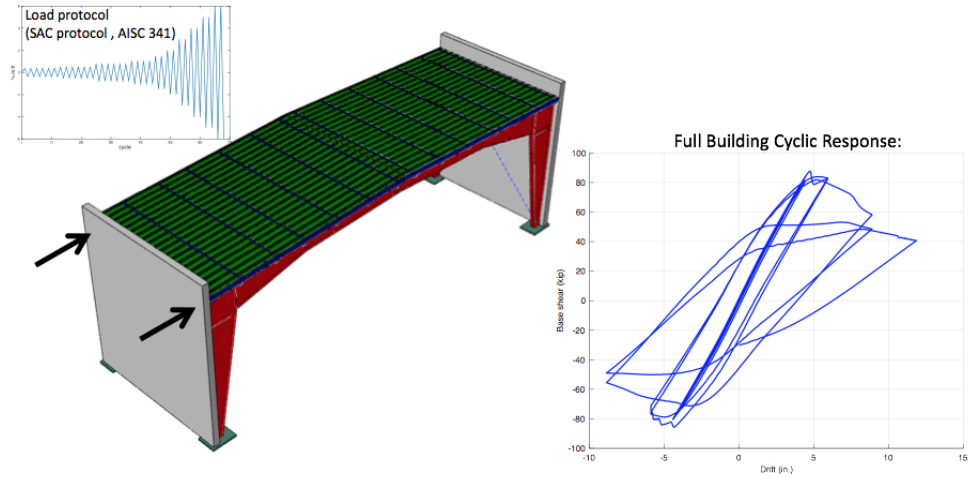


Figure 65. High fidelity quasi-static cyclic response of archetype A1 using the AISC 341 cyclic loading protocol

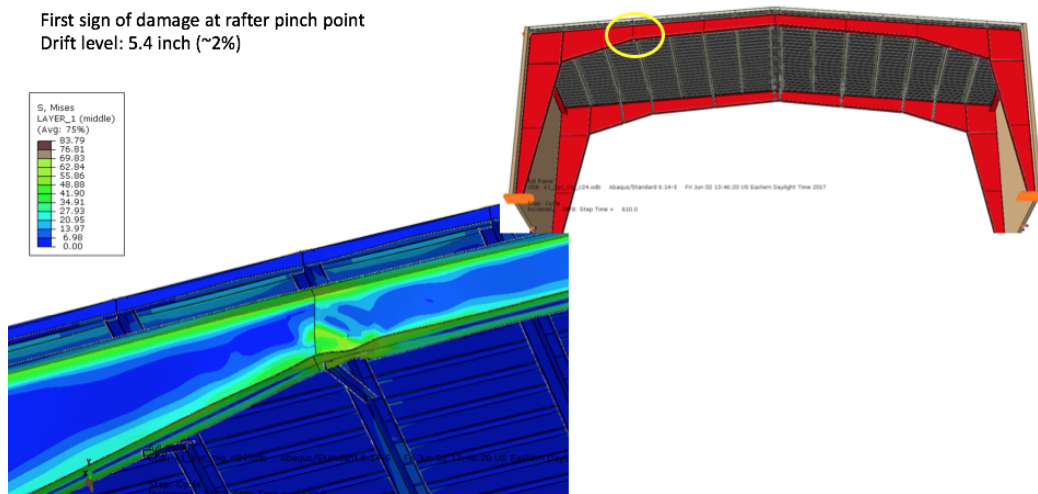


Figure 66. Archetype A1 frame buckling at 2.0% story drift

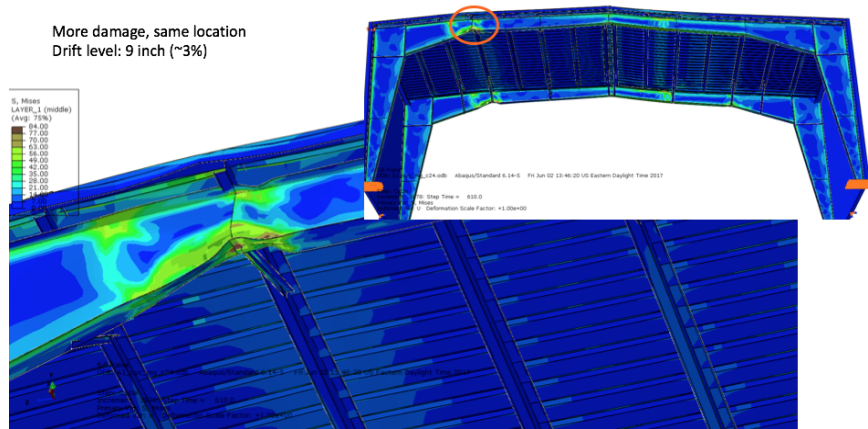


Figure 67. Archetype A1 buckling deformation at 3.0% story drift

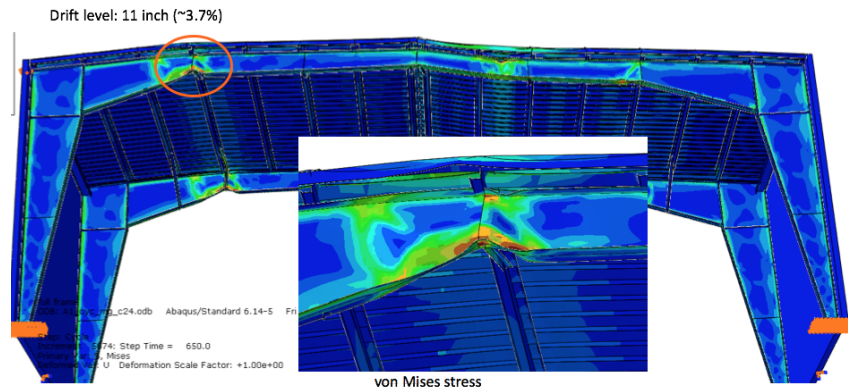


Figure 68. Archetype A1 buckling deformation at 3.7% story drift

This quasi-static cyclic behavior is used to calibrate the nonlinear SDOF model spring required for incremental dynamic analysis. The cyclic response in Figure 69 to Figure 71 is defined with the AISC 341 cyclic loading protocol. The cyclic response is matched to the Pinching 04 material model in OpenSees, which are the red color lines in Figure 69 to Figure 71. The Pinching 04 model are anchored to the building response primarily in the first and third quadrants. The cyclic energy curves and cumulative cyclic energy curves for each archetype, generated with high fidelity simulation and the Pinching-04 models, are consistent.

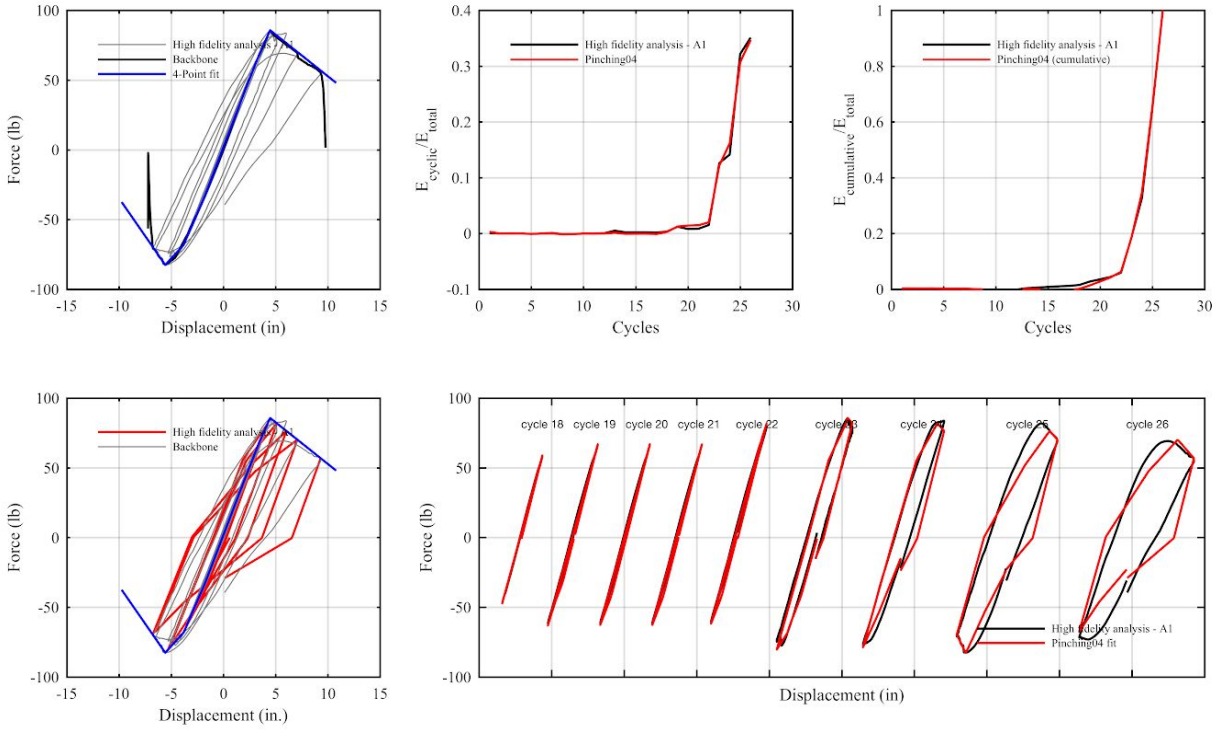


Figure 69. High fidelity quasi-static and Pinching 04 cyclic response: Archetype A1

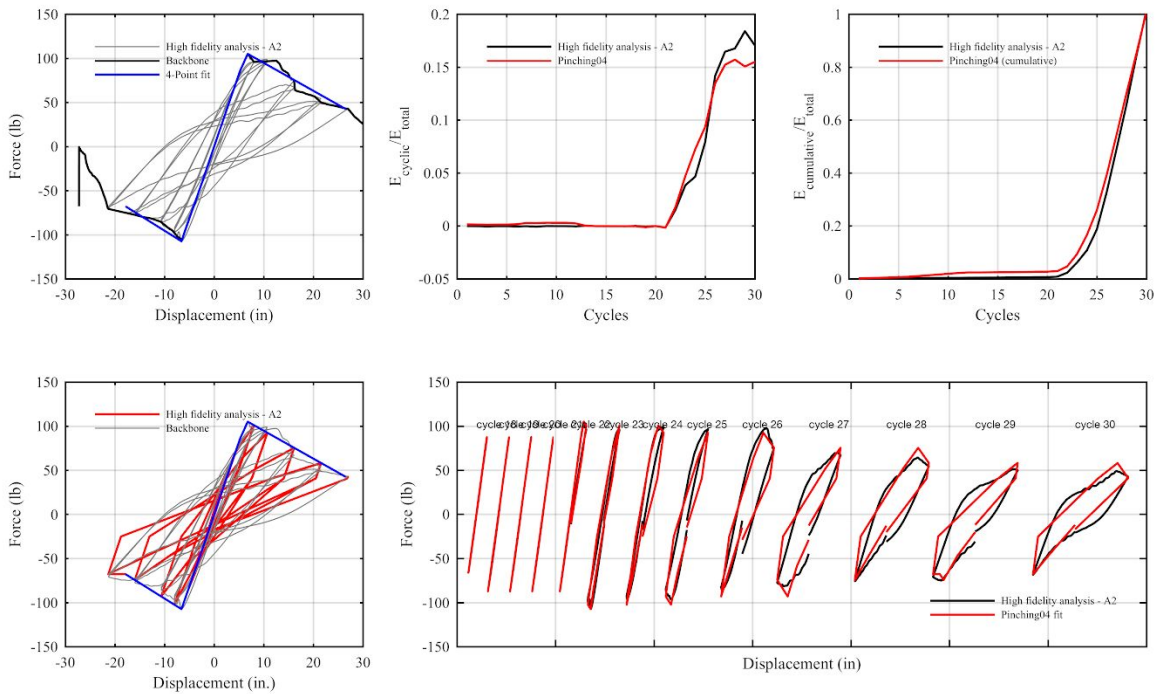


Figure 70. High fidelity quasi-static and Pinching 04 cyclic response: Archetype A2

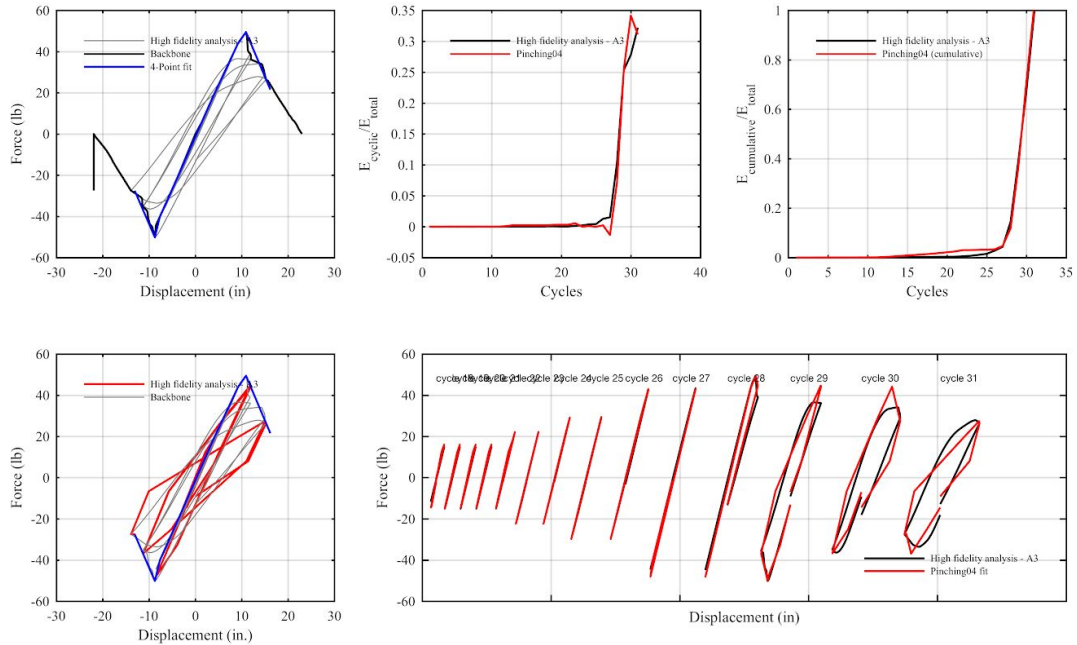


Figure 71. High fidelity quasi-static and Pinching 04 cyclic response: Archetype A3

10.5. Incremental dynamic analysis analysis and fragility curves for metal building index archetypes

Incremental dynamic analyses (IDAs) are performed using the same nonlinear SDOF modeling protocol employed in Chapter 9. Each IDA curve includes 572 SDOF nonlinear response analysis results. The trends in spectral acceleration, S_T , with maximum drift ratio are presented in Figure 72 to Figure 75 for index archetypes A1 to A4. The trends in spectral acceleration show that archetypes A1 to A4 begin to exhibit nonlinear behavior (buckling and yielding) earlier than UCSD shake table Specimens B1 and B2.

The IDA curves in Figure 72 to Figure 75 and the selected collapse drift limit of 4.5% lead to the collapse fragility curves in Figure 76 and Figure 79 for index archetypes A1 to A4.

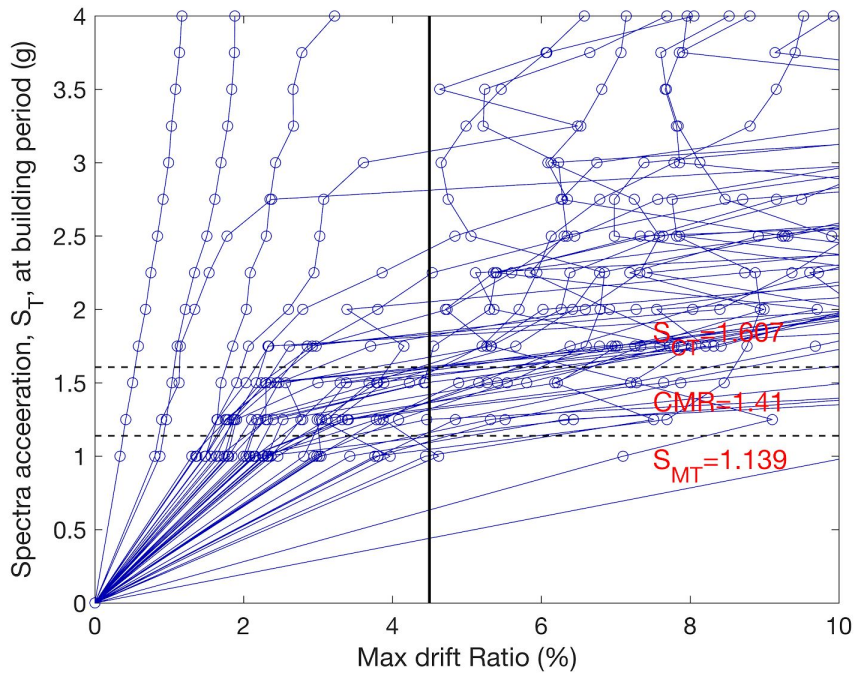


Figure 72. Index archetype A1 incremental dynamic analysis with the nonlinear SDOF modeling protocol (drift limit=4.5%)

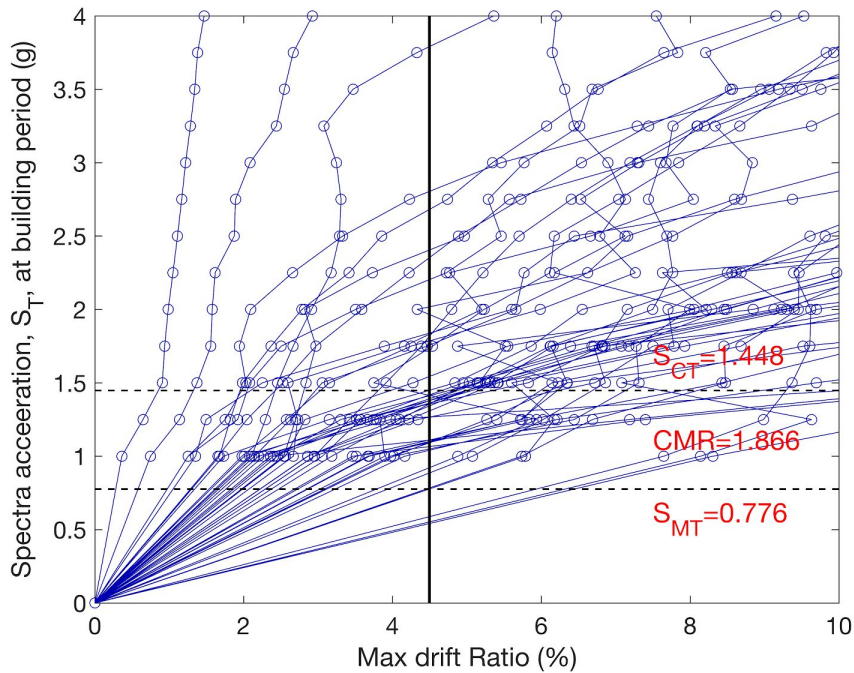


Figure 73. Index archetype A2 incremental dynamic analysis with the nonlinear SDOF modeling protocol (drift limit=4.5%)

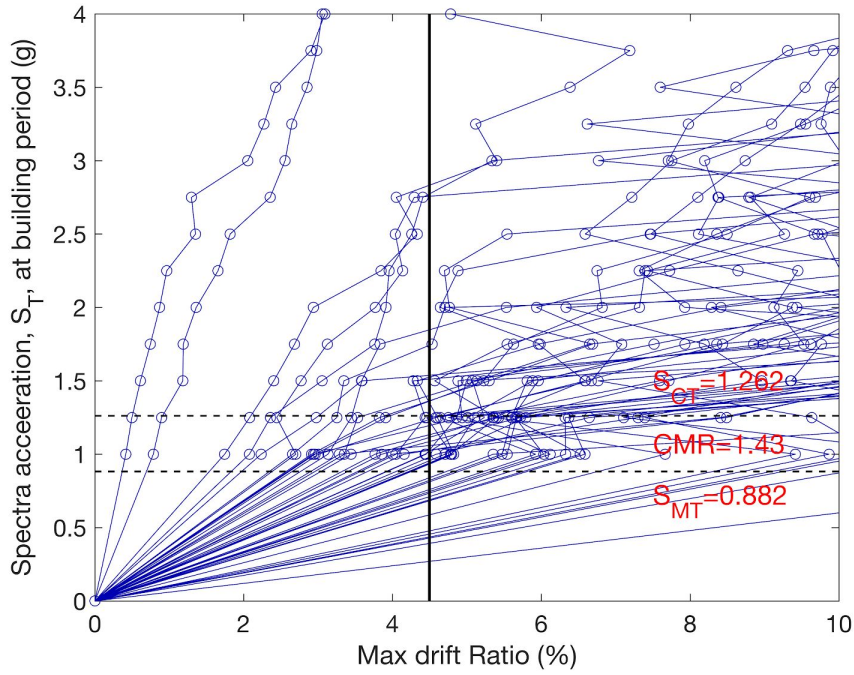


Figure 74. Index archetype A3 incremental dynamic analysis with the nonlinear SDOF modeling protocol (drift limit=4.5%)

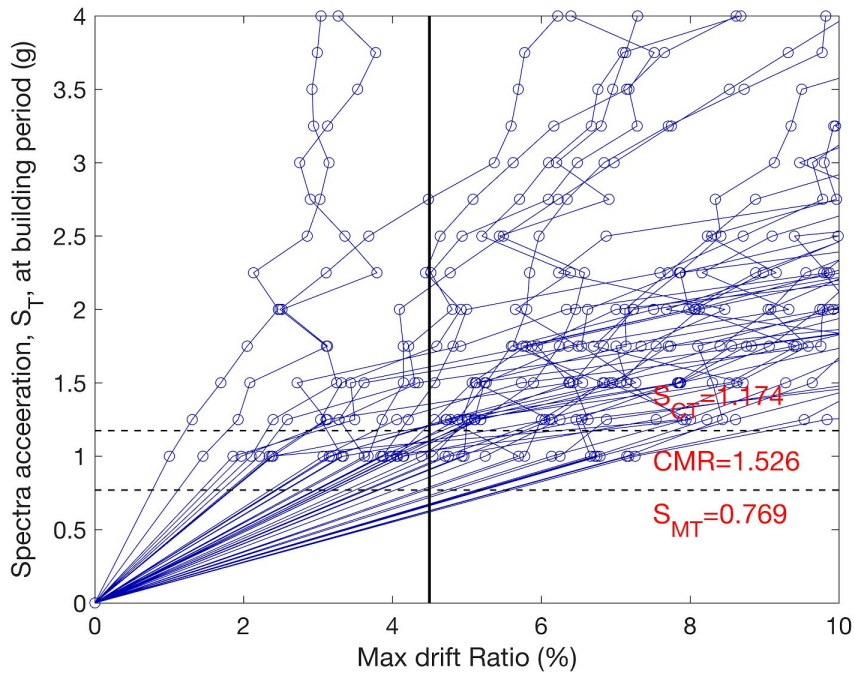


Figure 75. Index archetype A4 incremental dynamic analysis with the nonlinear SDOF modeling protocol (drift limit=4.5%)

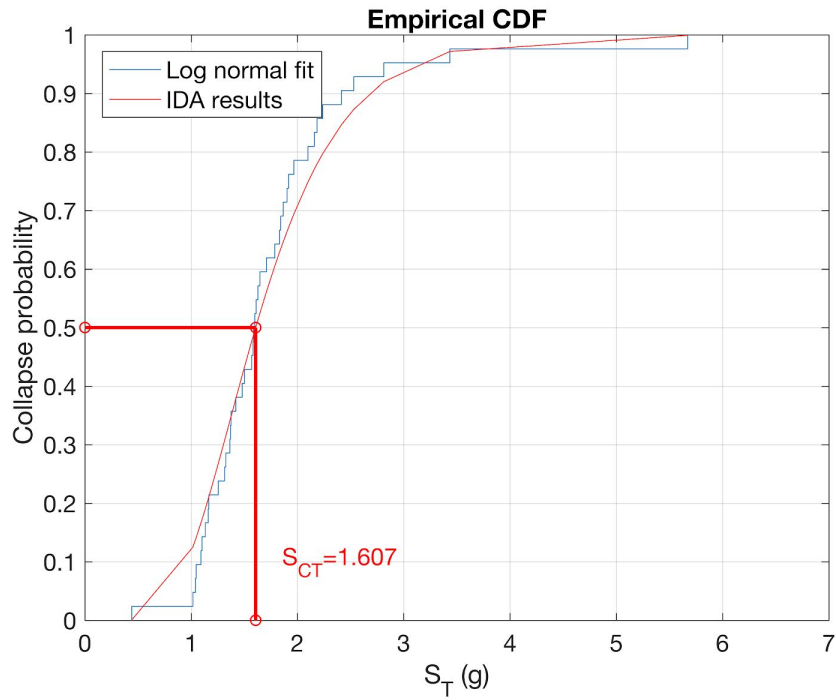


Figure 76. Collapse CDF (fragility curve) for index archetype A1 (drift limit=4.5%)

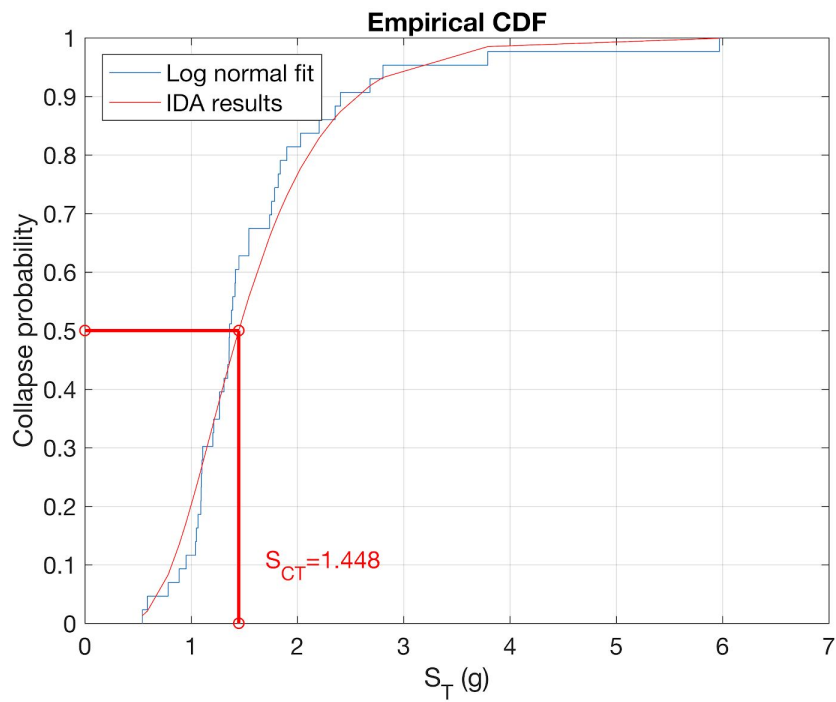


Figure 77. Collapse CDF (fragility curve) for index archetype A2 (drift limit=4.5%)

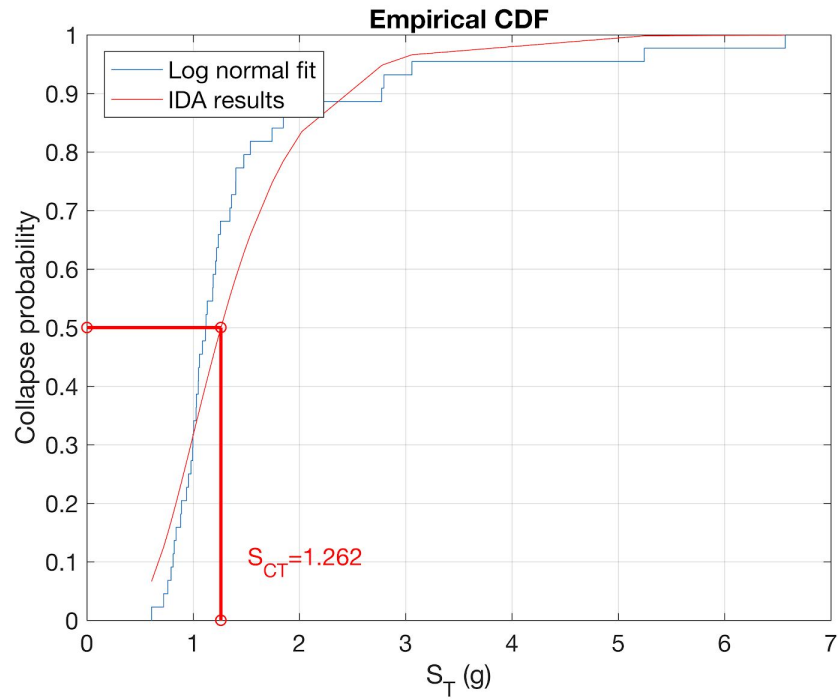


Figure 78. Collapse CDF (fragility curve) for index archetype A3 (drift limit=4.5%)

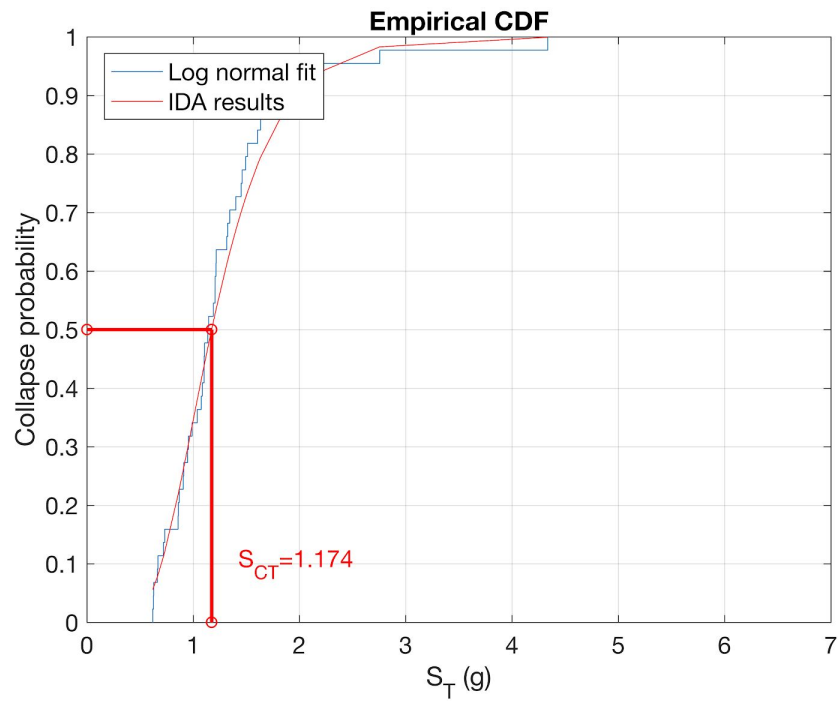


Figure 79. Collapse CDF (fragility curve) for index archetype A4 (drift limit=4.5%)

10.6. Seismic evaluation summary for archetype performance groups

The median of the spectral intensity of the far-field record set from the fragility curves in Figure 76 to Figure 79 leads to S_{CT} and the adjusted collapse margin ratios for the performance group summarized in Table 19. The acceptable collapse margin ratios $ACMR_{20\%}$ and $ACMR_{10\%}$ are calculated with assumed uncertainty of β_{TOT} where β_{RTR} is calculated in Table 19, $\beta_{DR}=0.20$, $\beta_{TD}=0.20$, and $\beta_{MDL}=0.10$ consistent with the same calculations for the UCSD shake table specimens in Chapter 9.

Table 19. Adjusted Collapse Margin Ratio for Archetype A1 to A4

Specimen	Seismic Design Parameters R, Ω, C_d	Overstrength Ω	Period-Based Ductility μ_T	Collapse Margin Ratio CMR	Spectral Shape Factor SSF	Adjusted Collapse Margin Ratio $ACMR$
A1: Heavy - Short	3.5, 3, 3	2.13	2.95	1.22	1.22	1.58
A2: Heavy - Tall	3.5, 3, 3	1.12	4.15	1.22	1.22	1.72
A3: Light - Short	3.5, 3, 3	3.33	1.65	1.34	1.34	2.30
A4: Light - Long Span	3.5, 3, 3	1.86	1.41	1.34	1.34	2.50

As shown in Table 20, the average of the ACMRs in the performance group is 1.895 for a collapse drift limit of 4.5%, which is higher than $ACMR_{10\%}$ again confirming the satisfactory collapse-level seismic performance of typical metal buildings within the considered performance group. The ACMR for each index archetype is higher than $ACMR_{20\%}$ and so even the lowest performing metal building archetype selected (A1) still has a sufficient margin against collapse.

Table 20. Adjusted Collapse Margin Ratio for index archetypes A1 to A4

Archetype	Total system collapse uncertainty β_{TOT}	Adjusted Collapse Margin Ratio $ACMR_i$	Acceptable adjusted collapse margin ratio $ACMR_{20\%}$	Acceptable adjusted collapse margin ratio $ACMR_{10\%}$	Pass/Fail
A1	0.50	1.72	1.52	1.89	Pass
A2	0.50	2.50	1.52	2.15	Pass
A3	0.40	1.64	1.40	1.67	Pass
A4	0.38	1.72	1.38	1.64	Pass
Average of the group		1.895	-	1.837	Pass

11. Conclusions and Possible Next Steps

The applicability of ASCE 7 seismic design procedures is confirmed in this study for industry typical light wall and heavy wall metal buildings, including the use of $R=3.5$. The confirmation stands on a rigorous seismic evaluation following a step-by-step approach outlined in FEMA P695. The confirmation process began more than 10 years ago with subassembly and shake table experiments at UCSD that highlighted primary frame local and lateral-torsional buckling and rafter-column knee panel zone tension field action, buckling, and tearing as important seismic limit states. The extensive experimental program served as a valuable verification of an ambitious high fidelity modeling protocol, made relevant with high performance computing, to conduct pushover analyses, quantify system overstrength and ductility, and directly model cyclic strength and stiffness degradation for a series of index archetypes.

The high fidelity models discretized the primary and secondary systems with shell elements to directly capture frame buckling limit states observed in the UCSD tests, and included almost every part and piece in a typical metal building, from flange braces to metal roof panels to rod bracing. The culminating nonlinear incremental dynamic analyses confirmed what had already been observed in the UCSD shake table tests, that uncontrollable system collapse of these gravity-light buildings is difficult, and that the average collapse probability in the performance group is less than 10% for a Maximum Considered Earthquake (MCE). The sensitivity of primary frame design to height-to-span ratio showed that shorter span, taller buildings will be defined more by seismic demands, where shorter, longer span buildings are governed by their geographical location (snow in the northwest U.S., wind in the southeast U.S.). The key to a high performing metal building is a well-designed primary frame bracing system that holds the brace points after global buckling deformation initiates.

With a seismic evaluation process now established and validated, the metal building industry can set their sights on other performance groups with potentially large commercial impact - for example, heavier roof buildings with a dead load higher than 20 psf and buildings that are taller than 65 ft, both of which are currently excluded from ASCE 7. These studies could be organized in a very similar way to the tall-short, heavy-light A1 to A4 archetype study in Chapter 10 and completed quickly thanks to the investment MBMA has made in exploring high performance computing. A modular metal building seismic performance group also becomes available for study with the high fidelity modeling protocol that could be used to perform simulated pushover experiments and to quantify cyclic performance.

And the impact of this MBMA analysis investment extends beyond earthquake engineering. The high fidelity 'experiment by simulation' capability can be used to gain market advantages where codes and standards currently penalize the industry, namely wind design and thermal performance.

Acknowledgments

Both the MBMA Seismic Research Steering Group and the peer review panel provided consistently thoughtful advice, input, effort, and feedback throughout this multi-year project. The peer review panel was made up of Greg Deierlein, Michael Engelhardt, and Tom Sabol. Lee Shoemaker and Vince Sagan of MBMA were instrumental in shepherding this project to a meaningful end. The project was sponsored by the American Iron and Steel Institute (AISI) and MBMA.

References

AISC (2010). ANSI/AISC 341-10, Seismic Provisions for Structural Steel Buildings, American Institute of Steel Construction, Chicago, IL.

ATC (2009). "Quantification of building seismic performance factors," Report No. FEMA-P695, Applied Technology Council, Redwood City, CA.

ASCE (2010). Minimum Design Loads for Buildings and Other Structures, ASCE/SEI 7-10, American Society of Civil Engineers, Reston, VA.

Hong, J.K. and Uang, C.M. (2006). Cyclic Performance Evaluation of a Metal Building System with Web-Tapered Members, Report No. SSRP-06/23, Department of Structural Engineering, University of California, San Diego, La Jolla, CA.

Hong, J.K. and Uang, C.M. (2007). Development of A Seismic Design Procedure for Metal Building Systems, Report No. SSRP-07/17, Department of Structural Engineering, University of California, San Diego, La Jolla, CA.

Kaehler, R.C., White., D.W., and Kim, Y.D. (2011). "Frame Design Using Web- Tapered Members," Steel Design Guide 25, AISC/MBMA, Chicago, IL.

Kim, Y.D. (2010). "Behavior and Design of Metal Building Frames with General Prismatic and Web-Tapered Steel I-Section Members," Doctoral Dissertation, School of Civil and Environmental Engineering, Georgia Institute of Technology, Atlanta, GA.

Mathworks (2016). Matlab Version 2016(b). Available at <https://www.mathworks.com/products/matlab.html>.

McKenna, F., Fenves, G.L., and Scott, M.H., (2004). "Open System for Earthquake Engineering Simulation." Pacific Earthquake Engineering Research Center, University of California, Berkeley.

Prawel, S.P., Morrell, M.L., and Lee, G.C. (1974). "Bending and Buckling Strength of Tapered Structural Members," Welding Research Supplement, Vol. 53, pp. 75- 84.

Schafer, B.W., Li, Z., Moen, C.D. (2010). "Computational modeling of cold-formed steel." Thin-Walled Structures, 48, pp. 752-762.

Simulia (2014). ABAQUS Version 6.14. Available at <https://www.3ds.com/products-services/simulia/products/abaqus/>.

Smith, M.S., Turner, K.T., and Uang, C.M. (2013). "Experimental Investigation of Cyclic Lateral Buckling of Web-Tapered I-Beams," Report No. SSRP-12/06, Department of Structural Engineering, University of California, San Diego, La Jolla, CA

Smith, M.S. (2013). Seismic Testing and Analytical Studies for the Development of New Seismic Force Resisting Systems for Metal Buildings. Ph.D Dissertation, University of California, San Diego.